General Introduction

Background of the work

Transition metal oxides, especially 3*d* transition metal oxides have a rich variety of electrical, optical, and magnetic properties. Examples include copper oxide high-temperature superconductors [1−6], titanium oxide photocatalysts [7] or ferroelectrics [8−10], manganese oxide colossal magnetoresistant materials [11−13], and ferrite magnets [14], to name only a few. Such functional properties in the 3*d* transition metal oxides have attracted considerable attention, and materials with various kinds of chemical compositions have been studied.

Traditionally, the most common synthetic route to oxides is the so-called high temperature solid state (HTSS) reaction method, where raw materials such as metal

oxides and carbonates are mixed and heated at high temperatures (> 1000 ºC) [15]. The HTSS method has enabled the synthesis of numerous structure types such as perovskites, spinels, and pyrochlores (Figures 1−3) with various chemical compositions. However, the HTSS method encounters a difficulty in obtaining new coordination geometries other than those of well-known crystal structures: because of relatively small ionic radii of transition metal ions, they generally have a preference for tetrahedral and octahedral coordination, as found in perovskite, spinel, and pyrochlore oxides. Additionally, the HTSS reactions usually result in products with crystal structures quite different from those of the raw materials. Thus, it can be difficult to predict or control the crystal structures of the products using the HTSS method, although the chemical and physical properties of materials are closely related to their crystal structures. To overcome these problems, researchers have developed several methods, where structurally related precursors are utilized to synthesize new compounds with unprecedented crystal structure (i.e. topochemical reactions [16, 17])

There has been considerable investigation on materials with functional morphologies such as thin films and porous materials. There are several preparation methods desirable for these materials: to name only a few, methods include pulsed laser deposition (PLD) methods for thin films [18], sol-gel with phase separation methods for porous monoliths [19]. However, there still remain limitations in controlling the chemical compositions of the as-prepared oxide materials, such as oxygen non-stoichiometry. Thus, reactions using these as-prepared materials as precursors could offer an opportunity to obtain novel materials where the morphologies of the precursors are retained through the reactions.

Topochemical reactions

The synthesis of inorganic compounds at relatively low temperatures (< 500 ºC) has been utilized to synthesize compounds with specific crystal structures and chemical compositions, which can never be obtained at high temperatures. In particular, topochemical reactions, where the crystal structure of a precursor is partially modified by insertion and/or elimination of atoms while leaving the remaining lattice intact, allow the prediction of crystal structure of the products in principle. For example, a layered manganate $LiMnO_2$, which is isostructural with the famous positive electrode material $LiCoO_2$ for lithium ion batteries and has recently been expected to serve as a cheap alternative of the Co analog, cannot be directly prepared via high temperature due to formation of $LiMn_2O_4$ spinel; instead, at room temperature, layered $LiMnO_2$ is prepared via ion-exchange reaction of layered $NaMnO_2$ as a precursor (synthesized via conventional HTSS route) with excess LiBr in *n*-hexanol solution (Figure 4): [20]

$$NaMnO_2 + LiBr \rightarrow LiMnO_2 + NaBr \quad (1)$$

Such ion-exchange reactions are also applicable to layered perovskites such as Dion-Jacobson (DJ) type (with the general formula $A'A_{n-1}B_nO_{3n+1}$ [21, 22]) and the Ruddlesden-Popper (RP) type (with the general formula $A'_2A_{n-1}B_nO_{3n+1}$ [23, 24]) (Figures 5, 6). In these series of compounds, *A'* cations can be replaced with different monovalent cations (e.g. H^+, Li^+, NH_4^+) or divalent cations (e.g. Ca^{2+} and transition metals, with 50% amount), by reactions with their nitrates or halides in air or aqueous solution [16]. Moreover, different from these cation exchange reactions, Wiley and

coworkers succeeded the co-exchange of *A*' cations with both cations and anions (i.e. Rb^+ with Cu^{2+} and X^- (X^- = Cl, Br)) in a DJ type layered perovskites $RbLaNb_2O_7$:

$$RbLaNb_2O_7 + CuCl_2 \rightarrow (CuCl)LaNb_2O_7 + RbCl \quad (2)$$

,which resulted in the synthesis of (Cu*X*)$LaNb_2O_7$ (X^- = Cl, Br), an intergrowth structure of CuX_4 square planes with apical oxygen (see Figure 7) [25]. This co-exchange reaction have readily been extended to the related DJ layered perovskites, giving other (Cu*X*)$A_{n-1}B_nO_{3n+1}$ including (CuCl)$LaTa_2O_7$ and (CuCl)$Ca_2Ta_3O_{10}$ [26, 27].

Another topochemical reaction is the intercalation/deintercalation reaction. These processes require redox ability of the precursor compounds. This reaction has been intensively studied due to its relevance in lithium ion batteries. For example, $LiCoO_2$ and $LiFePO_4$ are famous positive electrode materials, where intercalation or deintercalation of Li ions occurs during the charge/discharge process [28, 29]. Oxygen intercalation/deintercalation from oxides is one of the most important aspects of solid state chemistry, because of the widespread application arising from their different electronic, magnetic and catalytic properties. To date, for oxygen removal, hydrogen gas or finely divided electropositive getter metals, such as zirconium or aluminum have been used [30, 31]. Other methods for oxygen insertion include reactions with high oxygen pressure [32, 33] and electrochemical reactions [34]. Notably, most of these reactions occur at temperatures well above 300 ºC: thus it would be very interesting to study novel ways to reduce these materials at mild temperatures, which may then give access to reduced oxides inaccessible at high temperatures.

The use of metal hydrides e.g. NaH and CaH_2 as powerful reducing reagents has

been used to synthesize several 3*d* metal oxides with greater oxygen vacancies (or lower oxidation states) at lower temperatures than could be achieved by standard methods. For instance, Rosseinsky and coworkers reported that using NaH a square-planar nickel oxide $LaNiO_2$ was successfully synthesized from $LaNiO_3$ (Figure 8) at 200 ºC, a much lower reaction temperature than with a previous method (400 ºC) [35]. Other examples include $LaSrCoO_{3.38}$ from $LaSrCoO_4$ [36], and $YSr_2Mn_2O_{5.5}$ from $YSr_2Mn_2O_7$ using NaH [37], while the use of CaH_2 yields $Y_2Ti_2O_{5.99}$ from $Y_2Ti_2O_7$ [38], $La_3Ni_2O_6$ from $La_3Ni_2O_7$ [39], and square planar iron oxides $SrFeO_2$/$CaFeO_2$ from $SrFeO_{3-\delta}$/$CaFeO_{2.5}$ and $Sr_3Fe_2O_5$ from $Sr_3Fe_2O_{7-\delta}$ [40−42]. These metal hydrides enable the reduction of oxides at very low temperatures compared to conventional reducing methods. Therefore, the low temperature reduction methods would allow topochemical reactions with partial retention of the precursor crystal structures.

This low-temperature reduction technique was also applied to prepare oxide thin films using precursor film materials, as in the preparation of $SrFeO_2$/$CaFeO_2$ films from $SrFeO_{3-\delta}$/$CaFeO_{2.5}$ films [43, 44] and $LaNiO_2$ films from $LaNiO_3$ films [45]: notably, the epitaxial nature in the precursor films were retained through the low-temperature reduction process. Therefore, the hydride reduction methods are attractive which could provide oxide materials without significantly destroying the specific morphologies of precursors.

Layered perovskite copper oxyhalides (Cu*X*)$A_{n-1}B_nO_{3n+1}$

As the author mentioned above, Wiley and coworkers have developed a series of copper oxyhalide layered perovskites (Cu*X*)$A_{n-1}B_nO_{3n+1}$ (X^- = Cl, Br) [25−27]. In all of

these materials, the inserted $[CuX]^+$ layer has magnetic Cu^{2+} ions with the spin quantum number $S = 1/2$, arranged at the vertices of square lattice. Additionally, each magnetic $[CuX]^+$ layer is separated by nonmagnetic $A_{n-1}B_nO_{3n+1}$ perovskite blocks (see Figure 7). Therefore, in these compounds quantum magnetic properties based on a square lattice with good two-dimensionality are expected. Square-lattice-based two-dimensional (2D) quantum magnets have been considered as key materials for understanding the high temperature superconductivity in copper oxides [46]. Thus it is of great interest to investigate the magnetic properties of $(CuX)A_{n-1}B_nO_{3n+1}$.

Kageyama and coworkers have studied the magnetic properties of the ion-exchanged layered cupric perovskites. As a result, it was revealed that unlike conventional magnets which undergo a phase transition from a magnetically disordered (i.e. paramagnetic) to ordered state at low temperature, $(CuCl)LaNb_2O_7$ does not show magnetic order (i.e. spin-disordered state) even at 2 K [47, 48]. By contrast, $(CuBr)LaNb_2O_7$, the isomorph of $(CuCl)LaNb_2O_7$, exhibits collinear (or stripe) magnetic order at 32 K [49]. Additionally, in these compounds, strong geometrical frustration and the coexistence of ferromagnetic and antiferromagnetic interactions were also indicated. However, not only the detailed magnetic properties of $(CuCl)LaNb_2O_7$ (such as its behavior at high magnetic field) but also the magnetic behaviors of the related compounds (e.g. another isomorph $(CuCl)LaTa_2O_7$) are still unclear, thus further study is required for deep and systematical understanding.

Titanium oxides with specific morphologies

Together with efforts to search for new compounds, materials with specific

morphologies e.g. thin films and porous materials have also been intensively investigated. Titanium oxides are one of the most studied materials, because of a low environmental burden, biocompatibility, low cost, and chemical stability. Titanium dioxide ($Ti^{4+}O_2$, d^0) are a famous wide gap semiconductor utilized as photocatalyst [7] and/or photovoltaics [50], and to make use of such functional properties there have been intensive research on their morphologies such as thin films and porous monoliths.

TiO_2 thin films are considerably studied due to the interest for various kinds of optical, magnetic, and electrical devices. In particular, anatase TiO_2 thin films have been of interest due to their use as transparent magnets or conductors. For precise control of the electrical properties or carrier concentrations it is important to control the chemical compositions widely and systematically. Carrier injection into anatase TiO_2 has been performed mainly by metal substitution [51, 52] and/or oxygen defects [53−55]. In the latter case, the oxygen content was controlled by varying the partial oxygen pressure during growth [53, 54] and/or by annealing with flowing gases such as H_2 [55]. However, because of the instability of anatase structure at high temperature, the reaction temperature has been limited to about 500 °C: thus it has been difficult to obtain highly reduced anatase using the conventional reduction methods. Therefore, the low-temperature reduction methods using metal hydrides are attractive, since they could offer oxygen-deficient anatase $TiO_{2-\delta}$ thin films with unprecedentedly large amount of oxygen vacancies.

Porous materials are of great interest because of low density, good mass transport, and high surface area. In particular, porous monolithic materials possess various applications. Examples of porous titania monoliths include electrodes [56, 57], separation media [58], biomedical materials [59], and so on. Such porous oxide

monoliths have usually been prepared via the sol-gel process, using a polymer or silica template method [60−62], or using the phase separation method [58, 63−65]. The phase separation method is based on a spinodal decomposition, where the solution separated into a TiO_2 sol phase and a solvent phase, forming the basis of a macroporous structure; the following gelation process and calcinations fixes the macropore structure. This phase separation method allows precise control of pore properties (e.g. pore size and pore volume) by simply changing the starting compositions and does not need any templates. However, compared to the several investigations on porous monolithic TiO_2 [58, 63−65], little has been investigated about the oxygen-deficient titania porous monoliths with electrical conductivity, where porous TiO_2 monoliths were utilized as precursors.

Outline of this work

In this study the author reports (i) new copper square lattice magnets from layered perovskite precursors via low-temperature ion-exchange and (ii) new oxygen-deficient, conducting titania materials via reduction of TiO_2 precursors, both in the form of film and macroporous monoliths.

In Chapter 1, the unusual magnetic properties are reported for $(CuCl)LaNb_2O_7$, obtained via solid state ion-exchange of $RbLaNb_2O_7$ precursor with $CuCl_2$ at low temperature (320 ºC). In this compound [CuCl] magnetic layers are separated by nonmagnetic $LaNb_2O_7$ perovskite blocks from neighboring [CuCl] layers; thus good two-dimensionality is expected. Specific heat measurements indeed show no magnetic ordering (i.e. spin-disordered state) down to as low as 2 K. Additionally, the value of

energy gap between the ground state and the first excited state was estimated to be about 20 K at zero field. In general, magnetic materials with an energy gap respond to the external magnetic field at the critical field corresponding to the gap size; here a magnetic transition from a spin-disordered to spin-ordered ground state occurs, and such magnetic response can be interpreted as Bose-Einstein condensation (BEC) of magnons. However, somewhat surprisingly, $(CuCl)LaNb_2O_7$ responds at a anomalously low magnetic field of about 10 T, almost as half as was expected (18 T) from the size of its zero-field gap.

In Chapter 2, the substitution effect in $(CuCl)LaNb_2O_7$ was investigated, where Nb^{5+} was replaced with Ta^{5+} ions i.e. $(CuCl)LaTa_2O_7$. Because of almost the same ionic radius of Ta^{5+} and Nb^{5+} (0.64 Å), it is expected that both compounds have the same magnetic interactions within the [CuCl] magnetic layer. However, it was revealed that the Ta compound exhibits a collinear (or stripe) antiferromagnetic order at T_N = 7 K, which indicates the presence of a magnetic interaction via nonmagnetic perovskite slabs. The solid solution system $(CuCl)La(Nb_{1-x}Ta_x)_2O_7$ was also successfully synthesized, where a spin-disordered ground state exists up to 40% Ta-substitution, while coexistence of spin-disordered ground state and stripe antiferromagnetic state was suggested for $x > 0.4$.

In Chapter 3, the synthesis of a new quadruple-layered (n = 4) perovskite $(CuCl)Ca_2NaNb_4O_{13}$ is described. Through a topotactic ion-exchange reaction with $CuCl_2$, the precursor $RbCa_2NaNb_4O_{13}$, presumably having incoherent octahederal tilting, changes into $(CuCl)Ca_2NaNb_4O_{13}$ with a $2a_p \times 2a_p \times 2c_p$ superstructure. Magnetic studies show the absence of long-range magnetic ordering down to 2 K despite strong in-plane interactions. Aleksandrov's group theory and Rietveld refinement of

synchrotron X-ray diffraction data suggest the structure to be of the *I*4/*mmm* space group with in-phase tilting along the *a* and *b* axes, or a two-tilt system (++0).

In Chapter 4, it is reported that the preparation and physical properties of reduced anatase $TiO_{2-\delta}$ thin films obtained via a low-temperature reduction using CaH_2 (below 500 ºC). The oxygen amounts were controlled in a wider range than previously reported. Some highly reduced anatase films showed resistivities as low as 10^{-3} Ω cm at room temperature, both in metallic and semiconducting states. The most conducting metallic sample has very high carrier concentration of 1.6×10^{21} cm^{-3}, comparable with those of metal-doped anatase films.

In Chapter 5, the development of macroporous monoliths of oxygen-deficient titania is presented: single phases of Ti_nO_{2n-1} with n = 2 (Ti_2O_3), 3 (Ti_3O_5), 4 (Ti_4O_7) and 6 (Ti_6O_{11}) were successfully obtained via the reduction of macroporous TiO_2 using a zirconium getter. The obtained porous monoliths retained the macropore properties of the TiO_2 precursors, i.e. uniform pore size distribution and relatively large porosity of about 60%, about three times larger than that of commercial Ebonex.

References

[1] J. G. Bednorz and K. A. Muller: Z. Phys. B: Condens. Matter **64** (1986) 189.

[2] R. J. Cava, B. Batlogg, C. H. Chen, E. A. Rietman, S. M. Zahurak, and D. Werder: Nature **329** (1987) 423.

[3] S. S. P. Parkin, V. Y. Lee, A. I. Nazzal, R. Savoy, R. Beyers, and S. J. La Placa: Phys. Rev. Lett. **61** (1988) 750.

[4] S. A. Sunshine, T. Siegrist, L. F. Schneemeyer, D. W. Murphy, R. J. Cava, B. Batlogg, R. B. van Dover, R. M. Fleming, S. H. Glarum, S. Nakahara, R. Farrow, J. J. Krajewski, S. M. Zahurak, J. V. Waszczak, J. H. Marshall, P. Marsh, L. W. Rupp, Jr., and W. F. Peck: Phys. Rev. B **38** (1988) 893.

[5] S. N. Putilin, E. V. Antipov, O. Chmaissem, and M. Marezio: Nature **362** (1993) 226.

[6] M. Azuma, Z. Hiroi, M. Takano, Y. Bando, and Y. Takeda: Nature **356** (1992) 775.

[7] A. Fujishima and X. Zhang: Comptes Rendus Chimie **9** (2005) 750.

[8] M. Yoshimura, S.-E. Yoo, M. Hayashi, and N. Ishizawa: Jpn. J. Appl. Phys. **28** (1989) L2007.

[9] H. Tabata, H. Tanaka, and T. Kawai: Appl. Phys. Lett. **65** (1994) 1970.

[10] K. J. Choi, M. Biegalski, Y. L. Li, A. Sharan, J. Schubert, R. Uecker, P. Reiche, Y. B. Chen, X. Q. Pan, V. Gopalan, L.-Q. Chen, D. G. Schlom, and C. B. Eom: Science **306** (2004) 1005.

[11] S. Jin, T. H. Tiefel, M. McCormack, R. A. Fastnacht, R. Ramesh, and L. H. Chen: Science **264** (1994) 413.

[12] T. Kimura, Y. Tomioka, H. Kuwahara, A. Asamitsu, M. Tamura, and Y. Tokura: Science **274** (1996) 1698.

[13] A. P. Ramirez: J. Phys.: Condense. Matter **9** (1997) 8171.

[14] M. Sugimoto: J. Am. Ceram. Soc. **82** (1999) 269.

[15] C. N. R. Rao and J. Gopalakrishnan: New direction in solid state chemistry, 2nd edition ed. (Cambridge University Press, 1997).

[16] R. E. Schaak and T. E. Mallouk: Chem. Mater. **14** (2002) 1455.

[17] K. G. Sanjaya Ranmohotti, E. Josepha, J. Choi, J. Zhang, and J. B. Wiley: Adv. Mater. **23** (2011) 442.

[18] M. Green: J. Mater. Sci.: Materials in Electronics **18** (2007) 15.

[19] K. Nakanishi and N. Tanaka: Acc. Chem. Res. **40** (2007) 863.

[20] A. R. Armstrong and P. G. Bruce: Nature **381** (1996) 499.

[21] M. Dion, M. Ganne, and M. Tournoux: Mater. Res. Bull. **16** (1981) 1429.

[22] M. Dion, M. Ganne, M. Tournoux, and J. Ravez: Rev. Chim. Miner. **21** (1984) 92.

[23] S. N. Ruddlesden and P. Popper: Acta Crystallogr. **10** (1957) 538.

[24] J. Gopalakrishnan and V. Bhat: Inorg. Chem. **26** (1987) 4299.

[25] T. A. Kodenkandath, J. N. Lalena, W. L. Zhou, E. E. Carpenter, C. Sangregorio, A. U. Falster, W. B. Simmons, C. J. O'Connor, and J. B. Wiley: J. Am. Chem. Soc. **121** (1999) 10743.

[26] T. A. Kodenkandath, A. S. Kumbhar, W. L. Zhou, and J. B. Wiley: Inorg. Chem. **40** (2001) 710.

[27] H. Kageyama, L. Viciu, G. Caruntu, Y. Ueda, and J. B. Wiley: J. Phys.: Condens. Matter **16** (2004) S585.

[28] K. Mizushima, P. C. Jones, P. J. Wiseman, and J. B. Goodenough: Mater. Res. Bull. **15** (1980) 783.

[29] A. K. Padhi, K. S. Nanjundaswamy, and J. B. Goodenough: J. Electrochem. Soc.

144 (1997) 1188.

[30] O. H. Hansteen, H. Fjellvag, and B. C. Hauback: J. Mater. Chem. **8** (1998) 2081.

[31] T. Moriga, O. Usaka, I. Nakabayashi, T. Kinouchi, S. Kikkawa, and F. Kanamaru: Solid State Ionics **79** (1995) 252.

[32] Y. Takeda, K. Kanno, T. Takada, O. Yamamoto, M. Takano, N. Nakayama, and Y. Bando: J. Solid State Chem. **63** (1986) 237.

[33] J. P. Hodges, S. Short, J. D. Jorgensen, X. Xiong, B. Dabrowski, S. M. Mini, and C. W. Kimball: J. Solid State Chem. **151** (2000) 190.

[34] J. C. Grenier, A. Wattiaux, J. P. Doumerc, P. Dordor, L. Fournes, J. P. Chaminade, and M. Pouchard: J. Solid State Chem. **96** (1992) 20.

[35] M. A. Hayward, M. A. Green, M. J. Rosseinsky, and J. Sloan: J. Am. Chem. Soc. **121** (1999) 8843.

[36] M. A. Hayward and M. J. Rosseinsky: Chem. Mater. **12** (2000) 2182.

[37] M. A. Hayward: Chem. Mater. **18** (2006) 321.

[38] M. A. Hayward: Chem. Mater. **17** (2005) 670.

[39] V. V. Poltavets, K. A. Lokshin, S. Dikmen, M. Croft, T. Egami, and M. Greenblatt: J. Am. Chem. Soc. **128** (2006) 9050.

[40] Y. Tsujimoto, C. Tassel, N. Hayashi, T. Watanabe, H. Kageyama, K. Yoshimura, M. Takano, M. Ceretti, C. Ritter, and W. Paulus: Nature **450** (2007) 1062.

[41] C. Tassel, J. M. Pruneda, N. Hayashi, T. Watanabe, A. Kitada, Y. Tsujimoto, H. Kageyama, K. Yoshimura, M. Takano, M. Nishi, K. Ohoyama, M. Mizumaki, N. Kawamura, J. Íñiguez, and E. Canadell: J. Am. Chem. Soc. **131** (2008) 221.

[42] H. Kageyama, T. Watanabe, Y. Tsujimoto, A. Kitada, Y. Sumida, K. Kanamori, K. Yoshimura, N. Hayashi, S. Muranaka, M. Takano, M. Ceretti, W. Paulus, C. Ritter,

and G. André: Angew. Chem. Intl. Edn. **47** (2008) 5740.

[43] S. Inoue, M. Kawai, Y. Shimakawa, M. Mizumaki, N. Kawamura, T. Watanabe, Y. Tsujimoto, H. Kageyama, and K. Yoshimura: Appl. Phys. Lett. **92** (2008) 161911.

[44] S. Inoue, M. Kawai, N. Ichikawa, H. Kageyama, W. Paulus, and Y. Shimakawa: Nat. Chem. **2** (2010) 213.

[45] M. Kawai, S. Inoue, M. Mizumaki, N. Kawamura, N. Ichikawa, and Y. Shimakawa: Appl. Phys. Lett. **94** (2009) 082102.

[46] G. Misguich and C. Lhuillier: Frustrated Spin Systems, edited by H. T. Diep (World Scientific, Singapore, 2004), p. 229.

[47] H. Kageyama, T. Kitano, N. Oba, M. Nishi, S. Nagai, K. Hirota, L. Viciu, J. B. Wiley, J. Yasuda, Y. Baba, Y. Ajiro, and K. Yoshimura: J. Phys. Soc. Jpn. **74** (2005) 1702.

[48] H. Kageyama, J. Yasuda, T. Kitano, K. Totsuka, Y. Narumi, M. Hagiwara, K. Kindo, Y. Baba, N. Oba, Y. Ajiro, and K. Yoshimura: J. Phys. Soc. Jpn. **74** (2005) 3155.

[49] N. Oba, H. Kageyama, T. Kitano, J. Yasuda, Y. Baba, M. Nishi, K. Hirota, Y. Narumi, M. Hagiwara, K. Kindo, T. Saito, Y. Ajiro, and K. Yoshimura: J. Phys. Soc. Jpn. **75** (2006) 113601.

[50] B. O'Regan and M. Gratzel: Nature **353** (1991) 737.

[51] Y. Matsumoto, M. Murakami, T. Shono, T. Hasegawa, T. Fukumura, M. Kawasaki, P. Ahmet, T. Chikyow, S. Koshihara, and H. Koinuma: Science **291** (2001) 854.

[52] Y. Furubayashi, T. Hitosugi, Y. Yamamoto, K. Inaba, G. Kinoda, Y. Hirose, T. Shimada, and T. Hasegawa: Appl. Phys. Lett. **86** (2005) 252101.

[53] S. D. Yoon, Y. Chen, A. Yang, T. L. Goodrich, X. Zuo, D. A. Arena, K. Ziemer, C. Vittoria, and V. G. Harris: J. Phys.: Condens. Matter **18** (2006) L355.

[54] N. Sbai, J. Perriere, B. Gallas, E. Millon, W. Seiler, and M. C. Bernard: J. Appl. Phys. **104** (2008) 033529.

[55] H. Tang, K. Prasad, R. Sanjines, P. E. Schmid, and F. Lévy: J. Appl. Phys. **75** (1994) 2042.

[56] J. R. Smith, F. C. Walsh, and R. L. Clarke: J. Appl. Electrochem. **28** (1998) 1021.

[57] F. C. Walsh and R. G. A. Wills: Electrochim. Acta **55** (2010) 6342.

[58] J. Konishi, K. Fujita, K. Nakanishi, K. Hirao, K. Morisato, S. Miyazaki, and M. Ohira: J. Chromatogr. A **1216** (2009) 7375.

[59] L. L. Hench: J. Am. Ceram. Soc. **74** (1991) 1487.

[60] M. Breulmann, S. A. Davis, S. Mann, H. P. Hentze, and M. Antonietti: Adv. Mater. **12** (2000) 502.

[61] X. Fan, H. Fei, D. H. Demaree, D. P. Brennan, J. M. St. John, and S. R. J. Oliver: Langmuir **25** (2009) 5835.

[62] Y. Chen, Y. Yi, J. D. Brennan, and M. A. Brook: Chem. Mater. **18** (2006) 5326.

[63] J. Konishi, K. Fujita, S. Oiwa, K. Nakanishi, and K. Hirao: Chem. Mater. **20** (2008) 2165.

[64] G. Hasegawa, K. Kanamori, K. Nakanishi, and T. Hanada: J. Sol-Gel Sci. Technol. **53** (2010) 59.

[65] G. Hasegawa, K. Kanamori, K. Nakanishi, and T. Hanada: J. Am. Ceram. Soc. **93** (2010) 3110.

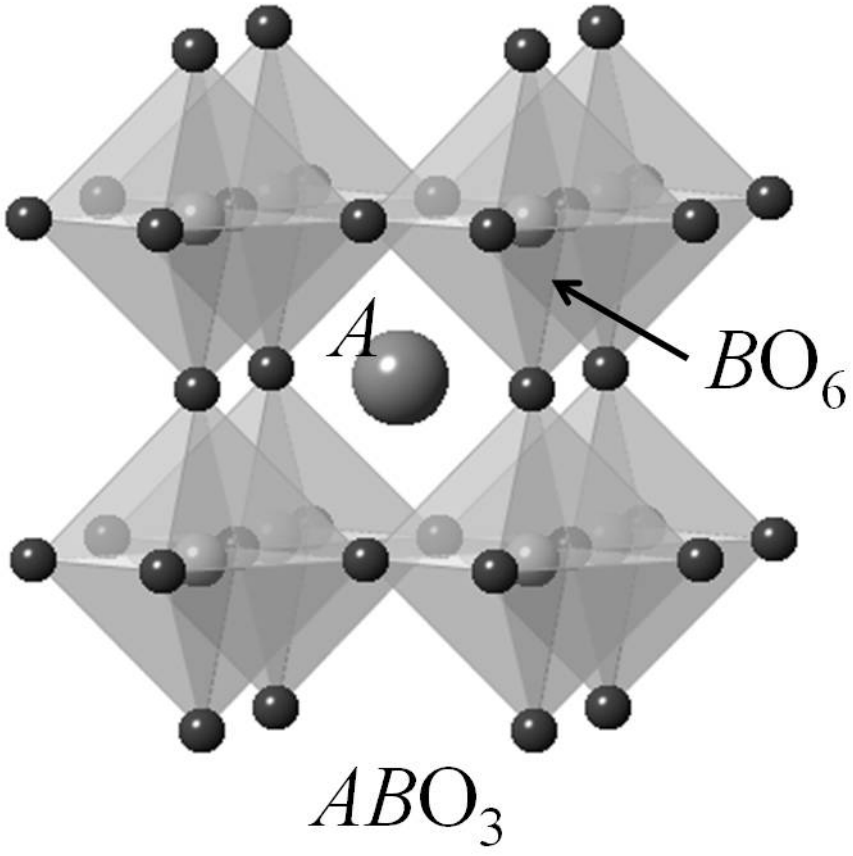

Figure 1. Schematic structure of a perovskite with *A* cation and BO_6 octahedra.

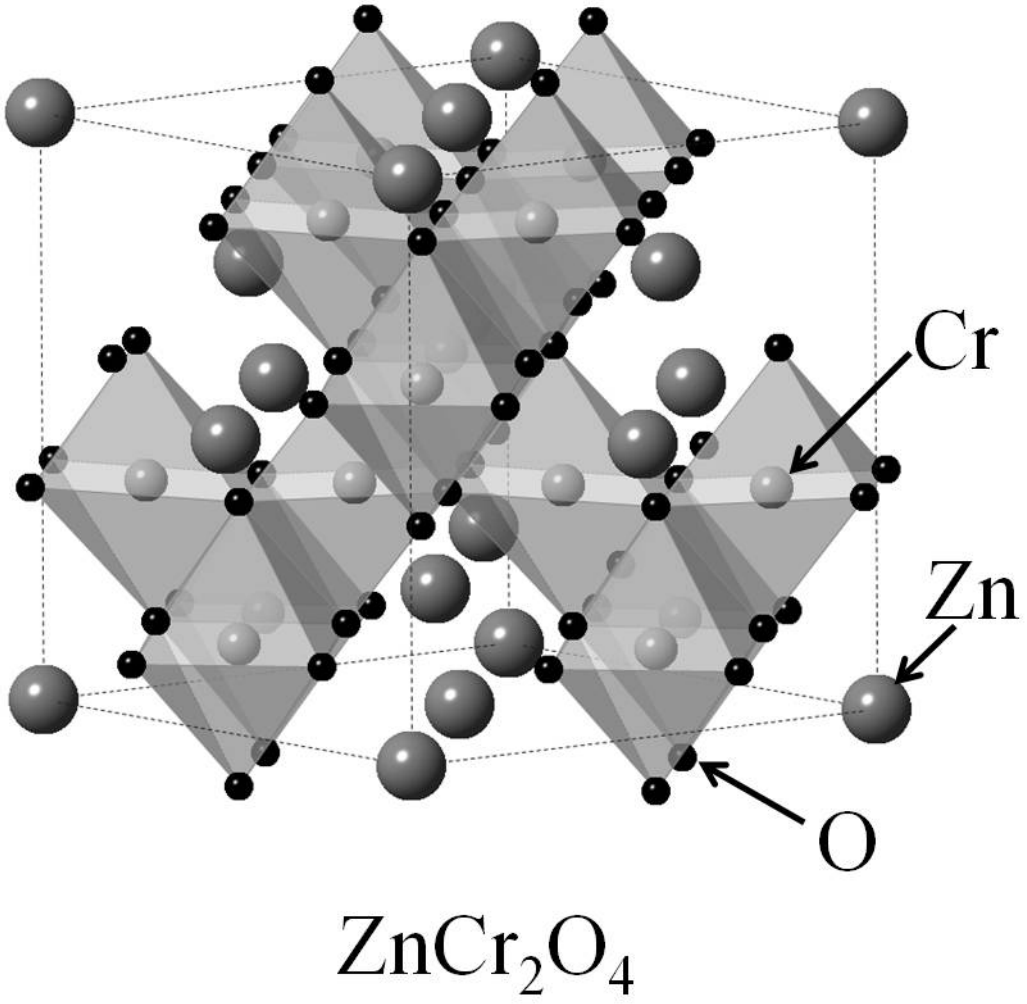

Figure 2. Schematic structure of a spinel $ZnCr_2O_4$.

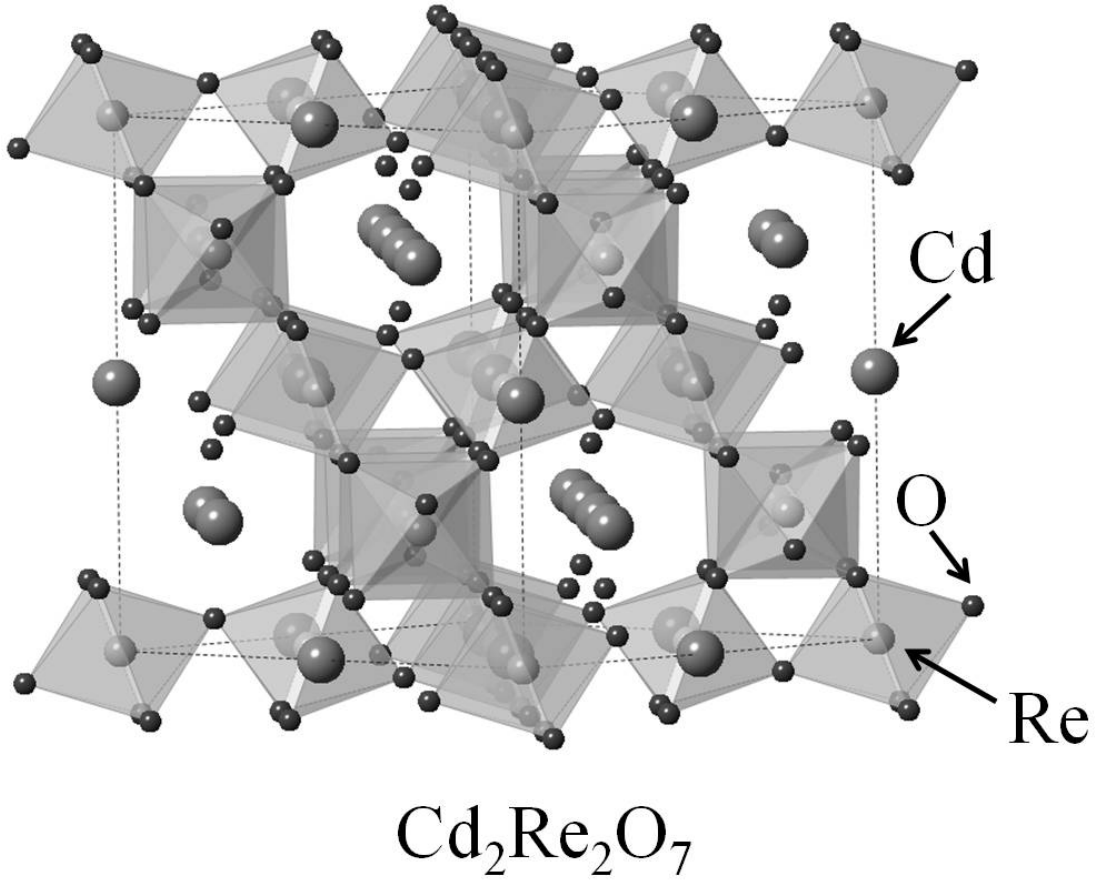

Figure 3. Clinographic representation of a pyrochlore $Cd_2Re_2O_7$.

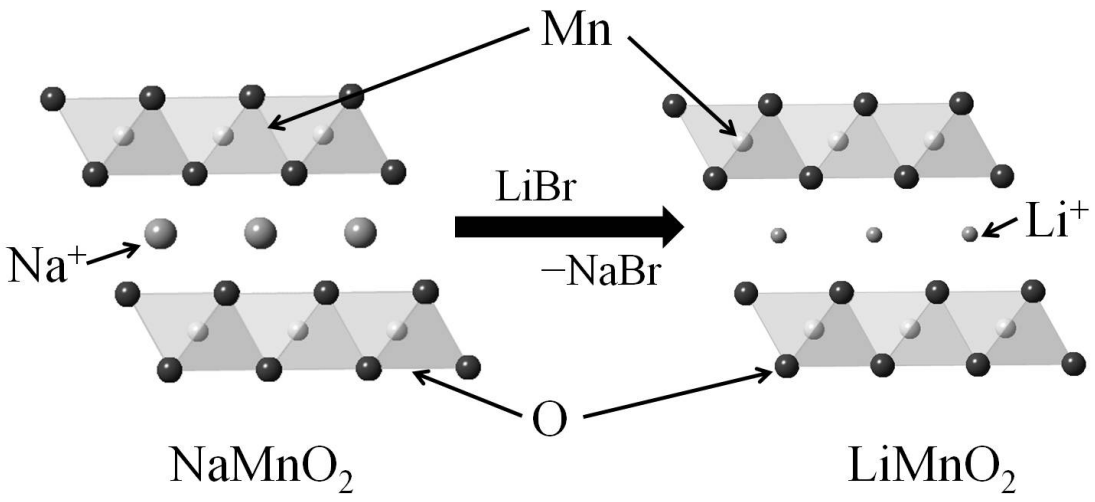

Figure 4. Schematic structure of $LiMnO_2$, obtained via exchange of sodium ions with lithium ions.

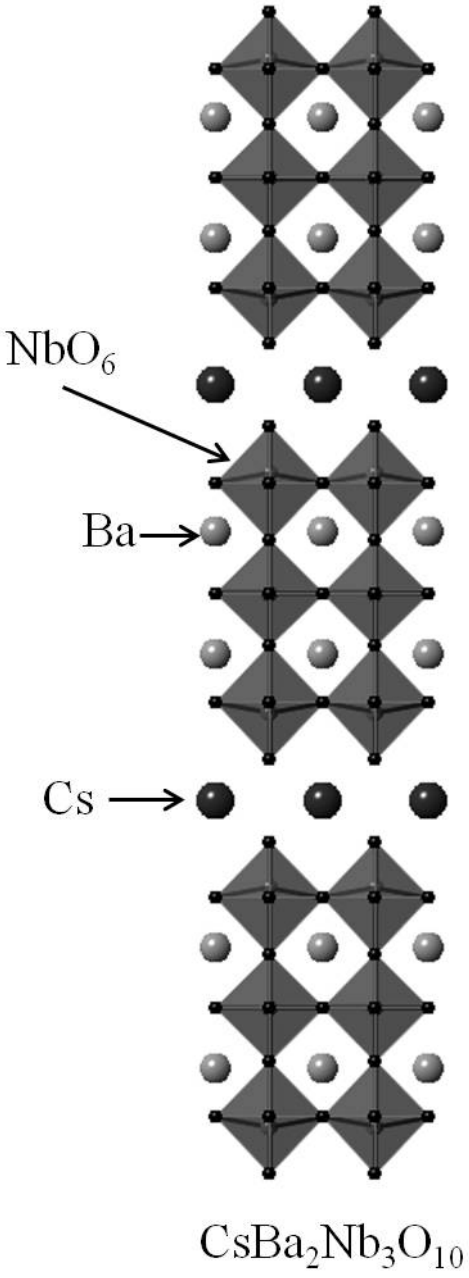

Figure 5. Schematic structure of a Dion-Jacobson phase $CsBa_2Nb_3O_{10}$.

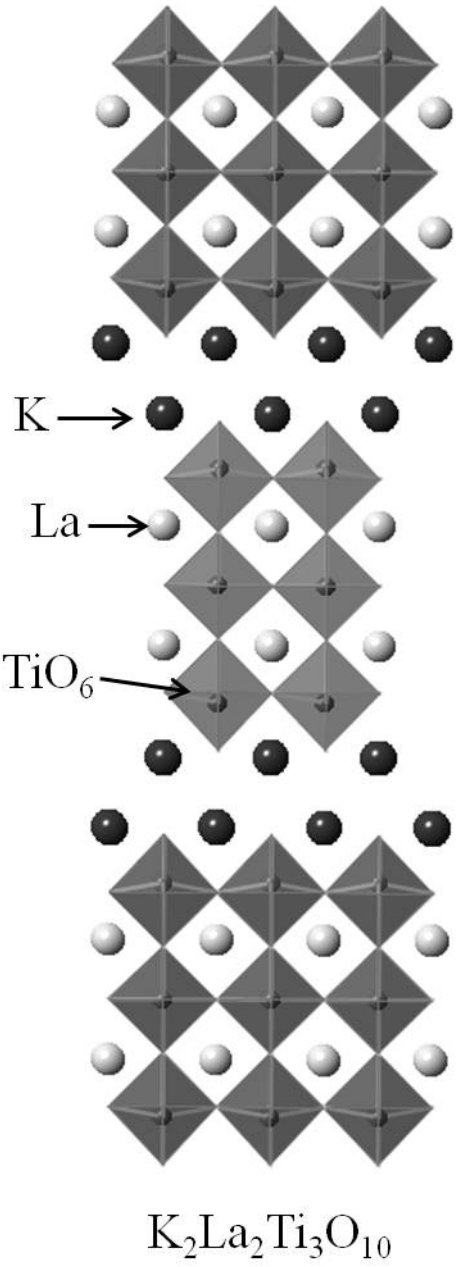

Figure 6. Schematic structure of a Ruddlesden-Popper phase $K_2La_2Ti_3O_{10}$.

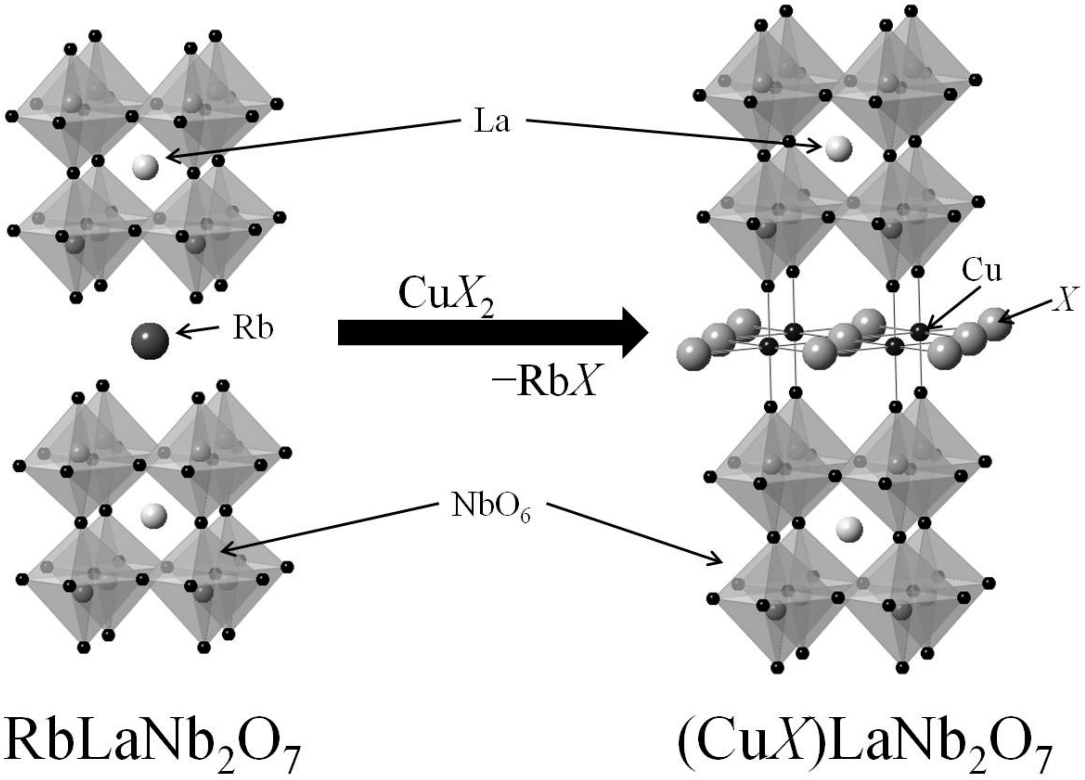

Figure 7. Structure of $(CuX)LaNb_2O_7$ (X = Cl, Br) (right) obtained via ion-exchange reaction using $RbLaNb_2O_7$ (left) as the precursor.

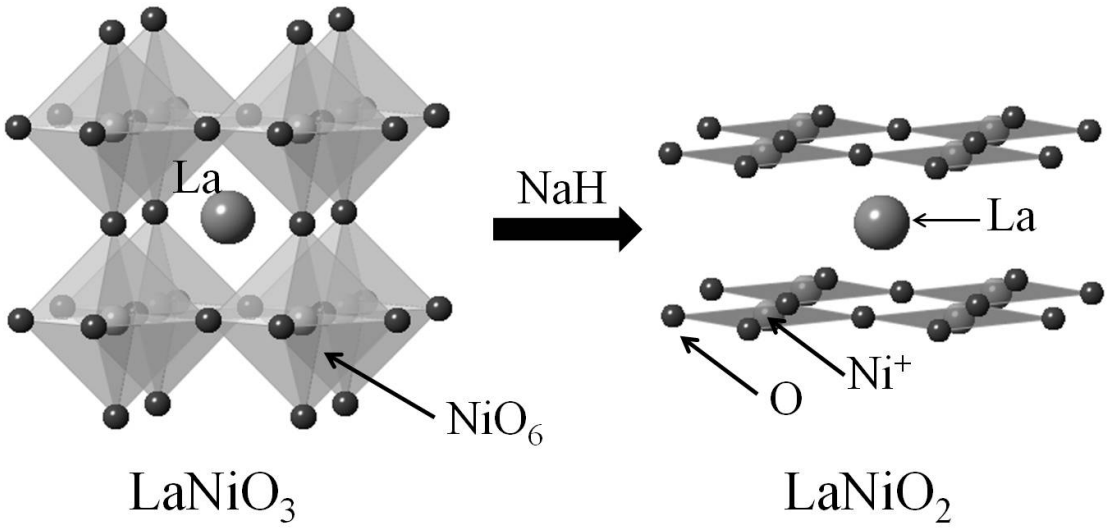

Figure 8. Structure of the square-planar nickelate $LaNiO_2$ obtained using NaH from the precursor compound, perovskite $LaNiO_3$.

Chapter 1. Bose-Einstein Condensation of Quasi-Two-Dimensional Frustrated Quantum Magnet $(CuCl)LaNb_2O_7$

1.1. Introduction

Response to an external stimulus i.e. magnetic field is called field-induced transition (FIT); FITs occur in Heisenberg antiferromagnetic spin systems, which, for various reasons, have a spin singlet ground state (i.e. spin-disordered ground state), separated by an energy gap Δ from the first excited triplet states. The application of magnetic fields decreases the separation between the ground state and the lowest branch (M_z = 1) of the triplet states and finally leads to a quantum phase transition at the critical field H_c (corresponding to $\Delta = g\mu_B H_c$). The ordered phase is described as a Bose-Einstein condensation (BEC) of bosons for which magnetic fields act as the chemical potential [1]. This concept is exclusively applicable to all known compounds

including $TlCuCl_3$ [1], $KCuCl_3$ [2], $Pb_2V_3O_9$ [3], $PbNi_2V_2O_8$ [4], $BaCuSi_2O_6$ [5], and $NiCl_2{\cdot}4SC(NH_2)_2$ [6]. Theoretically, a new route to the BEC has recently been proposed in the square-lattice frustrated model with modulating coupling constants, for which the two-magnon bound states condense above a certain magnetic field [7].

Chimie douce, solid-state reactions at relatively low temperatures, offer topochemical reactions which enable a rational design of the magnetic lattices in nonmolecular solids [8]. Recently, various exotic quantum magnetic phenomena have emerged from a new class of S = 1/2 layered copper oxyhalides $(CuX)A_{n-1}B_nO_{3n+1}$ (where $X = Cl^-$, Br^-; $A = La^{3+}$, Ca^{2+}, Na^+,…; $B = Nb^{5+}$, Ta^{5+}, Ti^{4+},…; n = 2, 3), obtained via low-temperature ion-exchange reactions [9−12]. They range from spin-disordered ground states in $(CuCl)LaNb_2O_7$ [13, 14], a collinear (or stripe) order at 32 K with a reduced magnetic moment in $(CuBr)LaNb_2O_7$ [15], to successive phase transitions and 1/3 magnetization plateaus in $(CuBr)Sr_2Nb_3O_{10}$ [16]. Common to this family, the CuX layer with an S = 1/2 square lattice is isolated by nonmagnetic perovskite slabs, making it a quasi-two-dimensional (quasi-2D) magnet. Within the layer, the halogen atom locates itself at the center of a copper square, so that the competition between first-nearest-neighbor and second-nearest-neighbor exchange couplings, denoted hereafter as J_1 and J_2, respectively, is expected. This situation differs markedly from the case of perovskite oxides ABO_3 with magnetic B sites that typically experience less frustration because the intervening superexchange anions are located at the edges of the square (or cube), resulting in dominating J_1 bonds.

From the previous studies, it is now revealed that $(CuCl)LaNb_2O_7$ has a spin singlet ground state with an energy gap, but there remain questions to be answered. Of particular interest is the unusual behavior under magnetic fields. Whereas the magnetic susceptibility at 0.1 T and inelastic neutron scattering (INS) experiments at 0 T have consistently yielded the zero-field gap Δ/k_B = 26.7 K (corresponding to H_c = 18.4 T) [13], the magnetization measurements at 1.3 K using pulsed fields have revealed the onset of magnetization at as low as 10.3 T [14]. However, a problem is that the magnetization increases slowly even in a field region below 10.3 T, most likely due to defects and/or unidentified magnetic impurities; the Curie tail is also detected in the magnetic susceptibility. Therefore, it is unfortunately uncertain whether the anomaly at

10.3 T can be truly attributed to the FIT or not. It may be a more complicated crossover behavior or just an extrinsic effect caused by the impurities. In the present study, the temperature variations of specific heat and magnetization measurements at static magnetic fields up to 14 T were performed. The obtained data not only indicate the absence of order-disorder transitions in the presence of a finite energy gap for lower fields but also provide evidence that the $(CuCl)LaNb_2O_7$ undergoes the FIT described by the magnon BEC, which is probably of a new type.

1.2. Experimental

1.2.1 Synthesis

The precursor phases $RbLaNb_2O_7$ were prepared via a conventional high-temperature route, using stoichiometric amounts of La_2O_3 (99.99% purity), Nb_2O_5 (99.99%), and 25% molar excess of Rb_2CO_3 (99.9%). $RbLaNb_2O_7$ was then mixed with a two-fold molar excess of ultra-dry $CuCl_2$ (99.999%) and pressed into pellets in an Ar-filled glove box (< 1ppm O_2/H_2O). The ion-exchange reactions expressed as

$$RbLaNb_2O_7 + CuCl_2 \rightarrow (CuCl)LaNb_2O_7 + RbCl \qquad (1.1)$$

were carried out in a sealed, evacuated ($< 4 \times 10^{-2}$ Pa) Pyrex tube at 320 °C for 7 days [13]. The final products were washed with distilled water to eliminate RbCl and excess $CuCl_2$, and dried at 120 °C.

1.2.2. Chemical characterization

The powder X-ray diffraction (XRD) data of the precursors and the final products were collected on a Mac Science M18XHF diffractometer equipped with a graphite monochromator and a CuKα source (λ = 1.5406 Å). The experiments were performed

on the 2theta range of 5−80º with an angular step of 0.02º and a counting time of 0.2 second per step.

1.2.3. Physical property measurements

To avoid the complexity arising from the dependence of the sample on the magnetic properties, the same sample used in previous measurements [13, 14] was employed. Specific heat measurements were performed by the heat relaxation method for $T > 2$ K and in magnetic fields up to $H = 14$ T in a Quantum Design QD-PPMS system. Further, 4.43 mg of (CuCl)$LaNb_2O_7$ powder was mixed with 2.34 mg of fine gold powder in order to improve thermal contact and pressed into a pellet. The pellet was attached to an alumina platform with a small amount of Apiezon N grease. The heat capacity was obtained by fitting a heat relaxation curve recorded after a heat pulse caused a temperature increase of approximately 2%. The heat capacity of the alumina platform and mixed gold powder was measured in separate runs without the sample and was subtracted from the data. The temperature dependence of magnetization was measured between 2 K and 20 K in fixed fields up to $H = 14$ T using the Quantum Design QD-PPMS system.

1.3. Results and Discussion

1.3.1. Chemical characterization

Figure 1.1 demonstrates room temperature XRD profiles of (CuCl)$LaNb_2O_7$ indicated a single phase product and was indexed to a tetragonal cell with the lattice constants $a = 3.879$ Å and $c = 11.754$ Å, consistent with those previously reported ($a = 3.879$ Å and $c = 11.728$ Å) [9]; additionally, the elongation along the c axis, ca. 0.7 Å relative to the precursor $RbLaNb_2O_7$, is consistent with the previous results [9], evidence for the insertion of a CuCl layer.

1.3.2 Magnetism

The total specific heat divided by the temperature (C/T) measured in the absence of

a magnetic field is plotted by black circles in Figure 1.1. The data display no trace of anomalies associated with the phase transitions. Instead, a Schottky anomaly was observed, i.e., a round maximum centered at around $T_{max} \sim 7$ K. This is a typical behavior of spin-singlet compounds with a finite gap to the lowest excited state and is consistent with the magnetic susceptibility and neutron scattering experiments [13]. It is not straightforward to extract a magnetic contribution C_M from the measured data because a nonmagnetic isomorph is not presently available from which the lattice contribution $C_L \sim \beta T^3$ in a low-temperature regime could be estimated. Therefore, a rough estimation is made and the result is indicated by the dotted line in Figure 1.1, where β is assumed as about 0.717 mJ/K^4 mol. The magnetic contribution is subsequently determined by subtracting the C_L term from C. By integrating C_M/T between 2 K and 30 K, 1.1 J/K mol was obtained. This value is approximately 13% smaller than the total magnetic entropy (Rln2) for 1 mol of S = 1/2 spins, but is acceptable considering the crude assumption of the lattice contribution.

For a spin-gapped compound in which the spin-singlet ground state is separated simply from the first excited one-magnon states by a gap Δ, the magnetic specific heat C_M in the low-temperature limit is, in general, given by the following expression [17]:

$$C_M = C_0 T^{-2} \exp(-\Delta/k_B T) \qquad (1.2)$$

where C_0 denotes constant. Thus, CT^2 is plotted against $1/T$ on the logarithmic scale, as shown in Figure 1.2. The fit with Δ/k_B = 19 K is also shown. This value is slightly smaller than that estimated by the magnetic susceptibility and neutron scattering experiment, Δ/k_B = 26.5 K. Alternatively, it is also possible to estimate the gap using the relation $k_B T_{max}/\Delta \sim 0.28$ in the isolated dimer limit [17]. Thus, the obtained value Δ/k_B = 25 K is closer to the values determined by magnetic susceptibility and neutron scattering studies. Similar values of the gap have been recently obtained by NMR [18]. It is noteworthy that a deviation from the temperature-activated behavior appears below 3 K (Figure 1.2), thereby leading to the ambiguity in the evaluation of the gap size because Equation 1.2 is more valid at lower temperatures. In fact, such a deviation is sometimes observed for spin-gapped materials [19, 20] and is ascribed to the phonon contribution or extrinsic effect involving defects and unidentified impurities. Recent

NMR experiments also show a deviation from the temperature activation curve at low temperatures, which are assigned as the extrinsic artifact factors from some nonmagnetic impurities.

As soon as the magnetic fields are applied up to 7 T, the broad maximum of C/T shifts gradually to a lower temperature, indicating not only the absence of order-disorder transitions but also a reduction in the energy gap $\Delta(H)$ with the field. A deviation from the temperature activation behavior is again appreciable below 3 K (not shown). The concave temperature dependence of the specific heat at low temperatures below 7 T reflects the spin-singlet nature of the ground state. However, it changes to a linear behavior at 10 T. Finally, the most spectacular feature of the present study is observed: a cusp-like peak in $C(T)$ at and above 11 T, which is the first evidence of a field-induced phase transition in this compound. The transition temperature T_N at 11 T is 2.3 K, as indicated by the arrow in the inset of Figure 1.1. When the magnetic field is further increased, the peak associated with the phase transition develops and shifts systematically to higher temperatures, and T_N becomes 3.3 K at 14 T. The FITs observed here are nearly consistent with the abrupt increase in the magnetization at 10.3 T [14]. Therefore, it is natural to consider that the FIT should be of magnetic origin associated with the BEC of magnons.

In order to validate this theory, the temperature dependence of magnetization was measured at various constant magnetic fields shown in Figure 1.3. While the $M(T)$ curves at 6 T, 8 T, and 10 T are featureless, those above 10 T signal magnetic phase transitions as cusp-like anomalies. In Figure 1.4, the field dependence of T_N is summarized in a temperature vs. magnetic field phase diagram. It is seen that T_N's determined by $C(T)$ and $M(T)$ are in good agreement with each other. Furthermore, both the increase in magnetization for decreasing temperature below T_N and the growth of the peak of the specific heat around T_N with increasing magnetic field can be attributed to the increased magnon density on the basis of the BEC scenario. From these results, it is concluded that $(CuCl)LaNb_2O_7$ is a new experimental correspondence of the BEC of magnons.

Figure 1.5 shows a theoretical curve of the Hartree-Fock approximation that gives the power law behavior

$$H_c(T) - H_c(0) = A_0 T^{\phi} \quad (1.3)$$

with a constant A_0 and the critical exponent ϕ = 3/2. Here, $H_c(0)$ = 9.0 T is assumed. The result *appears* to follow the theory. Note, however, that the fitted results largely depend on the choice of $H_c(0)$. Accurate determination of Δ is also hampered by rather broadened anomalies at T_N, probably due to the use of the polycrystalline specimen. Thus, quantitative discussions on the criticality require future experimental investigation with single crystals and at lower temperatures.

The most remarkable implication of the author's findings is that $(CuCl)LaNb_2O_7$ undergoes the magnon BEC at a surprisingly small magnetic field around 10 T, far below the critical field estimated from the zero-field gap. This markedly contrasts with other known experimental examples, in which the occurrence of the BEC is directly linked to the level crossing between the spin-singlet ground state and the low-lying excited one-magnon state [1−6]. That is, for $(CuCl)LaNb_2O_7$, the one-magnon states are at least not directly responsible for the BEC. One possibility is that two-magnon bound states reach the ground state at 10 T and drive the transition into a gapless spin-liquid state without transverse magnetic moment (spin-nematic state), as proposed theoretically for a quadrumerized 2D square-lattice antiferromagnet by Ueda and Totsuka [7]. Here, a key requirement for the spin-nematic order is the competition between ferromagnetic and antiferromagnetic interactions. Because the Weiss temperature (−9.6 K) has a much smaller magnitude than the temperature at maximum susceptibility (16.5 K), $(CuCl)LaNb_2O_7$ meets this requirement and thus may be the first experimental correspondence of this model. Historically, the BEC scenario of the two-magnon bound states was for the first time considered for the Shastry-Sutherland model with antiferromagnetic intra- and interdimer interactions [21]. However, unfortunately, the additional Dzyaloshinsky-Moriya interaction in the experimental counterpart $SrCu_2(BO_3)_2$ causes bending of these modes in the energy vs. field diagram and eventually drives the spin-singlet phase to the 1/8 plateau phase [22]. In the case of $(CuCl)LaNb_2O_7$, the magnon binding may be more favored because of the presence of ferromagnetic interactions. Whether this scenario or some other explains the BEC in this compound is an interesting issue that will be analyzed in the future.

1.4. Conclusion

In conclusion, the temperature variations of the specific heat and magnetization were measured for $(CuCl)LaNb_2O_7$. The results provide evidence that the BEC occurs at as low as 10 T. On the basis of a comparison with previous zero- and low-field experiments, the author strongly believes that the one-magnon excitations do not play the main role in the field-induced transition, thus providing a new mechanism that leads to the BEC. It seems that frustrated quantum spin systems with antiferromagnetic and ferromagnetic interactions hardly receive attention, with only limited theoretical studies [7, 23]. Experimentally, the present compound together with its family [15, 16] would provide suitable opportunities to investigate novel quantum phenomena including the BEC for systems with mixed interactions.

References

[1] T. Nikuni, M. Oshikawa, A. Oosawa, and H. Tanaka: Phys. Rev. Lett. **84** (2000) 5868.

[2] A. Oosawa, T. Takamatsu, K. Tatani, H. Abe, N. Tsujii, O. Suzuki, H. Tanaka, G. Kido, and K. Kindo: Phys. Rev. B **66** (2002) 104405.

[3] T. Waki, Y. Morimoto, C. Michioka, M. Kato, H. Kageyama, K. Yoshimura, S. Nakatsuji, O. Sakai, Y. Maeno, H. Mitamura, and T. Goto: J. Phys. Soc. Jpn. **73** (2004) 3435.

[4] N. Tsujii, O. Suzuki, H. Suzuki, H. Kitazawa, and G. Kido: Phys. Rev. B **72** (2005) 104402.

[5] S. E. Sebastian, N. Harrison, C. D. Batista, L. Balicas, M. Jaime, P. A. Sharma, N. Kawashima, and I. R. Fisher: Nature **441** (2006) 617.

[6] V. S. Zapf, D. Zocco, B. R. Hansen, M. Jaime, N. Harrison, C. D. Batista, M. Kenzelmann, C. Niedermayer, A. Lacerda, and A. Paduan-Filho: Phys. Rev. Lett. **96** (2006) 077204.

[7] H. T. Ueda and K. Totsuka: Phys. Rev. B **76** (2007) 214428.

[8] A. Stein, S. W. Keller, and T. E. Mallouk: Science **259** (1993) 1558.

[9] T. A. Kodenkandath, J. N. Lalena, W. L. Zhou, E. E. Carpenter, C. Sangregorio, A. U. Falster, W. B. Simmons, Jr., C. J. O'Connor, and J. B. Wiley: J. Am. Chem. Soc. **121** (1999) 10743.

[10] T. A. Kodenkandath, A. S. Kumbhar, W. L. Zhou, and J. B. Wiley: Inorg. Chem. **40** (2001) 710.

[11] H. Kageyama, L. Viciu, G. Caruntu, Y. Ueda, and J. B. Wiley: J. Phys.: Condens.

Matter **16** (2004) S590.

[12] H. Kageyama, T. Kitano, R. Nakanishi, J. Yasuda, N. Oba, Y. Baba, M. Nishi, Y. Ueda, Y. Ajiro, and K. Yoshimura: Prog. Theor. Phys. Suppl. **159** (2005) 39.

[13] H. Kageyama, T. Kitano, N. Oba, M. Nishi, S. Nagai, K. Hirota, L. Viciu, J. B. Wiley, J. Yasuda, Y. Baba, Y. Ajiro, and K. Yoshimura: J. Phys. Soc. Jpn. **74** (2005) 1702.

[14] H. Kageyama, J. Yasuda, T. Kitano, K. Totsuka, Y. Narumi, M. Hagiwara, K. Kindo, Y. Baba, N. Oba, Y. Ajiro, and K. Yoshimura: J. Phys. Soc. Jpn. **74** (2005) 3155.

[15] N. Oba, H. Kageyama, T. Kitano, J. Yasuda, Y. Baba, M. Nishi, K. Hirota, Y. Narumi, M. Hagiwara, K. Kindo, T. Saito, Y. Ajiro, and K. Yoshimura: J. Phys. Soc. Jpn. **75** (2006) 113601.

[16] Y. Tsujimoto, Y. Baba, N. Oba, H. Kageyama, T. Fukui, Y. Narumi, K. Kindo, T. Saito, M. Takano, Y. Ajiro, and K. Yoshimura: J. Phys. Soc. Jpn. **76** (2007) 063711.

[17] R. L. Carlin: Magnetochemistry (Springer-Verlag, Berlin, 1986).

[18] M. Yoshida, N. Ogata, M. Takigawa, J. Yamaura, N. Oba, T. Kitano, H. Kageyama, Y. Ajiro, and K. Yoshimura: J. Phys. Soc. Jpn. **76** (2007) 104703.

[19] H. Kageyama, K. Onizuka, Y. Ueda, M. Nohara, H. Suzuki, and H. Takagi: J. Exp. and Theor. Phys. **90** (2000) 129.

[20] P. R. Hammar, D. H. Reich, C. Broholm, and F. Trouw: Phys. Rev. B **57** (1998) 7846.

[21] T. Momoi and K. Totsuka: Phys. Rev. B **62** (2000) 15067.

[22] H. Nojiri, H. Kageyama, Y. Ueda, and M. Motokawa: J. Phys. Soc. Jpn. **72** (2003) 3243.

[23] N. Shannon, T. Momoi, and P. Sindzingre: Phys. Rev. Lett. **96** (2006) 02713.

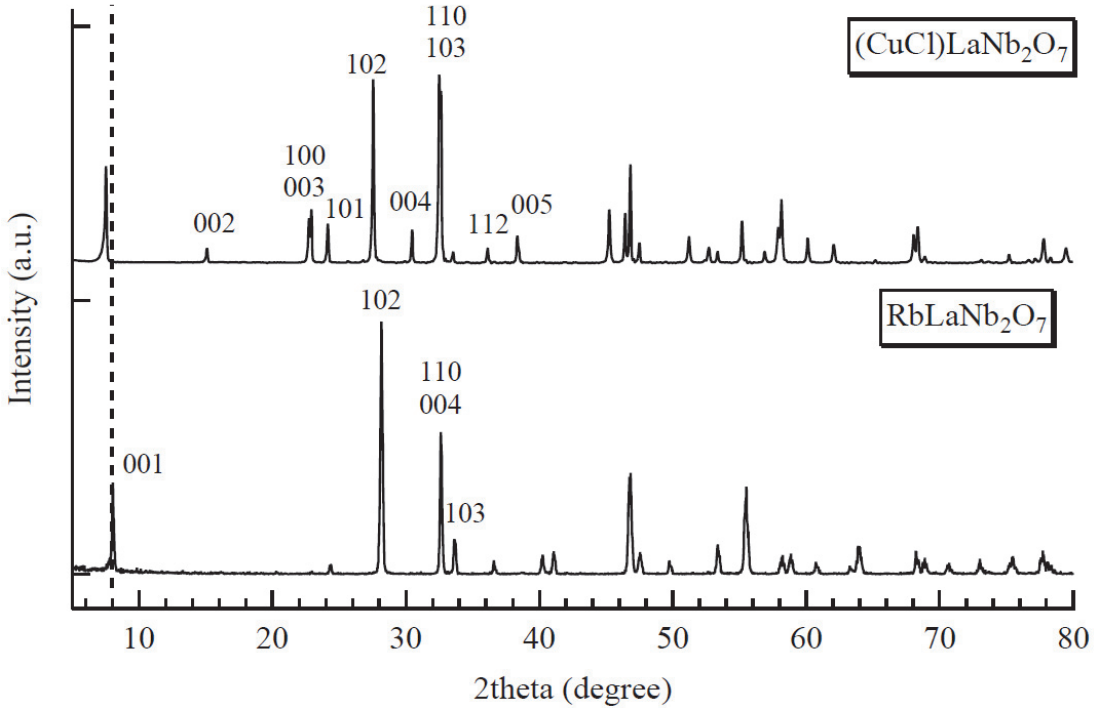

Figure 1.1. Laboratory X-ray diffraction patterns of $RbLaNb_2O_7$ and $(CuCl)LaNb_2O_7$ at room temperature. Dotted lines are guide to the eye.

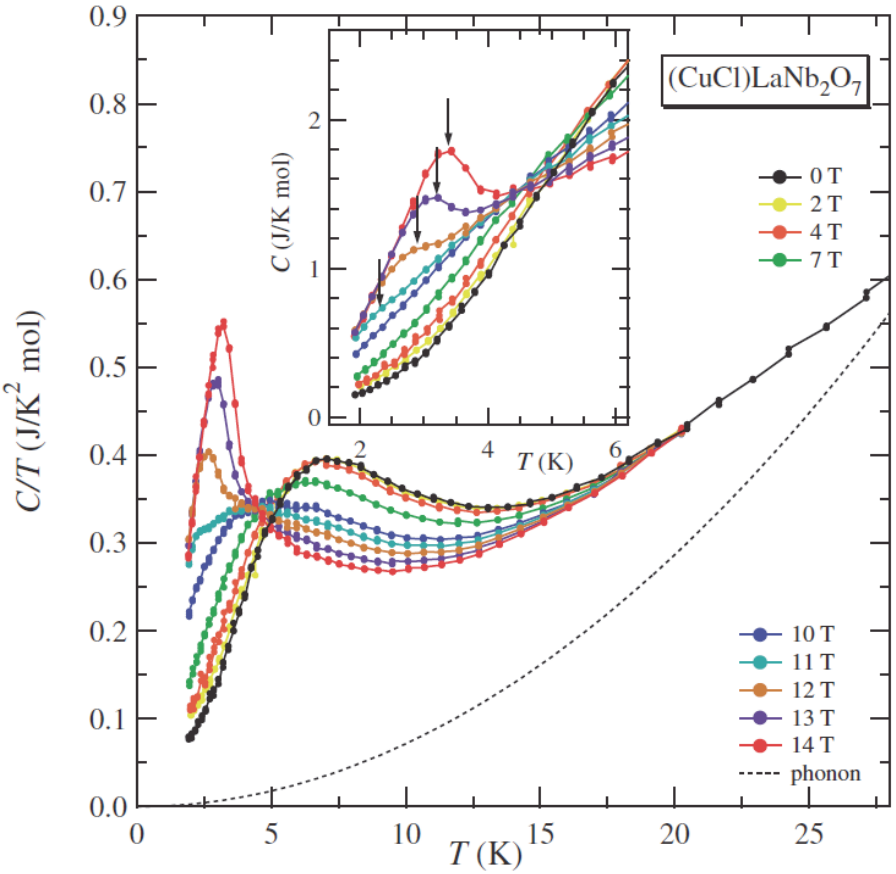

Figure 1.2. Specific heat divided by temperature (C/T) for $(CuCl)LaNb_2O_7$ collected with fields of H = 0 T, 2 T, 4 T, 7 T, 10 T, 11 T, 12 T, 13 T, and 14 T. The dotted curve represents the phonon contribution assumed as $C_L \sim \beta T^3$ (β = 0.717 mJ/K^4 mol). The inset shows the C vs. T plots in the low-temperature region, where arrows denote the transition temperatures.

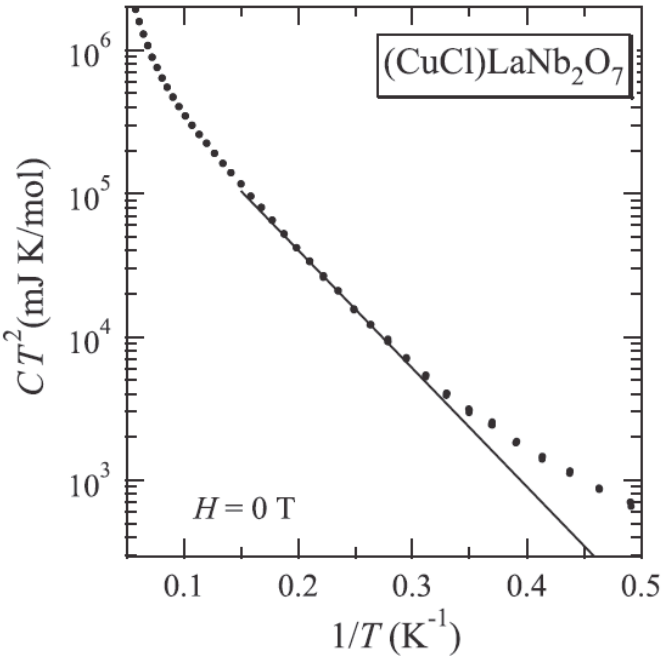

Figure 1.3. Logarithmic plot of CT^2 as a function of $1/T$ for $H = 0$ T. The solid line represents the fit to Equation 1.2.

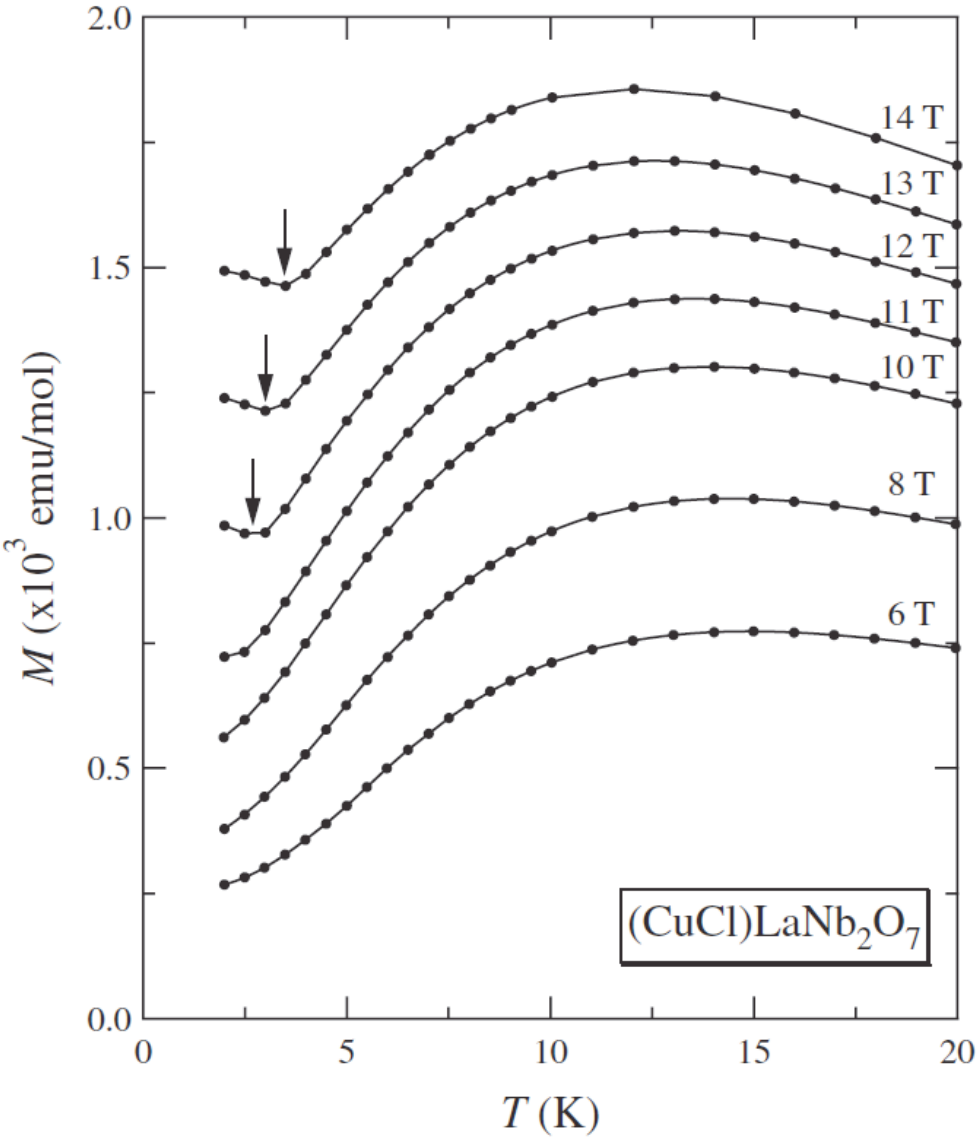

Figure 1.4. Low-temperature magnetizations of $(CuCl)LaNb_2O_7$ measured at various external magnetic fields up to 14 T.

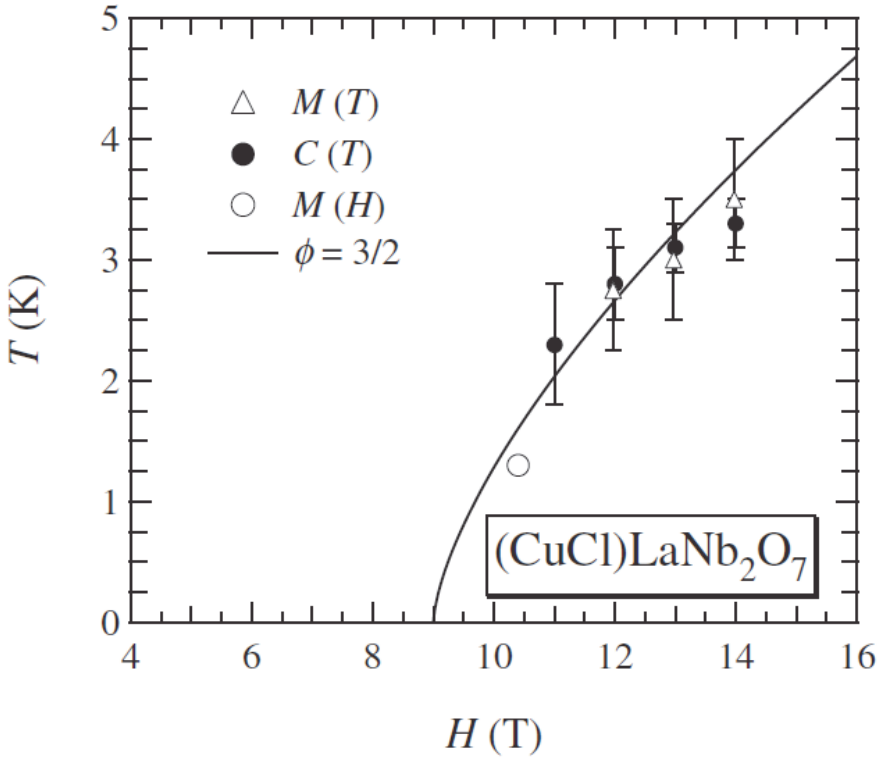

Figure 1.5. Phase boundary in (CuCl)$LaNb_2O_7$ determined from the results of $M(T)$ (triangles), $C(T)$ (solid circles). The open circle represents the critical field determined by the magnetization curve at 1.3 K [14]. The solid line represents a theoretical curve described in the text.

Chapter 2. Quantum Phase Transition in (CuCl)La($Nb_{1-x}Ta_x$)$_2O_7$

2.1. Introduction

Phenomena driven by quantum fluctuations in the vicinity of a quantum critical point in two-dimensional (2D) systems are one of the most important topics in modern physics. Motivated by the discovery of the 2D S = 1/2 spin correlation in high-T_c superconducting cuprates, 2D quantum spin insulators based on the square-lattice and its analogues have been searched for and extensively investigated. The examples include the J_1-J_2 lattice (where J_1 and J_2 denote the first-nearest-neighbor and second-nearest-neighbor exchange constants) such as $Li_2VO(Si, Ge)O_4$ [1], the checkerboard lattice $A_2F_2Fe_2OQ_2$ (A = Sr, Ba; Q = S, Se) [2], the 1/5 depleted square lattice CaV_4O_9 [3], and the Shastry-Sutherland lattice $SrCu_2(BO_3)_2$ [4]. Although those

studies have revealed intriguing properties like a spin-disordered state and quantized magnetization plateaus to name only a few [3−5], there are still many open issues left unsolved and therefore further search for compounds and systematic studies are required for global understanding of quantum fluctuations in 2D systems.

$(CuCl)LaNb_2O_7$ is an $S = 1/2$ square-lattice based antiferromagnet, where the magnetic CuCl layers are sandwiched by non-magnetic $LaNb_2O_7$ blocks (Figure 2.1). This material has a spin-disordered ground state and an excitation gap at zero field of $\Delta_{ZF} = 2.3$ meV. The triplet excitations are nearly Q-independent despite the apparent 2D crystal structure [6]. Furthermore, field-induced magnetic order occurs at a remarkably smaller magnetic field of $H_{c1} \sim 10$ T than that expected from Δ_{ZF} [7−9]. The loss of the tetragonal symmetry and thus the deviation from the idealized J_1-J_2 model is suggested from the nuclear magnetic resonance (NMR) studies [9]. By contrast, $(CuBr)LaNb_2O_7$ exhibits collinear (or stripe) antiferromagnetic (CAF) order at a Néel temperature of $T_N = 32$ K with a propagation vector $q = (\pi, 0, \pi)$ [10]. Common to the two compounds, there exist competing antiferromagnetic and ferromagnetic interactions. Recent studies on a solid solution $(CuCl_{1-y}Br_y)LaNb_2O_7$ have revealed magnetic order by 5%-Br substitution [11, 12]. However, it is noteworthy that the Br-for-Cl substitution with different ionic radii (1.82 Å for Br^- and 1.67 Å for Cl^- [13]) is subject to direct and considerable disorder of the CuCl layer itself. Not only the ratio of superexchange constants but also chemical disorder might play a significant role in driving the phase transition.

In this paper the magnetic properties of $(CuCl)La(Nb_{1-x}Ta_x)_2O_7$ were investigated by means of susceptibility, pulsed high-field magnetization, and elastic/inelastic neutron scattering measurements. A crucial advantage of the Ta-for-Nb substitution over the

Br-for-Cl substitution is that the magnetic CuCl plane is preserved and that pentavalent Nb and Ta ions have almost the same radius (0.64 Å) [13]. The present study has been performed in parallel with the muon spin relaxation (μSR) measurements of the $(CuCl_{1-y}Br_y)LaNb_2O_7$ and $(CuCl)La(Nb_{1-x}Ta_x)_2O_7$ systems [12].

2.2. Experimental

2.2.1 Synthesis

The precursor phases $RbLa(Nb_{1-x}Ta_x)_2O_7$ (x = 0, 0.2, 0.3, 0.4, 0.6, 0.8 and 1.0) were prepared via a conventional high-temperature route, using stoichiometric amounts of La_2O_3 (99.99% purity), Nb_2O_5 (99.99%), Ta_2O_5 (99.99%) and 25% molar excess of Rb_2CO_3 (99.9%). $RbLa(Nb_{1-x}Ta_x)_2O_7$ was then mixed with a two-fold molar excess of ultra-dry $CuCl_2$ (99.999%) and pressed into pellets in an Ar-filled glove box (< 1ppm O_2/H_2O). The ion-exchange reactions expressed as

$$RbLa(Nb_{1-x}Ta_x)_2O_7 + CuCl_2 \rightarrow (CuCl)La(Nb_{1-x}Ta_x)_2O_7 + RbCl \qquad (2.1)$$

were carried out in a sealed, evacuated (< 4×10^{-2} Pa) Pyrex tube at 320 °C for 7 days [14]. The final products were washed with distilled water to eliminate RbCl and excess $CuCl_2$, and dried at 120 °C.

2.2.2 Chemical characterization

The powder X-ray diffraction (XRD) data of the precursors and the final products were collected on a Mac Science M18XHF diffractometer equipped with a graphite

monochromator and a CuKα source (λ = 1.5406 Å). The experiments were performed on the 2theta range of 5−80º with an angular step of 0.02º and a counting time of 0.2 second per step.

To check the chemical homogeneity in the solid solution system, energy-dispersive spectroscopy (EDS) was carried out at ambient temperature using a JEM2010F system with an operating voltage of 200 kV at the Institute for Solid State Physics (ISSP) at the University of Tokyo. The specimen was finely ground in methanol and then placed on a Cu microgrid mesh for TEM observations.

2.2.3 Magnetism

Magnetic susceptibilities were measured using a SQUID magnetometer (Quantum Design, MPMS) over the temperature range T = 2−300 K in a magnetic field H of 2 T. High-field magnetization measurements up to 57 T were conducted using a pulsed magnet installed at ISSP. Elastic and inelastic neutron scattering experiments were performed using the ISSP-PONTA triple-axis spectrometer (5G), installed at the JRR-3 reactor at the Japan Atomic Energy Agency (JAEA), Tokai. Powder samples (x = 0.3, 0.6, 0.8 and 1.0) of about 20 g each were put into aluminum cylinders. Neutrons with a wavelength of 2.358 Å were obtained from the 002 reflection of pyrolytic graphite (PG), and a horizontal collimation of open-40'-sample-80'-80' in combination with a PG filter was placed before the sample to eliminate higher-order beam contamination.

2.3. Results and Discussion

2.3.1. Chemical characterization

Room-temperature XRD profiles of $(CuCl)LaNb_2O_7$ and $(CuCl)LaTa_2O_7$ were indexed to a tetragonal cell with nearly the same lattice constants (a = 3.879 Å, c = 11.754 Å for Nb, and a = 3.879 Å, c = 11.748 Å for Ta), consistent with those previously reported [14, 15]. No trace of impurity phases were found. The XRD patterns of the $0 < x < 1$ samples at room temperature demonstrated successful synthesis of the solid solution having nearly the same tetragonal cell parameters as those of $(CuCl)LaNb_2O_7$ and $(CuCl)LaTa_2O_7$. The quality of the XRD patterns is as good as that of the end members. In addition, as a typical example, the TEM image of the x = 0.8 sample is shown in Figure 2.1 (b) and the corresponding EDS spectrum in Figures 2.1 (c), (d), which demonstrates a uniform distribution of the Nb and Ta atoms.

2.3.2. Magnetism

Shown in Figure 2.2 are the magnetic susceptibilities χ for all the samples. χ of $(CuCl)LaTa_2O_7$ (x = 1) above 50 K was fitted to the Curie-Weiss law,

$$\chi = C/(T - \theta) \tag{2.2}$$

where C and θ represent the Curie constant and the Weiss temperature, respectively. The value of C of 0.410 emu K/mol suggests the completion of the designed ion-exchange reaction (Equation 2.1). The value of θ of −1.2 K is about 1/8 of what was obtained for x = 0 (−9.6 K) [6]. This does not simply mean much reduced magnetic interactions because the susceptibility has a broad maximum at T^{χ}_{max} = 11.5 K. This is a characteristic feature of low-dimensional magnetic materials, indicating that a dominant antiferromagnetic interaction is of same order of the magnitude as in x = 0. The

observed T^{χ}_{max} does not differ so much from that of $x = 0$ (16.5 K). However, unlike χ for $x = 0$ having a sharp drop due to spin-singlet formation, χ for $x = 1.0$ exhibits only a slight decrease below T^{χ}_{max}, followed by a Curie tail, presumably due to paramagnetic impurities and defects. Thus a magnetic ground state is expected for $x = 1.0$.

This speculation is supported by the magnetization measurements at 1.3 K (see Figure 2.3). While the magnetization curve for $x = 0$ remains zero until the field-induced magnetic order occurs at H_c, apart from a tiny magnetization coming from a small amount of impurities/defects [7, 9], the magnetization curve for $x = 1.0$ has a sizable slope even in low fields.

In order to probe probable magnetic order, neutron powder diffraction measurements were performed at zero magnetic field as shown in Figure 2.4 (a). A peak was found at around 18° corresponding to the (1/2, 0, 1/2) magnetic reflection. Hence, it is natural to consider that (CuCl)$LaTa_2O_7$ exhibits CAF order as in (CuBr)$LaNb_2O_7$ [10]. The ordered magnetic moment was estimated to be 0.69(10) μ_B, which is comparable to that of (CuBr)$LaNb_2O_7$ (0.60(11) μ_B). However, the T dependence of the intensity of this reflection (Figure 2.4 (d)) revealed that the transition temperature 7 K is much smaller than that for (CuBr)$LaNb_2O_7$ (32 K). The magnetization curve for $x = 1.0$ becomes very nonlinear compared with the normalized one for (CuBr)$LaNb_2O_7$ (Figure 2.3), suggesting that the effect of quantum fluctuations should be considerably stronger in the former material.

The author wish to recall here that the cell parameters of (CuCl)$LaTa_2O_7$ and (CuCl)$LaNb_2O_7$ are almost the same. Therefore, if the LaB_2O_7 perovksite slabs acted simply as *spacers* that spatially and magnetically isolated the CuCl layers, the magnetic properties of the two compounds would be identical. The present result indicates that

superexchange interactions through Cu-BO$_6$-BO$_6$-Cu (B = Nb, Ta) play an important role as well as those through Cu-X-Cu in the magnetic properties. This is compatible with the observations that the unpaired electron of Cu^{2+} ion occupies the $d(3z^2 - r^2)$ orbital pointing parallel to the c axis [9] and that the stability of the 1/3 magnetization plateau in (CuBr)$A_2B_3O_{10}$ (A = Ca, Sr, Ba, Pb) is tuned by substituting different atoms in the B site [16]. The cases in which $d(3z^2 - r^2)$ orbitals align perpendicular to the magnetic layers is also found in the S = 1/2 honeycomb antiferromagnet $InCu_{2/3}V_{1/3}O_3$, where superexchange interactions via InO_6 are expected to influence its magnetic properties [17].

Once it was confirmed that the two isostructural compounds had different ground states (i.e. spin-singlet and CAF states), the magnetic phase diagram in (CuCl)La($Nb_{1-x}Ta_x$)$_2O_7$ was investigated. Systematic evolution of the magnetic susceptibilities and the magnetization curves is shown as a function of x in Figure 2.2 and Figure 2.3, respectively. For example, the samples with higher x (from 0, 0.2, 0.4, 0.6, 0.8 to 1.0) have lower T^{χ}_{max} (16.5 K, 15.4 K, 14.2 K, 13.2 K, 12.5 K and 11.5 K, respectively). The value of θ, derived from Curie-Weiss fitting to the susceptibility data, also gradually decreases with x (θ = −9.6 K, −5.6 K, −3.8 K, −3.1 K, −2.5 K and −1.2 K).

The M-H curves for x = 0.2 and 0.4 trace that of x = 0 in the low-field region, suggesting the persistence of a spin-singlet ground state. Persistent nature of the spin-singlet ground state up to 40%-Ta substitution is in marked contrast to the Cl-Br solid solution where the spin-singlet to CAF ground state transition was induced by 5%-Br substitution at most [11, 12]. When the magnetic field is further increased, an anomaly was found at H_c = 10.3 T, 9.1 T and 8.0 T for x = 0.0, 0.2 and 0.4, respectively,

suggestive of a field-induced phase transition. H_c decreases with x. Above H_c, the magnetization increases in proportion with H and arrives at the saturation magnetization. For $x > 0.4$, magnetization curves have finite slope even from low-field region, as in the case of $x = 1.0$.

The energy scan at $Q = 1.0$ Å^{-1} for $x = 0.3$ (Figure 2.5 (a)) shows a singlet-triplet excitation, the peak of which is centered at $\Delta_{ZF} = 2.0$ meV. This gap energy is much bigger than that expected from the high-field magnetization measurements; though magnetization measurements have not been performed for $x = 0.3$, H_c should be between 8.0 T ($x = 0.4$) and 9.1 T ($x = 0.2$) corresponding, to 0.9−1.0 meV assuming $g = 2.0$. No reason has yet been given for the source of the discrepancy of the gap energy derived from neutron and magnetization measurements, but the fact that there is a systematic decrease of Δ_{ZF} and H_c with x strongly suggests that it is an intrinsic property. The triplet mode is nearly Q-independent, indicating the localized nature of the triplet excitations as observed in $x = 0$ [6]. As shown in Figure 2.5 (b), the Q scan result at $E = 2.0$ meV for $x = 0.3$ exhibits rapidly oscillating behavior similar to $x = 0$. The fit to the isolated dimer model [6] yielded an unreasonably long intradimer distance of $R = 9.5$ Å, implying more complex and competing magnetic interactions. Powder neutron diffraction measurements for $x = 0.6$ and $x = 0.8$ (Figures 2.4 (b) and (c)) show a magnetic reflection corresponding to (1/2, 0, 1/2) indexed with respect to the chemical unit cell. Hence they should have the same spin structure as that of $x = 1.0$. It was also found that the ordered temperature hardly changes (Figures 2.4 (e) and (f)), while the ordered moment sizes decrease with decreasing x: 0.50 ± 0.1 μ_B ($x = 0.8$) and 0.27 ± 0.1 μ_B ($x = 0.6$).

Uemura and coworkers [12] recently performed μSR measurements of

$(CuCl)La(Nb_{1-x}Ta_x)_2O_7$ and proposed magnetic phase separation between the static magnetic state and spin-singlet state in the range of $0.4 < x < 1.0$. This scenario requires that the magnetization curves for $x = 0.6$ and 0.8 are expressed by two terms both in partial volume fractions: the spin-singlet phase (exemplified by the magnetization curve for $x = 0.4$) and the CAF phase ($x = 1.0$):

$$M(x) = \alpha M(1.0) + (1 - \alpha)M(0.4) \qquad (2.3)$$

In Equation 2.3, α represents the volume fraction of the CAF phase and $(1 - \alpha)$ represents that of the spin-singlet one. As shown in Figure 2.3, the fitting curves reproduce the experimental data quite well. The obtained value of α is 0.35 for $x = 0.6$ and 0.78 for $x = 0.8$ which is consistent with the μSR results (0.37 for $x = 0.6$ and 0.80 for $x = 0.8$) [12]. The decrease in intensity of the magnetic Bragg peaks can be also interpreted as a gradual decrease in the CAF partial volumes. Assuming a constant ordered moment in the CAF phase, the volume fraction α was estimated to be 0.39 ± 0.14 for $x = 0.6$ and 0.72 ± 0.15 for $x = 0.8$, again consistent with the μSR results [12] and with the magnetization results presented above.

2.4. Conclusion

It was demonstrated that a quantum phase transition from spin-singlet state to antiferromagnetic order occurs in $(CuCl)La(Nb_{1-x}Ta_x)_2O_7$, summarized in the magnetic phase diagram in Figure 2.6 (b). It is found that $(CuCl)LaTa_2O_7$ exhibits, despite the closeness of the lattice parameters in the solid solution, collinear antiferromagnetic

(CAF) order at $T_N \sim 7$ K. This clearly shows that the substitution of Ta^{5+} for Nb^{5+} in nonmagnetic slabs can affect the ground state of this quasi-2D magnet. The spin-singlet ground state in $(CuCl)LaNb_2O_7$ is fairly robust against Ta substitution ($0 \leq x \leq 0.4$), accompanied by a slight reduction of the spin gap, which is in marked contrast to the drastic collapse of the spin-singlet state in $(CuCl_{0.95}Br_{0.05})LaNb_2O_7$. In the intermediate region ($0.4 < x < 1.0$), CAF order was observed but with a nearly constant T_N, likely coexisting with the spin-singlet state with systematic variation of the volume fraction (Figure 2.6 (a)), in agreement with the recent μSR results. This is in stark contrast to the case of $(CuCl_{1-y}Br_y)LaNb_2O_7$ where T_N increases gradually from 7 K ($y = 0.05$) to 32 K ($y = 1.0$).

References

[1] R. Melzi, P. Carretta, A. Lascialfari, M. Mambrini, M. Troyer, P. Mittlet, and F. Mila: Phys. Rev. Lett. **85** (2000) 1318.

[2] H. Kabbour, E. Janod, B. Corraze, M. Danot, C. Lee, M. Whangbo, and L. Cario: J. Am. Chem. Soc. **130** (2008) 8261.

[3] K. Kodama, H. Harashina, H. Sasaki, Y. Kobayashi, M. Kasai, S. Taniguchi, Y. Yasui, M. Sato, K. Kakurai, T. Mori, and M. Nishi: J. Phys. Soc. Jpn. **66** (1997) 793.

[4] H. Kageyama, M. Nishi, N. Aso, K. Onizuka, T. Yoshihama, K. Nukui, K. Kodama, K. Kakurai, and Y. Ueda: Phys. Rev. Lett. **84** (2000) 5876.

[5] K. Onizuka, H. Kageyama, Y. Narumi, K. Kindo, Y. Ueda, and T. Goto: J. Phys. Soc. Jpn. **69** (2000) 1016.

[6] H. Kageyama, T. Kitano, N. Oba, M. Nishi, S. Nagai, K. Hirota, L. Viciu, J. B. Wiley, J. Yasuda, Y. Baba, Y. Ajiro, and K. Yoshimura: J. Phys. Soc. Jpn. **74** (2005) 1702.

[7] H. Kageyama, J. Yasuda, T. Kitano, K. Totsuka, Y. Narumi, M. Hagiwara, K. Kindo, Y. Baba, N. Oba, Y. Ajiro, and K. Yoshimura: J. Phys. Soc. Jpn. **74** (2005) 3155.

[8] A. Kitada, Z. Hiroi, Y. Tsujimoto, T. Kitano, H. Kageyama, Y. Ajiro, and K. Yoshimura: J. Phys. Soc. Jpn. **76** (2007) 093706.

[9] M. Yoshida, N. Ogata, M. Takigawa, J. Yamaura, M. Ichihara, T. Kitano, H. Kageyama, Y. Ajiro, and K. Yoshimura: J. Phys. Soc. Jpn. **76** (2007) 104703.

[10] N. Oba, H. Kageyama, T. Kitano, J. Yasuda, Y. Baba, M. Nishi, K. Hirota, Y. Narumi, M. Hagiwara, K. Kindo, T. Saito, Y. Ajiro, and K. Yoshimura: J. Phys. Soc. Jpn. **75** (2006) 113601.

[11] Y. Tsujimoto, A. Kitada, H. Kageyama, M. Nishi, Y. Narumi, K. Kindo, Y. Kiuchi, Y. Ueda, Y. J. Uemura, Y. Ajiro and K. Yoshimura: J. Phys. Soc. Jpn. **79** (2010) 014709.

[12] Y. J. Uemura, A. A. Aczel, Y. Ajiro, J. P. Carlo, T. Goko, D. A. Goldfeld, A. Kitada, G. M. Luke, G. J. MacDougall, I. G. Mihailescu, J. A. Rodriguez, P. L. Russo, A. Tanaka, Y. Tsujimoto, C. R. Wiebe, T. J. Williams, T. Yamamoto, K. Yoshimura, and H. Kageyama: Phys. Rev. B **80** (2009) 174408.

[13] R. D. Shannon: Acta. Crystallogr. A, **32** (1976) 751.

[14] T. A. Kodenkandath, J. N. Lalena, W. L. Zhou, E. E. Carpenter, C. Sangregorio, A. U. Falster, W. B. Simmons, Jr., C. J. O'Connor, and J. B. Wiley: J. Am. Chem. Soc. **121** (1999) 10743.

[15] T. A. Kodenkandath, A. S. Kumbhar, W. L. Zhou, and J. B. Wiley: Inorg. Chem. **40** (2001) 710.

[16] Y. Tsujimoto, H. Kageyama, Y. Baba, A. Kitada, T. Yamamoto, Y. Narumi, K. Kindo, M. Nishi, J. P. Carlo, A. A. Aczel, T. J. Williams, T. Goko, G. M. Luke, Y. J. Uemura, Y. Ueda, Y. Ajiro, and K. Yoshimura: Phys. Rev. B **78** (2008) 214410.

[17] V. Kataev, A. Möller, U. Löw, W. Jung, N. Schittner, M. Kriener, and A. Freimuth: J. Mag. Mag. Mater. **290-291** (2005) 310.

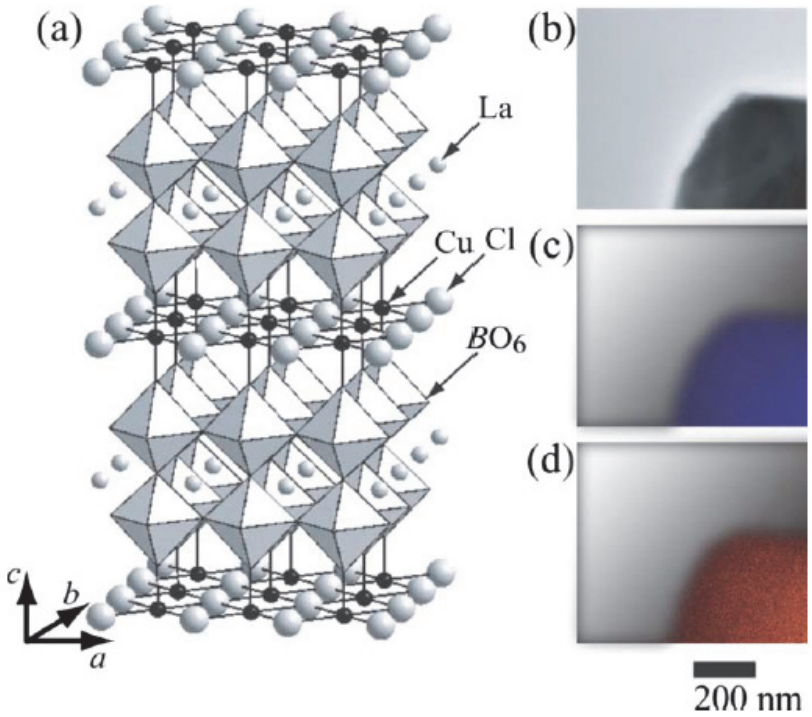

Figure 2.1. (a) Schematic view of the crystal structure of (CuCl)LaB_2O_7 (B = Nb, Ta). (b) TEM image and (c), (d) the corresponding EDS maps of the x = 0.8 sample, where blue and red dots represent Nb and Ta, respectively.

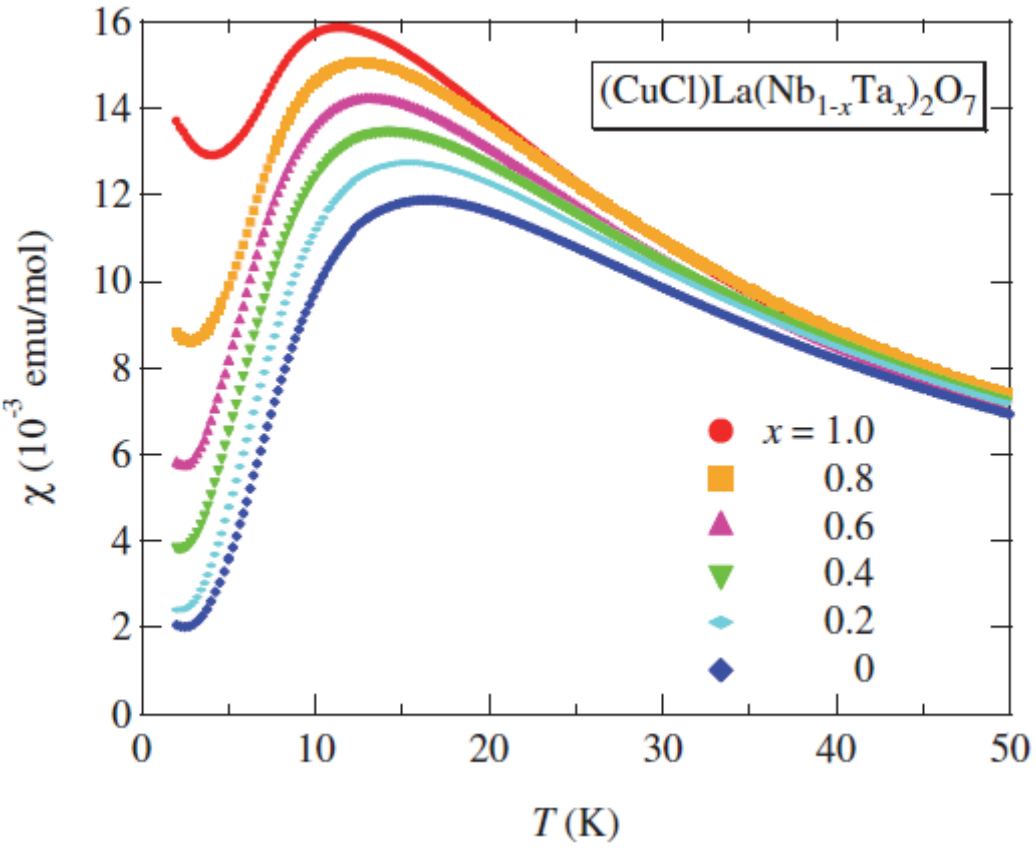

Figure 2.2. Magnetic susceptibilities of $(CuCl)La(Nb_{1-x}Ta_x)_2O_7$ measured at $H = 2$ T.

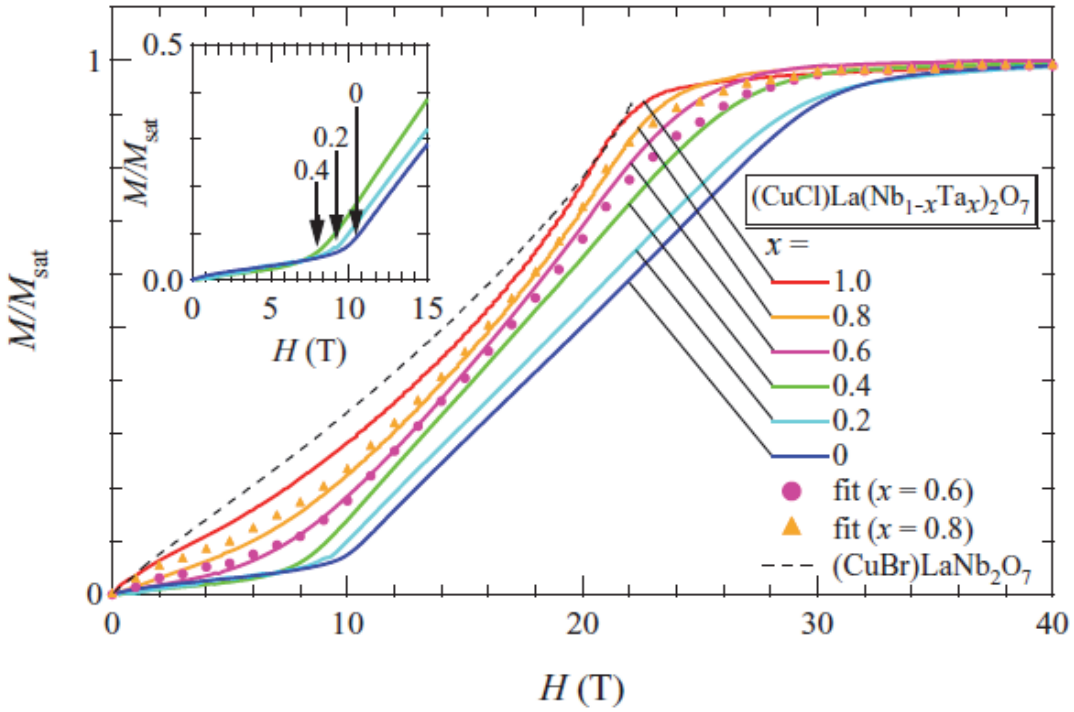

Figure 2.3. Magnetization curves M of (CuCl)La($Nb_{1-x}Ta_x$)$_2O_7$ at T = 1.3 K. The normalized magnetization for (CuBr)$LaNb_2O_7$ (broken line) was obtained from the data in ref. 10 as its saturation field equals to that of x = 1.0 (~ 23 T). Circles represent fitted curves to the x = 0.6 and 0.8 data, (see text for details). Inset is an enlarged plot for x = 0, 0.2 and 0.4, highlighting the critical fields H_c, which were assigned to the fields of the inflection points in dM/dH. The very slow increases of magnetization below H_c are due to tiny amount of defect and/or unknown magnetic impurity as mentioned in ref. 7 and ref. 9.

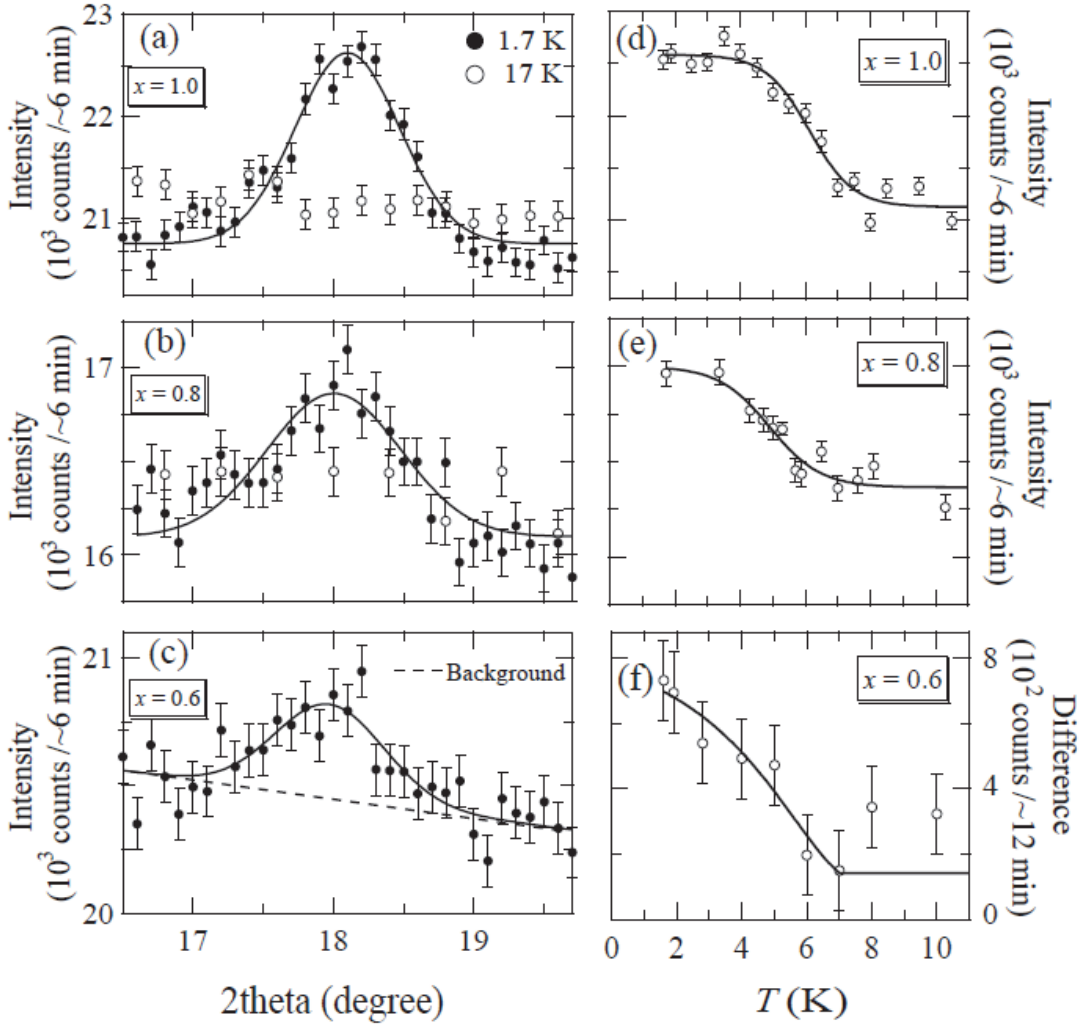

Figure 2.4. (a)−(c) Neutron diffraction profiles of x = 1.0, 0.8 and 0.6 around the (1/2, 0, 1/2) magnetic reflection. Open and closed circles represent the data collected at 1.7 K and 17 K, respectively, and solid lines are a guide to the eye. A broken line in (c) represents the background. (d)−(e) Temperature dependence of the intensity of the (1/2, 0, 1/2) reflection. The lines are a guide to the eye. (f) Temperature dependence of the difference between intensity of the (1/2, 0, 1/2) reflection and the background. The lines are a guide to the eye.

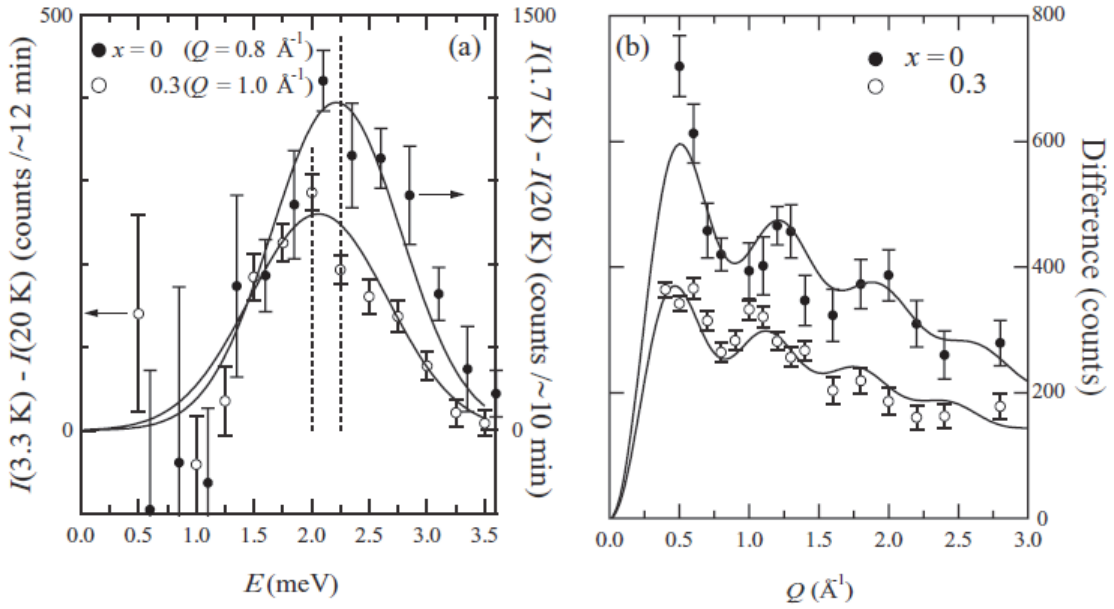

Figure 2.5. Results of inelastic neutron scattering measurements for x = 0 (closed circles) [6] and 0.3 (open circles). (a) The difference I(1.7 K) − I(20 K) for x = 0 and I(3.3 K) − I(20 K) for x = 0.3. The curve represents a least-squares fit to a Gaussian. (b) Peak intensities of the transition from the singlet ground state to the one-triplet excited state as a function of Q obtained at E = 2.1 meV for x = 0 and at E = 2.0 meV for x = 0.3. The solid lines represent the fits according to the equation written in ref. 6.

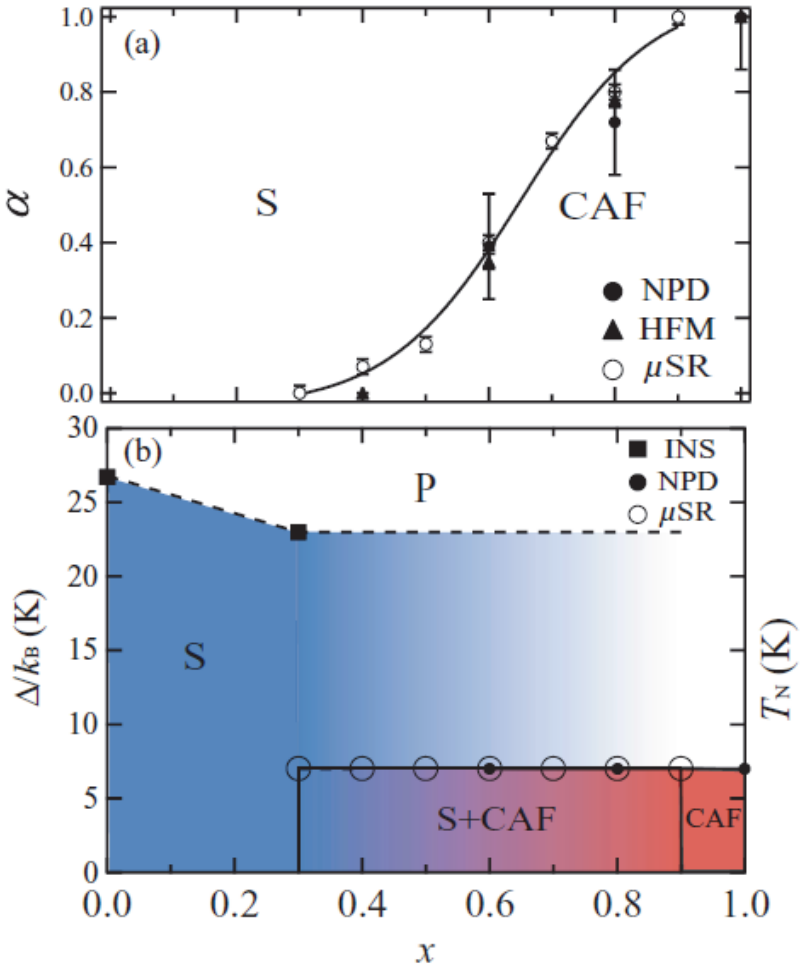

Figure 2.6. (a) Antiferromagnetic volume fraction α obtained using neutron powder diffraction (NPD) (closed circles), high-field magnetization (HFM) (closed triangles) and μSR [12] (open circles). The solid line is a guide to the eye. (b) Magnetic phase diagram of $(CuCl)La(Nb_{1-x}Ta_x)_2O_7$ as a function of temperature and concentration. Closed squares represent the zero-field gap obtained by inelastic neutron scattering (INS). S stands for the spin-singlet state. Closed and open circles denote the transition temperatures obtained by NPD and μSR [12].

Chapter 3. Quadruple-layered perovskite (CuCl)$Ca_2NaNb_4O_{13}$

3.1. Introduction

The discovery of high-T_c superconducting layered cupric oxides has led to the search for phenomena driven by quantum fluctuations in two-dimensional (2D) $S = 1/2$ antiferromagnets with square and analogous lattices. Examples include the J_1-J_2 lattice (where J_1 and J_2 denote the first-nearest-neighbor and second-nearest-neighbor exchange constants) $Li_2VO(Si, Ge)O_4$ [1], the 1/5-depleted lattice CaV_4O_9 [2], and the Shastry-Sutherland lattice $SrCu_2(BO_3)_2$ [3]. These quantum spin systems exhibit unconventional behaviors at low temperatures; e.g., spin-disordered ground state and quantized magnetization, but there still remain many open issues unsolved. For example, no material has been obtained to represent a theoretically predicted

resonating-valence-bond (RVB) state in the J_1-J_2 model [4], in which spin-singlets are quantum mechanically resonating among themselves.

(CuCl)$LaNb_2O_7$ belongs to a family with the general formula (CuX)$A_{n-1}B_nO_{3n+1}$ (X: Cl^-, Br^-; A: La^{3+}, Ca^{2+}, Sr^{2+}, …; B: Nb^{5+}, Ta^{5+}, Ti^{4+}; n = 2, 3), all prepared by topotactic ion-exchange reactions using Dion-Jacobson type layered perovskite oxides as a host. The magnetic CuX planes in (CuX)$A_{n-1}B_nO_{3n+1}$ carrying S = 1/2 are well separated spatially by nonmagnetic $A_{n-1}B_nO_{3n+1}$ perovskite slabs (~ 11 Å for n = 2 and ~ 15 Å for n = 3) [5−7]. As a result, various exotic quantum phenomena emerge depending on constituent elements; (CuCl)$LaNb_2O_7$ has a product of spin-singlet dimers as the ground state [8−12], and (CuBr)$LaNb_2O_7$ and (CuCl)$LaTa_2O_7$ order magnetically in a stripe spin structure with significantly reduced magnetic moments [13, 14]. The solid solution (CuCl)$La(Nb_{1-x}Ta_x)_2O_7$ shows a quantum phase separation at low temperatures between the spin-singlet and the antiferromagnetic states [14, 15]. (CuBr)$A_2B_3O_{10}$ has a 1/3 quantized plateau in the magnetization curve, the width of which is varied by the in-plane lattice size [16].

In (CuX)$A_{n-1}B_nO_{3n+1}$, n is the parameter that controls the two-dimensionality of the magnetic characters. It is well known that increased two-dimensionality enhances quantum fluctuations in some cases, leading to a spin-disordered (paramagnetic) state stabilized even at low temperatures relative to the exchange constant. For example, the 2D kagomé compound $Ba_2Sn_2Ga_3ZnCr_7O_{22}$, which contains a magnetically inert spacer of $Ba_2Sn_2Ga_2O_{12}$ (9.4 Å thick), has an extraordinarily large frustration factor of 200 [17]. Unfortunately, the preparation of (CuX)$A_{n-1}B_nO_{3n+1}$ has been exclusively limited to n = 2 and 3 cases. This paper will deal with the synthesis, structure and magnetism of a new n = 4 compound, (CuCl)$Ca_2NaNb_4O_{13}$, parepared by ion-exchange of $RbCa_2NaNb_4O_{13}$.

Doubling along all the crystallographic axes has been observed, which could be attributed to an octahedral tilting of the type (++0) in Glazer notation. Moreover, magnetic experiments show that the system stays in a paramagnetic state down to 2 K despite strong in-plane exchange couplings.

3.2. Experimental

3.2.1. Synthesis

The preparation of the precursor $RbCa_2NaNb_4O_{13}$, a quadruple-layered Dion-Jacobson phase as illustrated in Figure 3.1, follows that of an earlier work [18]. First, a triple-layered phase $RbCa_2Nb_3O_{10}$ was prepared from appropriate mixture of Rb_2CO_3 (Rare Metallic, 99.9%), $CaCO_3$ (Rare Metallic, 99.99%) and Nb_2O_5 (Rare Metallic, 99.99%) [19], where 50% molar excess of Rb_2CO_3 was used to compensate for loss due to its vaporization. $RbCa_2Nb_3O_{10}$ was washed with distilled water after the calcinations, and dried at 120 ºC overnight. $NaNbO_3$ was prepared from appropriate mixtures of Na_2CO_3 (Rare Metallic, 99.9%) and Nb_2O_5 (Rare Metallic, 99.99%) with 5% molar excess of Na_2CO_3. Then, equimolar $RbCa_2Nb_3O_{10}$ and $NaNbO_3$ were mixed and heated at 1150 ºC for 24 h in air to yield $RbCa_2NaNb_4O_{13}$. Finally, a low-temperature ion-exchange reaction expressed as

$$RbCa_2NaNb_4O_{13} + CuCl_2 \rightarrow (CuCl)Ca_2NaNb_4O_{13} + RbCl \qquad (3.1)$$

was performed. Here, $RbCa_2NaNb_4O_{13}$ was mixed with a two-fold molar excess of ultra dry $CuCl_2$ (Sigma-Aldrich, 99.999%), pressed into a pellet with a hand press inside an Ar-filled glovebox, and heated at 320 °C for 7 days in a sealed, evacuated ($< 4 \times 10^{-2}$ Pa) Pyrex tube. The final product was washed with distilled water to eliminate the excess copper chloride and the rubidium chloride byproduct, and dried at 120 ºC overnight.

3.2.2 Chemical Characterization

Chemical analysis was based on energy dispersive X-ray spectroscopy (EDS) measurements of sets of individual grains. These were carried out on a JEOL (JSM-5600) scanning electron microscope equipped with an EDS system installed at the Institute for Solid State Physics (ISSP), the University of Tokyo. Transmission electron microscopy (TEM) experiments were carried out at room temperature (RT) with an operating voltage of 200 kV using a JEM2010F system at ISSP. Specimens of the host and the ion-exchanged compound were finely ground in methanol and then placed on a Cu microgrid mesh for TEM observation. Synchrotron powder X-ray diffraction (XRD) experiments were carried out at ambient temperature on a large Debye-Scherrer camera installed at BL02B2 at the Japan Synchrotron Radiation Research Institute SPring-8 using an imaging plate as a detector. Incident beams from a bending magnet were monochromatized to 0.77747 Å. The final product was contained in a glass capillary tube with an inner diameter of 0.2 mm and was rotated during measurements to eliminate the effect of preferential orientation. The diffraction data were collected in a 2theta range from 1° to 75° with a step interval of 0.01°. Rietveld refinement was performed using the RIETAN-2000 program [20]. The agreement indices used were the weighted profile $R_{wp} = [\Sigma w_i(y_{io} - y_{ic})^2/\Sigma w_i(y_{io})^2]^{1/2}$ and the goodness of fit (GOF), $\chi^2 = (R_{wp}/R_{Bragg})^2$, where $R_{Bragg} = [(N - P)/\Sigma w_i y_{io}{}^2]^{1/2}$, y_{io} and y_{ic} are the observed and calculated intensities, w_i is the weighting factor, N the total number of y_{io} data when the background is refined, and P the number of adjusted parameters.

3.2.3. Magnetism

Magnetic susceptibility measurements of $(CuCl)Ca_2NaNb_4O_{13}$ were performed on a powder sample with a Quantum Design MPMS (Magnetic Property Measurement System) over a temperature range $T = 2-350$ K in a magnetic field H of 1 T. High-field magnetization measurements up to 57 T were conducted using an induction method with a multilayer pulse magnet installed at ISSP. Specific heat measurements were performed by the heat relaxation method down to 2 K in a zero magnetic field using a Quantum Design PPSM (Physical Property Measurement System) at ISSP. Zero-filed and longitudinal-field muon spin relaxation (μSR) measurements were performed at the M20 channel at TRIUMF, the Canadian National Accelerator Laboratory in Vancouver. Polarized positive muons were implanted one-by-one into the specimen mounted in a

gas-flow He cryostat down to T = 2.0 K. Details of the μSR methods can be found elsewhere [21].

3.3. Results and Discussion

3.3.1. Structure

Laboratory XRD patterns of both $RbCa_2NaNb_4O_{13}$ and $(CuCl)Ca_2NaNb_4O_{13}$ at RT, shown in Figure 3.2, could be readily indexed into tetragonal systems with cell parameters a = 3.869 Å and c = 18.859 Å for the former and a = 3.866 Å and c = 19.608 Å for the latter compound. No impurity phase could be detected within the experimental resolution limits. The obtained lattice parameters for the precursor are in a good accordance with the reported values (a = 3.8727 Å, c = 18.9116 Å) [18]. The elongation along the c axis (see the inset of Figure 3.2), ca. 0.7 Å relative to the precursor, is consistent with the results on the n = 2 and 3 compounds [5−7] and thus is evidence for the insertion of a CuCl layer. The EDS experiment reveals the composition of the final product to be approximately Cu : Cl : Ca : Na : Nb = 1 : 1 : 2 : 1 : 4. The absence of Rb also supports the occurrence of desired ion-exchange reaction (Equation 3.1).

The use of electron diffraction is crucial for identifying possible superstructures. The room-temperature electron diffraction (ED) patterns for $(CuCl)Ca_2NaNb_4O_{13}$ along the [001]* and [010]* zone axes are shown in Figures 3.3 (a) and (b), which reveal weak commensurate reflections such as (1/2 1/2 0) and (1/2 0 1/2), together with strong fundamental ones. The extinct reflections are described as $\{hkl;\ h + k + l = \text{odd}\}$, $\{hk0;\ h + k = \text{odd}\}$, $\{h00;\ h = \text{odd}\}$, $\{h0l;\ h + l = \text{odd}\}$ and $\{00l;\ l = \text{odd}\}$ in the $2a_p \times 2a_p \times 2c_p$ cell indexation, where a_p and c_p denote the original primitive unit cell parameters of $RbCa_2NaNb_4O_{13}$. Furthermore, the room-temperature synchrotron XRD profile (see the inset of Figure 3.4) not only confirmed the tetragonal symmetry, but also detected superlattice reflections being consistent with the extinction conditions obtained from the TEM study. Therefore, possible space groups are $I4$ (No. 79), $I\bar{4}$ (No. 82), $I4/m$ (No. 87), $I422$ (No. 97), $I4mm$ (No. 107), $I\bar{4}m2$ (No. 119), $I\bar{4}2m$ (No. 121) and $I4/mmm$ (No. 139).

A large number of perovskite-based compounds have structural deviations from their ideal structure, which is governed by the tolerance factor t. When t is smaller than

unity, coherent octahedral tilting takes place, resulting in reduction of symmetry accompanied by the emergence of a superstructure [22]. Assuming a random distribution of Ca^{2+} and Na^{+} for $(CuCl)Ca_2NaNb_4O_{13}$, one can use, in a first approximation, the average value $t = 0.955$ ($r(Ca^{2+}) = 1.34$ Å, $r(Na^{+}) = 1.39$ Å [23]). It is therefore natural to consider that octahedral tilting is present in this material and causes the doubling of all the crystallographic axes.

It is then presumed that $RbCa_2NaNb_4O_{13}$ with the identical t value exhibits the same type of octahedral tilting, which, however, was not been reported. Synchrotron XRD and TEM measurements were conducted for this compound. While the XRD experiments did not detect any superreflection peaks (not shown), the ED displayed very weak and diffuse superlattice reflections (Figure 3.5 (a)). These reflections were observed only in a small region of the particle, and in other regions no obvious superlattice reflections were observed (Figure 3.5 (b)). This observation is in contrast to $(CuCl)Ca_2NaNb_4O_{13}$, the ED of which has well-defined superreflections (without any streaks) observed uniformly across the specimen (Figures 3.3 (a) and (b)). This means that the inserted copper-halide arrays in between the perovskite layers play a crucial role in stabilizing the superstructure associated with the octahedral tilting.

The difference in structure between $RbCa_2NaNb_4O_{13}$ and $(CuCl)Ca_2NaNb_4O_{13}$ would be related to the difference in the bonding nature connecting adjacent perovskite blocks. In $RbCa_2NaNb_4O_{13}$, the adjacent $Ca_2NaNb_4O_{13}$ blocks are weakly bound via the Rb cations. The weak bonding nature of this and related Dion-Jacobson layered perovskites is indeed what provides the abilities of ion-exchange and makes them amenable to exofoliation into nanosheets [24]. However, this feature in turn results in the octahedral tilting being extended to only a short distance. In $(CuCl)Ca_2NaNb_4O_{13}$, the adjacent perovskite slabs are connected covalently via the edge-shared CuO_4Cl_2 octahedra, which results in a long ranged coherent octahedral tilting. The details of the possible octahedral tilting arrangements will be discussed later.

3.3.2. Magnetism

Figure 3.6 (a) shows the temperature dependence of magnetic susceptibility χ for $(CuCl)Ca_2NaNb_4O_{13}$. At the first sight, it does not show any spectacular behavior. With decreasing temperature down to 2 K, the susceptibility gradually increases. Using the

Curie-Weiss equation,

$$\chi = C/(T - \theta) \qquad (3.2)$$

a Curie constant C = 0.386 emu K/mol was obtained by fitting the data above 150 K, which agrees well with that expected for 1 mol of Cu^{2+} ions (0.375 emu K/mol when assuming the isotropic g-factor of 2.0). It also confirms a successful ion-exchange reaction. Below 150 K, the experimental susceptibility deviates from the Curie-Weiss behavior. The Weiss temperature is θ = 22.4 K (Figure 3.6 (b)). The positive Weiss temperature is suggestive of ferromagnetic intra-layer interactions. The out-of-plane interaction is expected to be negligibly small because the magnetic layer is widely separated by the nonmagnetic layer (~ 20 Å). This implies that the magnetization would saturate easily by applying a weak magnetic field. Contradictory to this prediction, however, the magnetization curves of $(CuCl)Ca_2NaNb_4O_{13}$ at 1.3 K and 4.2 K evolve rather slowly and do not saturate even at 57 T (Figure 3.7). This indicates the presence of a strong antiferromagnetic exchange coupling at low temperatures, and the apparent small (and ferromagnetic) Weiss temperature is as a consequence of close competition between ferromagnetic and antiferromagnetic interactions within the CuCl layer. The coexistence of such competing interactions in the CuBr and CuCl layers have been discussed in the n = 2 and n = 3 systems [8, 12−15], so it is not surprising that this situation is present in the present n = 4 case.

The presence of competing interactions in the CuCl layer is inferred also from the temperature dependence of total specific heat. As shown in Figure 3.8, C_p/T exhibits a Schottky-like round maximum at around 3 K. This anomaly might be due to an energy gap of some type, although $(CuCl)Ca_2NaNb_4O_{13}$ does not have any spin-disordered ground state with a finite gap (see Figures 3.6 (a) and 3.7). Interestingly, similar behavior is reported for a 2D kagomé compound $[Cu_3(titmb)_2(OCOCH_3)_6]\cdot H_2O$ (titmb = 1,3,5-tris(imidazol-1-ylmethyl)-2,4,6 trimethylbenzene) with competing interactions also within the layer [25]. Competing interactions create a very large density of low-lying excited states, where even a small perturbation may change its ground state, giving non-spin-gapped aspects in susceptibility and/or magnetization data.

μSR measurements offer a unique opportunity in detecting static magnetic order with high sensitivity. Figure 3.9 shows the zero-field spectra for $(CuCl)Ca_2NaNb_4O_{13}$ measured at 5 K and 2 K. The time evolution $A(t)$ of the muon spin polarization was obtained from the time histograms $F(t)$ and $B(t)$ of the forward and backward counters as

$$A(t) = A_0G(t) = [F(t) - B(t)]/[F(t) + B(t)] \quad (3.3)$$

where A_0 is a constant and $G(t)$ represents the relaxation function defined with $G(0) = 1$ [21]. The relaxation spectra at 5 K and 2 K are almost identical and can be decoupled by the longitudinal magnetic field of 100 G. These results unambiguously demonstrate that long-range magnetic order is absent down to 2 K, despite strong in-plane interactions. The absence of magnetic order down to 2 K is attributed to the competing interactions within the layer as well as the enhanced two-dimensionality. Further study is required to understand the nature of the ground state in $(CuCl)Ca_2NaNb_4O_{13}$.

3.3.3 Structural refinement

As the author mentioned above, eight possible tetragonal space groups for $(CuCl)Ca_2NaNb_4O_{13}$ are derived from the XRD and ED patterns. However, solving the structure solely by Rietveld analysis without any further constraints would be very difficult, given that the $2a_p \times 2a_p \times 2c_p$ unit cell contains as 176 atoms ($Z = 8$). For this reason, Aleksandrov's analysis was utilized, where symmetry reduction in response to octahedral tilting in layered perovskites were theoretically studied [26]. The material finds the following characteristics: an even number of perovskite layers (i.e., $n = 4$), $P4/mmm$ in the absence of octahedral tilting, and a $2a_p \times 2a_p \times 2c_p$ cell. These conditions reduce the possible space groups to $P4_2/mmc$ (No. 131) with a (+++) tilt, $P4_2/nmc$ (No. 137) with a (++−) tilt and $I4/mmm$ (No. 139) with a (++0) tilt, where +, – and 0 denote, respectively, in-phase tilt, out-of-phase tilt and no tilt in Glazer's notation [27]. Among them, only $I4/mmm$ meets the extinction conditions derived from the TEM

and XRD results.

Therefore, Rietveld refinement of the synchrotron XRD data for $(CuCl)Ca_2NaNb_4O_{13}$ was performed using *I*4/*mmm* as the space group. Initial atomic coordinates of calcium, sodium, niobium and oxygen were set based on crystallographic data of $RbCa_2NaNb_4O_{13}$ (*P*4/*mmm*, $a_p \times a_p \times c_p$) reported by Sugimoto and coworkers [18]. Calcium and sodium ions were assumed to be randomly distributed at the *A*-sites. The thermal parameters of Cl, *A*(Ca, Na), Nb and O atoms were set to be equal respectively, a constraint being sometimes applied when complex structures are refined, as in $RbCa_2NaNb_4O_{13}$ [18]. Linear constraints were logically set up so as to maintain the (++0) tilt system: $x(O(i)) = x(O(j))$ for $i, j = 1-3$ and $y = 0.25$ for O(4)−O(7). The initial positions of copper atom and chlorine atoms were set at the ideal (most symmetric) positions: 8*f* (1/4, 1/4, 1/4) for Cu, and 4*e* (0, 0, *z*) and 4*d* (0, 1/2, 1/4) for Cl(1) and Cl(2). The refinement converged quickly to acceptable agreement factors (R_{wp} = 5.90%, R_{Bragg} = 3.25% and χ^2 = 3.31). However, obtained thermal parameters for chlorine atoms were too large, $B_{iso}(Cl) = 8.2(3)$ Å^2, a result similar to previous structural studies on the homologous $(CuCl)A_{n-1}B_nO_{3n+1}$ [5, 6].

The model was subsequently modified by introducing disorder of chlorine atoms. Several models involving disorder of the chlorine sites were examined and the model in which Cl(1) and Cl(2) atoms moved to, respectively, 16*m* (*x*, *x*, *z*) and 16*k* (*x*, *x* + 1/2, 1/4), with 25% site occupancy, resulted in the best fit: $x = 0.035(9)$ for Cl(1) and 0.049(9) for Cl(2), $B_{iso}(Cl) = 2.8(5)$ Å^2), R_{wp} = 5.72%, R_{Bragg} = 3.25% and χ^2 = 3.10. It would be worth noting that the *z*-coordinate of the Cl(1) atom was very close to 0.25 ($z = 0.252(1)$), indicating that the Cl(1) atom hardly moved off the Cu-plane. The obtained thermal parameters for each site were acceptable considering previous data on perovskite niobates [18, 28, 29]. The observed, calculated, and difference plots for the final refinement are shown in Figure 3.4, and the crystallographic data are presented in Table 3.1. The structure is illustrated in Figures 3.1 (b)−(e). Note that, when the thermal parameters of Cl, *A*(Ca, Na), Nb and O atoms were individually refined, the variable atomic coordinates became less stable. Given many adjustable parameters, it is hard, with the current synchrotron data alone, to perform a refinement without the constraints on the thermal parameters. In order to validate the structure proposed in this study, high-resolution neutron diffraction study, which can determine oxygen positions with

higher accuracy, along the combined X-ray/neutron refinement would be necessary.

The bond distances are listed in Table 3.2. It is seen that the Nb(2)-O(3) distance of 1.71(1) Å (O(3) is the outer oxygen site) is relatively short. However, it would like to be noted that in layered perovskite niobates, the Nb-O bond extending to the interlayer has a tendency to form a shorter bond. For example, similar values of 1.77(6) Å and 1.748(6) were reported, respectively, for $RbCa_2NaNb_4O_{13}$ [18] and Å in $KCa_2Nb_3O_{10}$ [30]. The bond valence sum (BVS) method was applied to estimate the valences of cations using tabulated parameters [31], and +1.7, +5.5 and +1.4 was obtained for Cu, Nb and *A* (= $Ca_{2/3}Na_{1/3}$) respectively, in reasonable agreement with the formal values.

The Cl(1) atom, which the O(3) atom moves toward from the ideal site, has a smaller degree of displacement from its ideal position than the Cl(2) atom (see Figure 3.1 (e)), probably to reduce Coulomb repulsion from the apical oxygen. By contrast, the Cu atom, which has its neighboring two apical oxygen atoms O(3) moving away along <110>, remains at the midpoint of these two oxygen atoms i.e. the ideal site. It should be noted that at low temperatures, ordering of the chlorine atoms might occur. Such structural relationships between $CuCl_4O_2$ and NbO_6 octahedra are also reported in the *n* = 2 analogue $(CuCl)LaNb_2O_7$ [12]. In $(CuCl)LaNb_2O_7$, the Cl ions as well as their nearest oxygen atoms shift mostly along the b_p axis, probably due to their electrostatic repulsion. Moreover, in marked contrast to the *n* = 4 case, the Cu atoms are displaced from their ideal positions, while the apical oxygen atoms still move toward the same direction.

It is now interesting to compare the present compound with the *A*-site deficient perovskite $Na_{0.74}WO_3$, which is the only reported compound with the same (++0) tilt [32]. It was found that the tilt angle φ along the *a*-axis was 4.0º, estimated from

$$\tan\varphi = \{a\cdot(x(\mathrm{O}(i)) - x(\mathrm{O}(j)))\}/\{c\cdot(z(\mathrm{O}(i)) - z(\mathrm{O}(j)))\} \qquad (3.4)$$

where (*i*, *j*) = (1, 2) and (2, 3)). This value is close to 3.40º in $Na_{0.74}WO_3$ [32]. Note that this value is much smaller than that in $RbAgF_3$ with a (− − +) tilt (8.0º) [33] and $SrZrO_3$ with a (00−) tilt (8.95º) [34], despite having similar *t* values. As pointed out in ref [22], the *A*-site (Na) in $Na_{0.74}WO_3$ has three kinds of coordination geometry; i.e. square-planar, rectangular-planar and square-prismatic coordination. Likewise, for

$(CuCl)Ca_2NaNb_4O_{13}$ the *A*(1)-, *A*(2)- and *A*(3)-sites comprising the inner perovskite slabs being surrounded only by $Nb(1)O_6$ octahedra, have, respectively, square-planar, rectangular-planar and square-prismatic coordination (Figures 3.10 (a)−(c)). Note, however, that the *A*(4)−*A*(6) sites comprising the outer perovskite slabs being surrounded both by $Nb(1)O_6$ and $Nb(2)O_6$ octahedra have a more distorted coordination geometry as shown in Figures 3.10 (d)–(f).

3.4. Conclusion

Synthesis of a quadruple-layered copper oxyhalide $(CuCl)Ca_2NaNb_4O_{13}$ is reported. Through topotactic ion-exchange with $CuCl_2$, the precursor $RbCa_2NaNb_4O_{13}$ with diffuse superreflections changes into $(CuCl)Ca_2NaNb_4O_{13}$ with a well-defined, tetragonal $2a_p \times 2a_p \times 2c_p$ superstructure. The insertion of the edge-shared $CuCl_4O_2$ layer induces strong bonding between the neighboring perovskite slabs, likely stabilizing the superstructure. Magnetic studies reveal that $(CuCl)Ca_2NaNb_4O_{13}$ does not undergo magnetic long-range ordering down to 2 K despite strong magnetic interaction in the CuCl plane, due to the enhanced quantum fluctuations in two dimensions. Group theory analysis together with the synchrotron XRD and TEM measurements suggests the *I*4/*mmm* space group with an unusual in-phase two-tilt system (++0) in $(CuCl)Ca_2NaNb_4O_{13}$. Applying the ion-exchange reaction to other layered perovskites $A'A_{n-1}B_nO_{3n+1}$ with $n > 4$ may allow us to obtain more 2D materials with further enhanced quantum fluctuations.

References

[1] R. Melzi, P. Carretta, A. Lascialfari, M. Mambrini, M. Troyer, P. Mittlet, and F. Mila: Phys. Rev. Lett. **85** (2000) 1318.

[2] K. Kodama, H. Harashina, H. Sasaki, Y. Kobayashi, M. Kasai, S. Taniguchi, Y. Yasui, M. Sato, K. Kakurai, T. Mori, and M. Nishi: J. Phys. Soc. Jpn. **66** (1997) 793.

[3] H. Kageyama, M. Nishi, N. Aso, K. Onizuka, T. Yoshihama, K. Nukui, K. Kodama, K. Kakurai, and Y. Ueda: Phys. Rev. Lett. **84** (2000) 5876.

[4] P. W. Anderson: Mater. Res. Bull. **8** (1973) 153.

[5] T. A. Kodenkandath, J. Lalena, W. L. Zhou, E. E. Carpenter, C. Sangregorio, A. U. Falster, W. B. Simmons, Jr., C. J. O'Connor, and J. B. Wiley: J. Am. Chem. Soc. **121** (1999) 10743.

[6] T. A. Kodenkandath, A. S. Kumbhar, W. L. Zhou, and J. B. Wiley: Inorg. Chem. **40** (2001) 710.

[7] H. Kageyama, L. Viciu, G. Caruntsu, Y. Ueda, and J. B. Wiley: J. Phys. Condens. Matter **16** (2004) S585.

[8] H. Kageyama, T. Kitano, N. Oba, M. Nishi, S. Nagai, K. Hirota, L. Viciu, J. B. Wiley, J. Yasuda, Y. Baba, Y. Ajiro, and K. Yoshimura: J. Phys. Soc. Jpn **74** (2005) 1702.

[9] H. Kageyama, J. Yasuda, T. Kitano, K. Totsuka, Y. Narumi, M. Hagiwara, K. Kindo, Y. Baba, N. Oba, Y. Ajiro, and K. Yoshimura: J. Phys. Soc. Jpn. **74** (2005) 3155.

[10] A. Kitada, Z. Hiroi, Y. Tsujimoto, T. Kitano, H. Kageyama, Y. Ajiro, and K. Yoshimura: J. Phys. Soc. Jpn. **76** (2007) 093706.

[11] M. Yoshida, N. Ogata, M. Takigawa, J. Yamaura, M. Ichihara, T. Kitano, H. Kageyama, Y. Ajiro, K. Yoshimura, J. Phys. Soc. Jpn. **76** (2007) 104703.

[12] C. Tassel, J. Kang, C. Lee, O. Hernandez, Y. Qiu, W. Paulus, E. Collet, B. Lake, T. Guidi, M.-H. Whangbo, C. Ritter, H. Kageyama, and S.-H. Lee: Phys. Rev. Lett. **105** (2010) 167205.

[13] N. Oba, H. Kageyama, T. Kitano, J. Yasuda, Y. Baba, M. Nishi, K. Hirota, Y. Narumi, M. Hagiwara, K. Kindo, T. Saito, Y. Ajiro, and K. Yoshimura: J. Phys. Soc. Jpn. **75** (2006) 113601.

[14] A. Kitada, Y. Tsujimoto, H. Kageyama, Y. Ajiro, M. Nishi, Y. Narumi, K. Kindo, M. Ichihara, Y. Ueda, Y. J. Uemura, and K. Yoshimura: Phys. Rev. B, **80** (2009) 174409.

[15] Y. J. Uemura, A. A. Aczel, Y. Ajiro, J. P. Carlo, T. Goko, D. A. Goldfeld, A. Kitada, G. M. Luke, G. J. MacDougall, I. G. Mihailescu, J. A. Rodriguez, P. L. Russo, Y. Tsujimoto, C. R. Wiebe, T. J. Williams, T. Yamamoto, K. Yoshimura, and H. Kageyama: Phys. Rev. B **80**, (2009) 174408.

[16] Y. Tsujimoto, H. Kageyama, Y. Baba, A. Kitada, T. Yamamoto, Y. Narumi, K. Kindo, M. Nishi, J. P. Carlo, A. A. Aczel, T. J. Williams, T. Goko, G. M. Luke, Y. J. Uemura, Y. Ueda, Y. Ajiro, and K. Yoshimura: Phys. Rev. B **78** (2008) 214410.

[17] I. S. Hagemann, Q. Huang, X. P. A. Gao, A. P. Ramirez, and R. J. Cava: Phys. Rev. Lett. **86** (2001) 894.

[18] W. Sugimoto, H. Ohkawa, M. Naito, Y. Sugahara, and K. Kuroda: J. Solid State Chem. **148** (1999) 508.

[19] M. Dion, M. Ganne, and M. Tournoux: Mater. Res. Bull. **16** (1981) 1429.

[20] F. Izumi and T. Ikeda: Mater. Sci. Forum. **321-324** (2000) 198.

[21] R. S. Hayano, Y. J. Uemura, J. Imazato, N. Nishida, T. Yamazaki, and R. Kubo: Phys. Rev. B **20** (1979) 850.

[22] P. M. Woodward: Acta Crystallogr. B **53** (1997) 44.

[23] R. D. Shannon: Acta Crystallogr. A **32** (1976) 751.

[24] R. E. Shaak and T. E. Mallouk: Chem. Mater. **14** (2002) 1455.

[25] Y. Narumi, K. Katsumata, Z. Honda, J.-C. Domenge, P. Sindzingre, C. Lhuillier, Y. Shimaoka, T. C. Kobayashi, and K. Kindo: Europhys. Lett. **65** (2004) 705.

[26] K. S. Aleksandrov: Crystallography Reports **40** (1995) 251.

[27] A. M. Glazer: Acta Crystallogr. B **28** (1972) 3384.

[28] M. Yashima, S. Matsuyama, R. Sano, M. Itoh, K. Tsuda, and D. Fu: Chem. Mater. **23** (2011) 1643.

[29] J. A. Schottenfeld, A. J. Benesi, P. W. Stephens, G. Chen, P. C. Eklund, and T. E. Mallouk: J. Solid State Chem. **178** (2005) 2313.

[30] H. Fukuoka, T. Isami, and S. Yamanaka: J. Solid State Chem. **151** (2000) 40.

[31] I. D. Brown and D. Altermatt: Acta Crystallogr. B **41** (1985) 244.

[32] C. N. W. Darlington, J. A. Hriljac, and K. S. Knight: Acta Crystallogr. B **59** (2003)

584.

[33] R. H. Odenthal and R. Hoppe: Monatsh Chem. **102** (1971) 1340.

[34] A. Ahtee, M. Ahtee, A. M. Glazer, and A. W. Hewat: Acta Crystallogr. B **32** (1976) 3243.

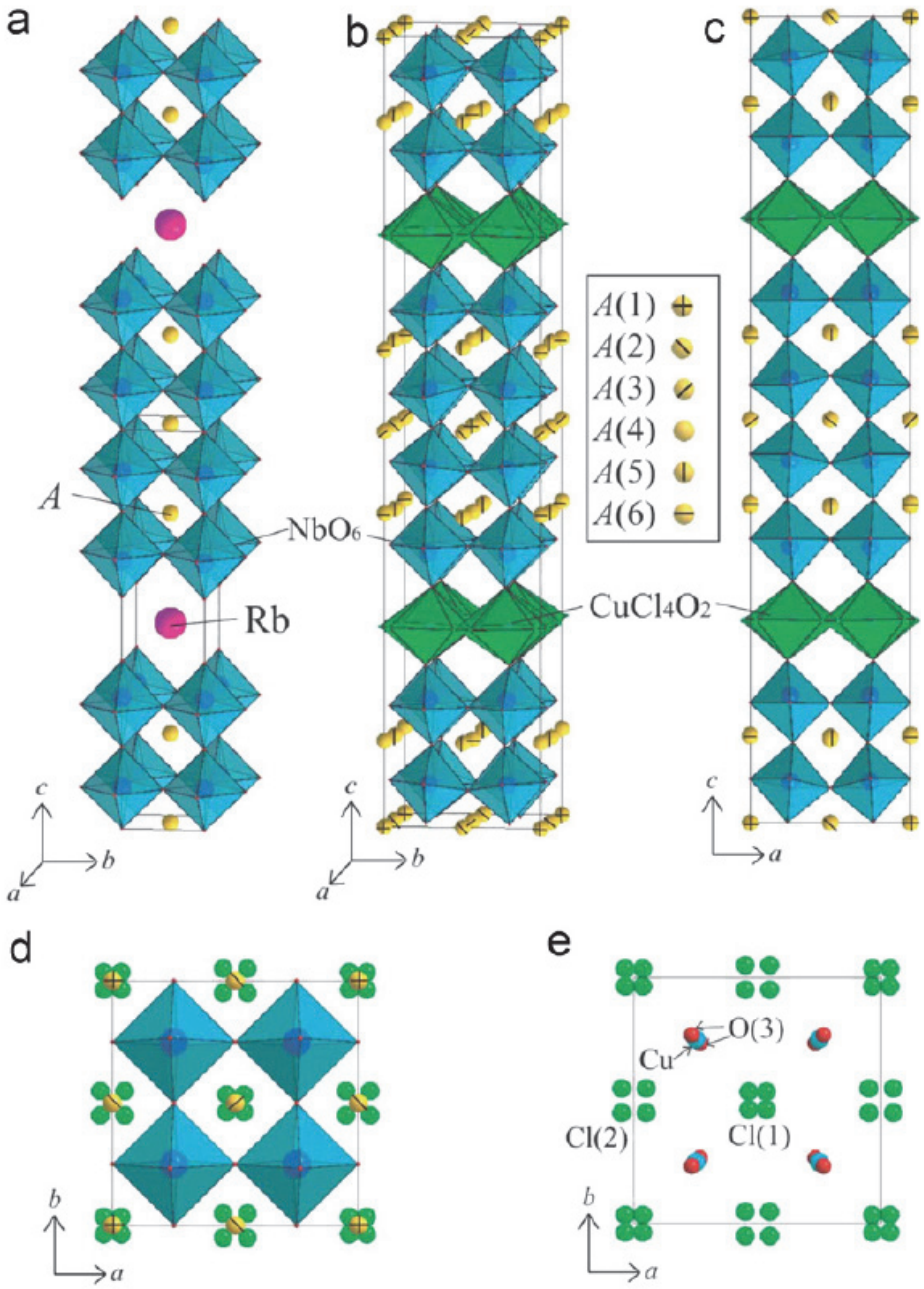

Figure 3.1. (a) Clinographic presentation of the structure of $RbCa_2NaNb_3O_{10}$ reported by Sugimoto *et al*. [18] and (b) the room-temperature structure of $(CuCl)Ca_2NaNb_4O_{13}$ obtained in this study. (c) [010] projection, (d) [001] projection, (e) the edge-shared $CuCl_4O_2$ layer viewed along [001].

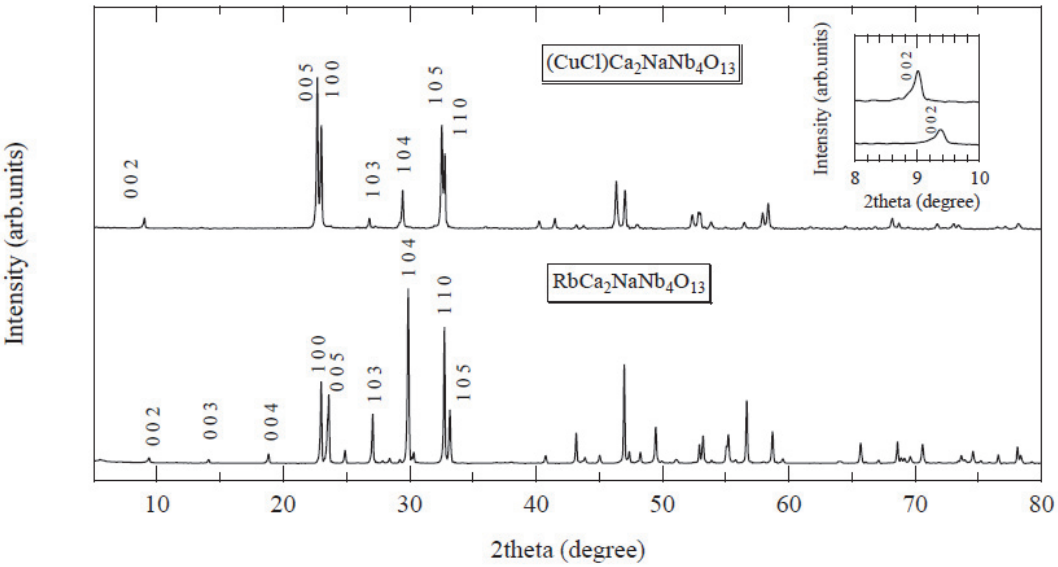

Figure 3.2. Laboratory powder X-ray diffraction profile of $RbCa_2NaNb_4O_{13}$ and $(CuCl)Ca_2NaNb_4O_{13}$ measured at room temperature (RT). The inset shows 002 peak of each compound.

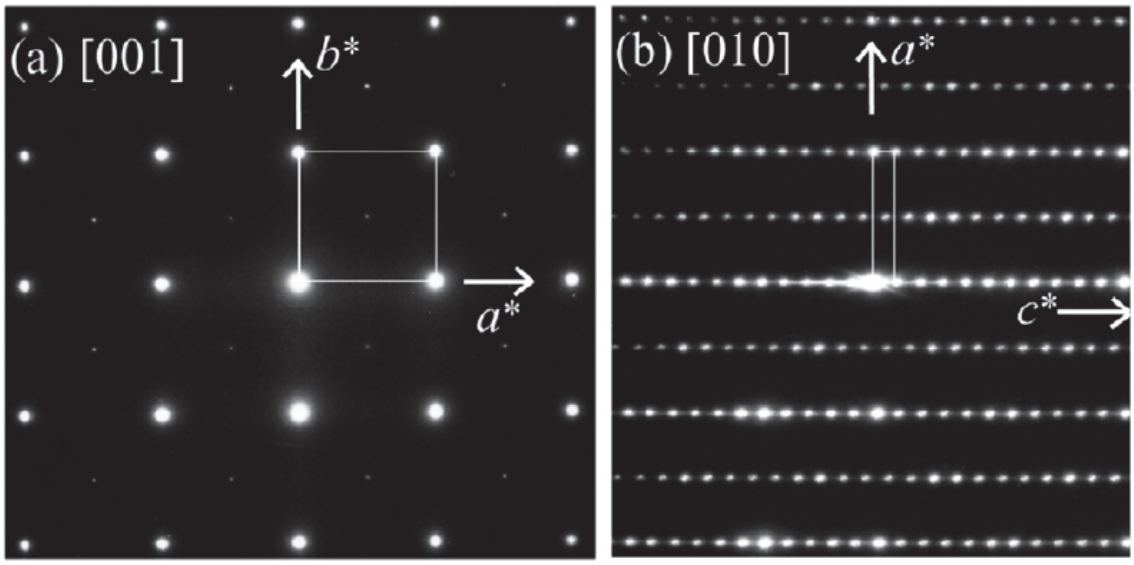

Figure 3.3. Electron diffraction patterns of $(CuCl)Ca_2NaNb_4O_{13}$ at RT obtained along (a) the [001]- and (b) the [010]-zone axes.

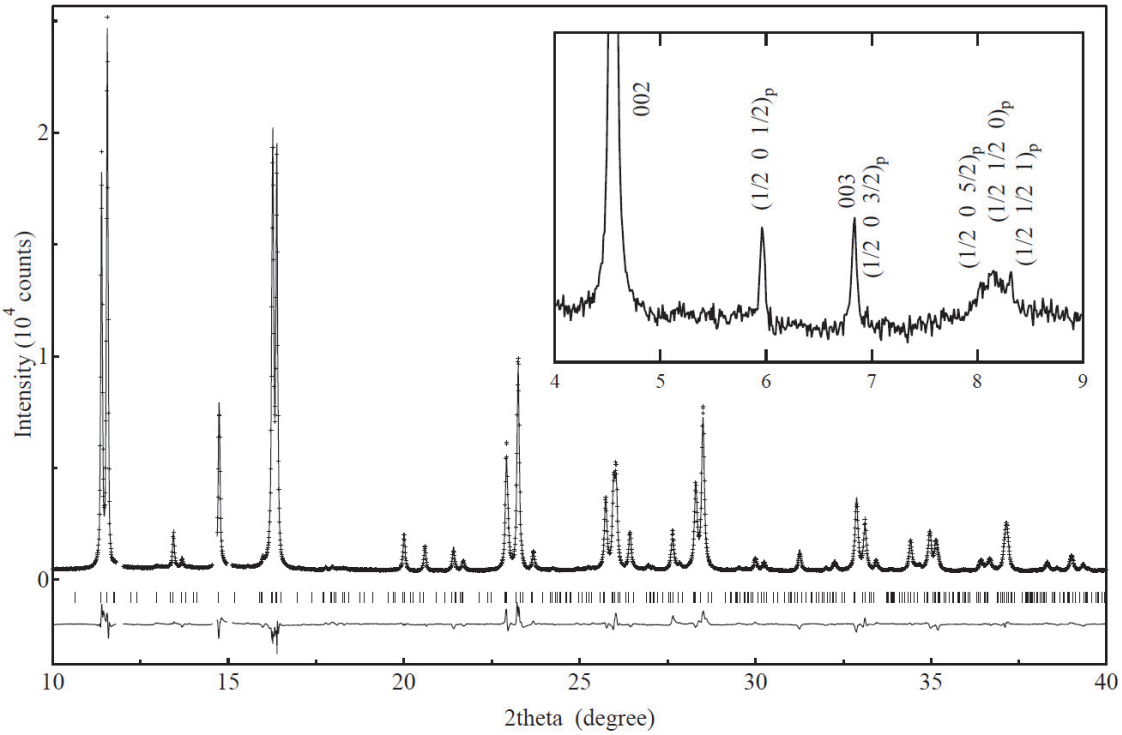

Figure 3.4. Powder synchrotron X-ray diffraction profile of $(CuCl)Ca_2NaNb_4O_{13}$ obtained at RT. The wavelength was λ = 0.77747 Å. Observed and calculated diffraction patterns are represented by crosses and solid curve, respectively. Vertical bars are related to the calculated Bragg reflection positions and solid lines below are the difference between observed and calculated data. The inset shows several superreflections to evidence the $2a_p \times 2a_p \times 2c_p$ supercell.

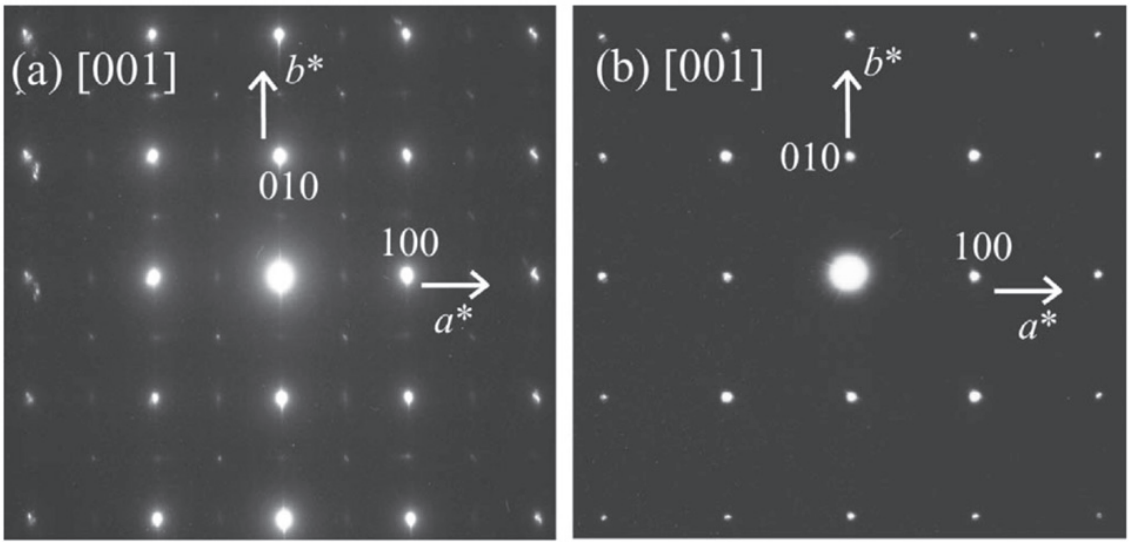

Figure 3.5. (a), (b) Room-temperature electron diffraction patterns along the [001]-zone axis of $RbCa_2NaNb_4O_{13}$ obtained from different areas.

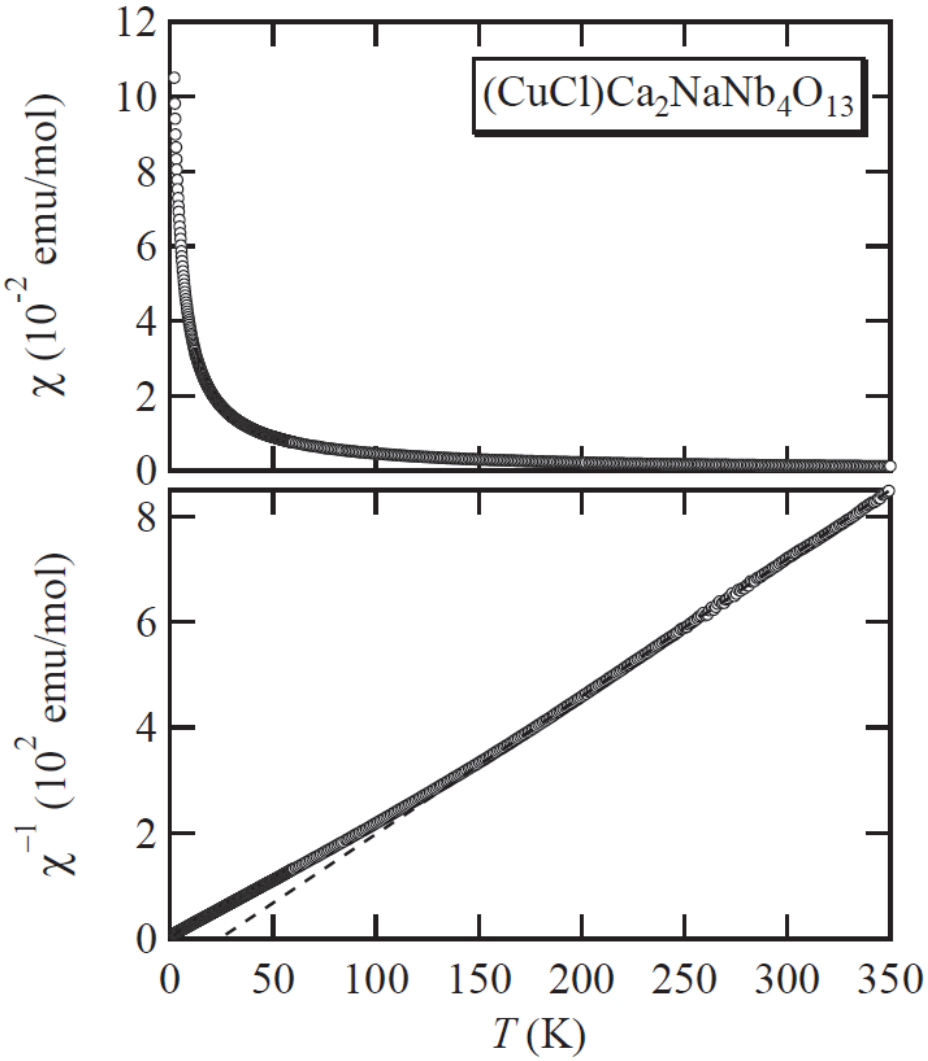

Figure 3.6. (a) Susceptibility and (b) inverse susceptibility for $(CuCl)Ca_2NaNb_4O_{13}$ measured at 1 T. The dotted line represents the Curie-Weiss fit.

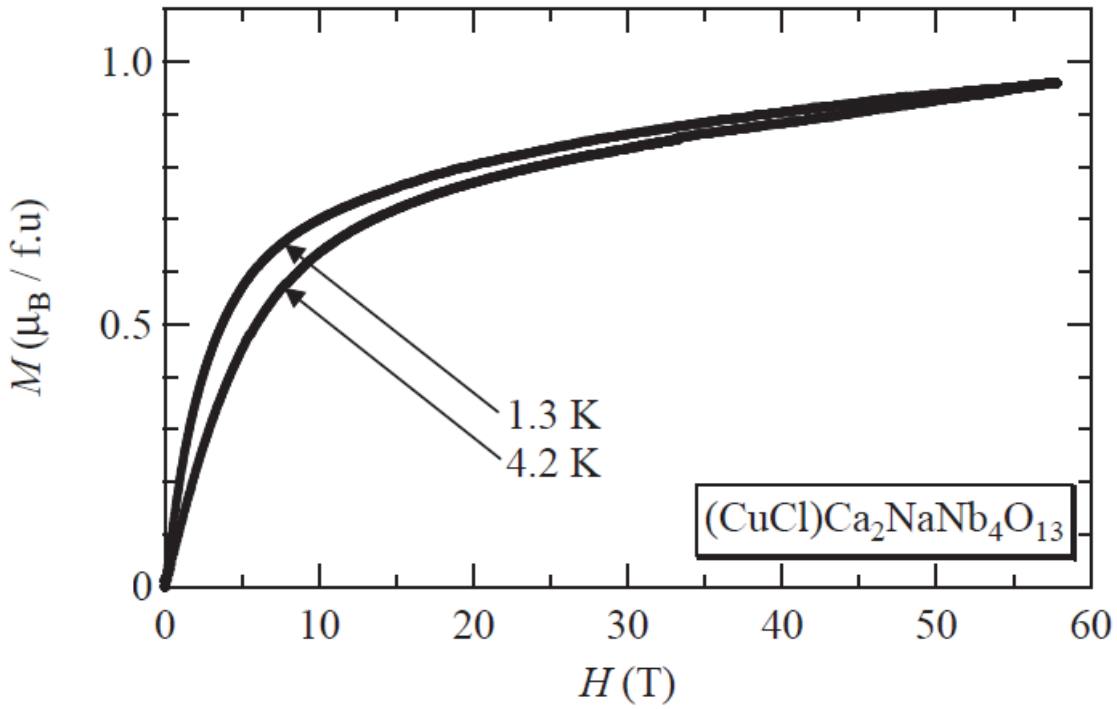

Figure 3.7. Magnetizations for $(CuCl)Ca_2NaNb_4O_{13}$ at 1.3K and 4.2K measured in pulsed fields. Within the experimental certainty, no hysteresis was observed between runs where the field was increased/decreased.

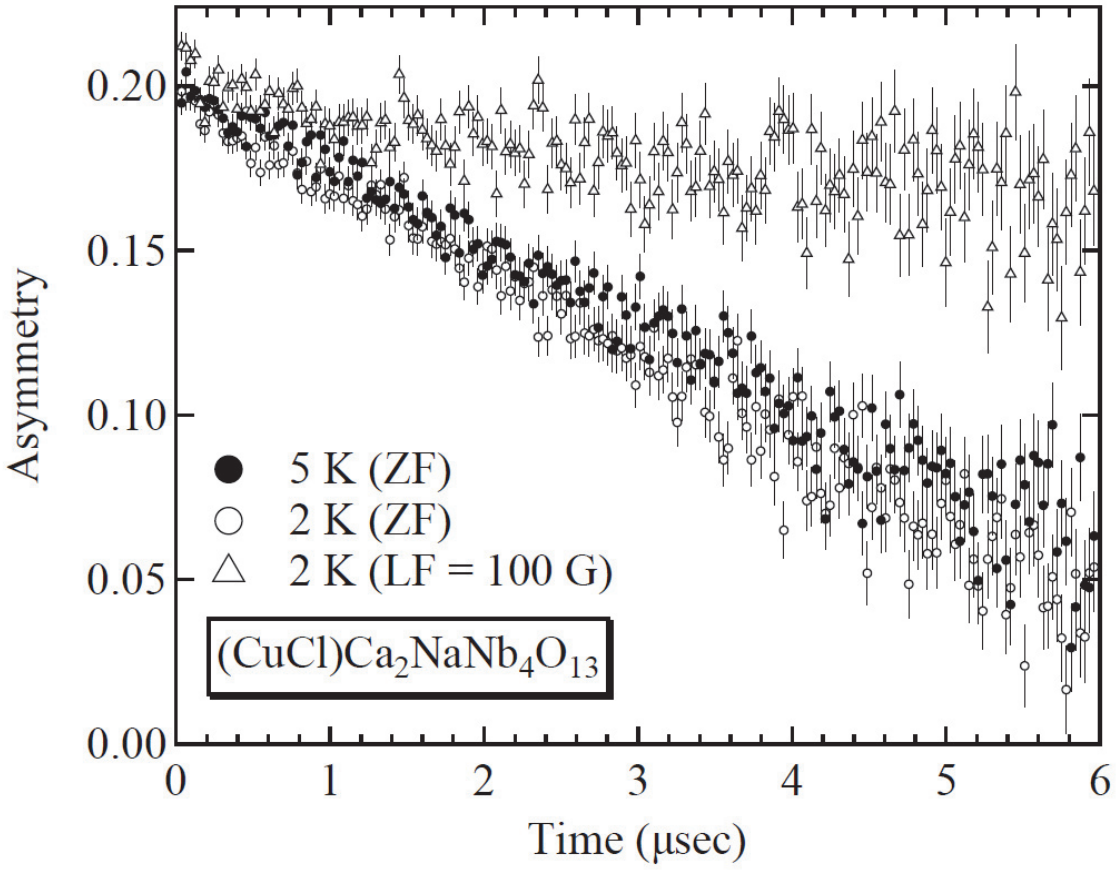

Figure 3.8. Time evolution of μSR asymmetry in zero field (ZF) for $(CuCl)Ca_2NaNb_4O_{13}$ measured at 2 K and 5 K. The decoupled spectrum in a longitudinal field (LF) of 100 G at 2 K is also shown.

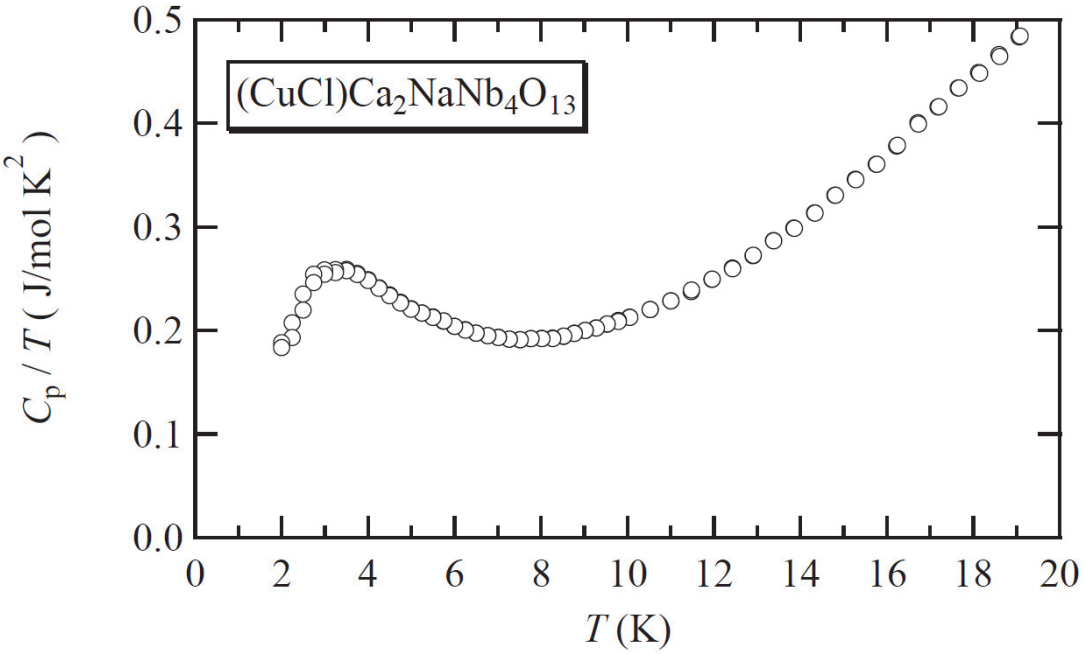

Figure 3.9. Temperature dependence of C_p/T for $(CuCl)Ca_2NaNb_4O_{13}$, showing a Schottky anomaly at around 3 K.

Table 3.1. Crystallographic data for $(CuCl)Ca_2NaNb_4O_{13}$.

	atom	site	x	y	z	g	B_{iso} (Å^2)
$(CuCl)Ca_2NaNb_4O_{13}$	Cu	8*f*	0.25	0.25	0.25	1	1.26(9)
*I*4/*mmm*	Cl(1)	16*m*	0.535(9)	0.535(9)	0.252(1)	0.25	2.8(5)
a = 7.73232(5) Å	Cl(2)	16*k*	0.049(9)	0.549(9)	0.25	0.25	2.8(5)
c = 39.2156(4) Å	*A*(1)	2*a*	0	0	0	1	1.71(7)
R_{wp} = 5.72%	*A*(2)	4*c*	0	0.5	0	1	1.71(7)
R_{Bragg} = 3.25%	*A*(3)	2*b*	0.5	0.5	0	1	1.71(7)
χ^2 = 3.10	*A*(4)	4*e*	0	0	0.108(2)	1	1.71(7)
	A(5)	8*g*	0	0.5	0.107(2)	1	1.71(7)
	A(6)	4*e*	0.5	0.5	0.103(1)	1	1.71(7)
	Nb(1)	16*m*	0.249(1)	0.249(1)	0.0545(1)	1	0.02(1)
	Nb(2)	16*m*	0.251(1)	0.251(1)	0.15774(4)	1	0.02(1)
	O(1)	8*h*	0.233(2)	0.233(2)	0	1	2.29(9)
	O(2)	16*m*	0.233(2)	0.233(2)	0.0997(3)	1	2.29(9)
	O(3)	16*m*	0.233(2)	0.233(2)	0.2011(3)	1	2.29(9)
	O(4)	16*n*	0	0.25	0.0543(4)	1	2.29(9)
	O(5)	16*n*	0	0.25	0.1487(8)	1	2.29(9)
	O(6)	16*n*	0	0.25	0.0428(4)	1	2.29(9)
	O(7)	16*n*	0	0.25	0.1478(8)	1	2.29(9)

Table 3.2. Bond distances for $(CuCl)Ca_2NaNb_4O_{13}$.

Bond	Bond Distances (Å)	Bond	Bond Distances (Å)
Cu-Cl(1)	2 × 2.34(11)	*A*(3)-O(6)	8 × 2.560(10)
	4 × 2.76(1)	*A*(3)-O(1)	4 × 2.913(18)
Cu-Cl(2)	2 × 2.19(10)		
	4 × 2.78(2)	*A*(4)-O(5)	4 × 2.483(46)
Cu-O(3)	2 × 2.1925(13)	*A*(4)-O(4)	4 × 2.886(59)
		A(4)-O(2)	4 × 2.936(9)
Nb(1)-O(4)	2 × 1.937(11)		
Nb(1)-O(2)	1 × 1.939(11)	*A*(5)-O(7)	2 × 2.508(39)
Nb(1)-O(6)	2 × 1.957(11)	*A*(5)-O(5)	2 × 2.532(49)
Nb(1)-O(1)	1 × 1.986(2)	*A*(5)-O(2)	4 × 2.754(6)
		A(5)-O(4)	2 × 2.829(45)
Nb(2)-O(3)	1 × 1.712(13)		
Nb(2)-O(7)	2 × 1.963(9)	*A*(6)-O(2)	4 × 2.558(3)
Nb(2)-O(5)	2 × 1.973(9)	*A*(6)-O(7)	4 × 2.600(49)
Nb(2)-O(2)	1 × 2.283(10)		
A(1)-O(1)	4 × 2.554(18)		
A(1)-O(4)	8 × 2.876(13)		
A(2)-O(6)	4 × 2.560(10)		
A(2)-O(1)	4 × 2.739(1)		
A(2)-O(4)	4 × 2.876(13)		

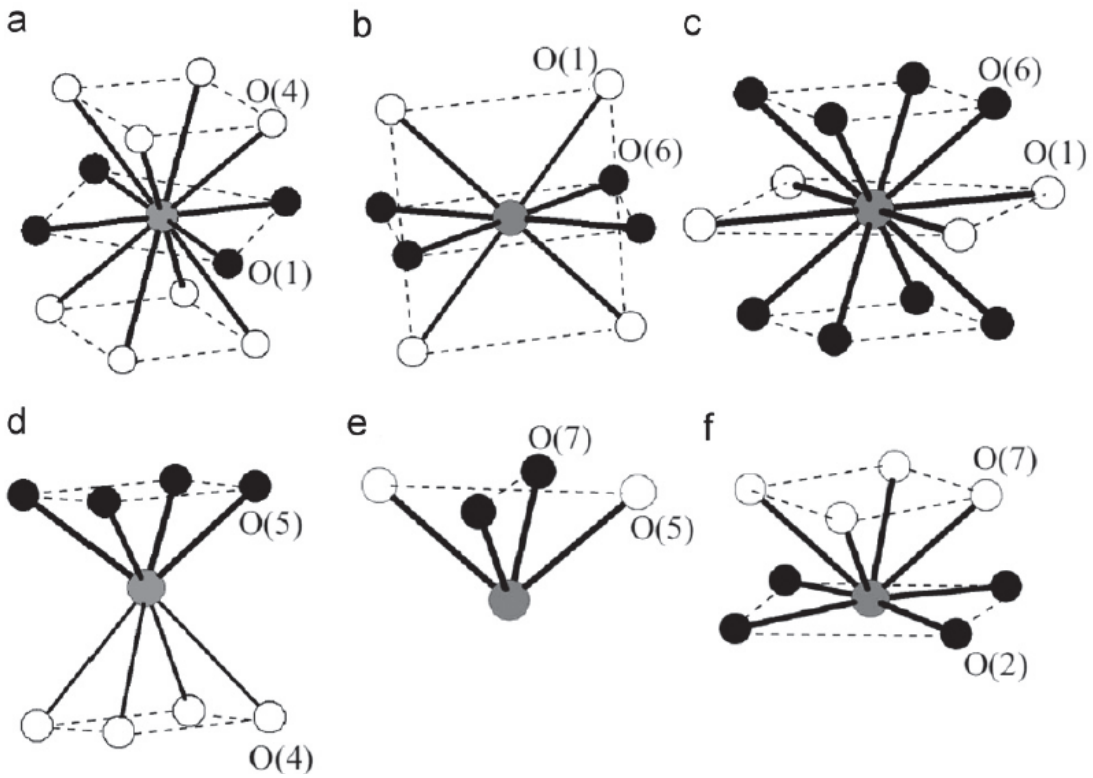

Figure 3.10. Coordination environment of the *A*-site cation in $(CuCl)Ca_2NaNb_4O_{13}$. The lightly shaded circles represent the *A*-site cations. The filled circles with the thicker solid lines represent the nearest oxygen atoms and the open circles with the thinner solid lines the second coordination sphere. The dotted lines are guides to the eye.

Chapter 4. Highly Reduced Anatase $TiO_{2-\delta}$ Thin Films Obtained via Low-Temperature Reduction

4.1. Introduction

Titanium dioxide (TiO_2) is a wide-gap semiconductor and has been intensively investigated because of its functional properties such as photocatalysis, high refractive index and high dielectric constant. TiO_2 has three polymorphs: rutile, anatase, and brookite. Among them, anatase has attracted recent attention in electronics because of its ability to take a Ti^{4+}-Ti^{3+} mixed valence state by chemical modifications, allowing potential applications to a transparent conductor [1, 2], a cheap alternative to indium tin oxide (ITO).

Electrical properties are closely related to the carrier density; thus, systematic control of the chemical composition is of great importance. Carrier control of anatase

TiO_2 has been so far performed mainly by substituting metal and/or introducing oxygen defects [1−7]. In the latter case, oxygen nonstoichiometry was controlled by varying the oxygen partial pressure during growth [3, 4] and by post-annealing with flowing gases such as O_2 and H_2 [5−7]. However, because unlike rutile, anatase is not thermodynamically stable at high temperatures, the reaction temperature has been limited up to ~ 500 °C. Thus the conventional reduction methods limited the value of δ and gave electrical resistivities only down to 10^{-2} Ω cm at room temperature (RT) [3, 5].

Recently, metal hydrides such as CaH_2 and NaH have been used to synthesize several transition metal oxides at low temperatures. This method permits more oxygen vacancies (or lower oxidation states) than other methods [8−11]. This technique was applied to obtain thin films such as AFeO$_2$ (A = Sr, Ca) films from AFeO$_{2.5}$ [12, 13] and $LaNiO_2$ films from $LaNiO_3$ via $LaNiO_{2.5}$ [14]. However, all reduced oxide films using the hydride method have dealt with *discrete* oxygen compositions; between ABO_2 and $ABO_{2.5}$, no intermediate oxygen stoichiometry was found. Nothing has been reported on oxide films with oxygen defects over a wide and continuous range, while doing so might help understand and ultimately control their electrical properties. In this paper, the author reports the preparation and the electrical properties of highly reduced anatase $TiO_{2-\delta}$ thin films using CaH_2 at low temperature.

4.2. Experimental

4.2.1. Sample preparation

The anatase TiO_2 precursor film was grown on a (001) substrate of $LaAlO_3$ (LAO) by pulsed laser deposition (PLD). LAO was chosen not only because the lattice

mismatch between LAO and anatase is quite small (−0.2%), but also because LAO is not reduced by CaH_2. A rutile TiO_2 ceramic target (99.99% purity) was ablated by a KrF excimer laser (λ = 248 nm) pulse with an energy of 0.7 J cm^{-2} $shot^{-1}$ and a frequency of 2 Hz. The substrate temperature and oxygen partial pressure were kept at 700 °C and 6.2×10^{-2} Pa, respectively. The film thickness was 60 nm. The as-grown films were embedded in 0.2 g of CaH_2 powder in a Pyrex tube in an Ar-filled glovebox. The tube was sealed in vacuum ($< 4 \times 10^{-2}$ Pa) and kept for 2 h at various reaction temperatures ranging from 360 °C to 500 °C. Excess CaH_2 and residual byproduct CaO on the film surface were removed by ultrasonic washing with hexane.

4.2.2 Characterization

2theta-theta and in-plane X-ray diffraction (XRD) measurements with CuKα radiation between 5º and 80° were performed on the as-grown and reduced films. Only the 004 diffraction peak from the anatase films and the 001, 002, and 003 diffraction peaks from the LAO substrates were seen [3, 4]. The orientation along the *c*-axis was also confirmed by a rocking curve around the 004 diffraction peak. Moreover, in-plane XRD measurements revealed that only 100, 200, and 300 diffraction peaks from the films were seen along LAO <100> direction. These results indicate that the success in obtaining epitaxial anatase $TiO_{2-\delta}$ (00*l*) thin films. Reduction at above 500 °C resulted in a collapse of the anatase structure.

4.2.3. Physical properties

Resistivity (ρ), Hall effect and magnetoresistance (MR) were measured along the in-plane direction by a four-probe method. Ag or Au/Ti was deposited as electrodes.

Hall resistivity was measured with a magnetic field H of $-7\ \mathrm{T} \leq H \leq 7\ \mathrm{T}$. MR was measured at 2 K up to 7 T applied along the in-plane direction.

4.3. Results and Discussion

The as-grown thin film showed relatively high resistivity (~ 10^2 Ω cm) at RT, indicating the presence of very few oxygen defects. Figure 4.1 (a) shows the resistivities versus temperature of the reduced films, labeled with different reaction temperatures of 360 ºC, 380 ºC, 400 ºC, 420 ºC, 440 ºC, 460 ºC, and 500 ºC, as A1−A7, respectively. As seen in Figure 4.1 (a), A1−A5 were metallic at RT, followed by crossover to semiconducting behavior at lower temperatures. The crossover behavior has often been reported both in bulk and thin film systems [3, 5, 6]. The crossover temperatures for A1−A5 were around 213, 96, 72, 108, and 133 K, respectively. In Figure 4.1 (b), the RT resistivities (ρ(RT)) of A1−A5 are plotted against reaction temperature, which should correlate with δ. Among these films, the lowest ρ(RT) was obtained at the intermediate δ (A3). In particular, ρ(RT) of metallic A3 with optimal δ reached as low as 8×10^{-3} Ω cm, about four times lower than the lowest ρ(RT) obtained for previously reported anatase $TiO_{2-\delta}$ films (3×10^{-2} Ω cm) with a similar metal-semiconductor crossover [3, 5]. In addition, Hall measurements revealed that the carriers in A3 film are n-type with very large carrier density (n) of 1.6×10^{21} cm^{-3} at RT, considerably larger than that reported in ref. 3 (3×10^{17} cm^{-3}) and ref. 5 (6×10^{19} cm^{-3}). The obtained value of n for the non-metal-doped anatase film is comparable with those of 6%-Nb and 5%-Ta substituted anatase TiO_2 films (1.7×10^{21} cm^{-3} and 1.4×10^{21} cm^{-3}, respectively) and ITO films (8×10^{20} cm^{-3}), although their ρ(RT) are 10^{-4} Ω cm [1, 2, 15]. In the Nb- and

Ta-doped anatase films, induced mobile electrons correspond to about 90−95% of the substituted metals [1, 2]. Suppose that one oxygen vacancy introduces two carriers. Then, δ in $TiO_{2-\delta}$ is only ~ 0.03 (i.e. 1−2% oxygen vacancy) for A3. However, it is known that in $SrTiO_{2.92}$ (2−3% oxygen vacancies) only 54% of the oxygen vacancies are activated [16], while, when the *B*-site is doped, a high activation level of 70% is achieved even at a high dopant level of $SrTi_{0.8}Nb_{0.2}O_3$ [17]. This is because the random potential originating from the oxygen vacancy is greater than that from the metal substitution. Therefore, it is expected that δ in A3 is much higher than 0.03.

In contrast to A1−A5, $\rho(T)$ of A6 and A7 were semiconducting from RT (Figure 4.2), indicating significant increase in the random potential when δ was further increased. At the same time, however, ρ(RT) of A6 and A7 are about 10 times lower than that of A5, suggesting a sizable increase in n. Notably, ρ(RT) of A6 (7×10^{-3} Ω cm) and A7 (5×10^{-3} Ω cm) are a little lower than that of A3 (8×10^{-3} Ω cm). In order to further understand the conduction mechanisms for A6 and A7, the data were analyzed with the equation

$$\rho(T) = \rho_0 \exp(T_0/T)^{1/(d+1)}, \qquad (4.1)$$

where ρ_0 is a constant; for the three-dimensional (3D) Mott variable range hopping (VRH) model d = 3 [18], and for the Efros-Shklovskii (ES) VRH model, d = 1 (regardless of dimension) [19]. Because anatase consists of edge-shared TiO_6 octahedra in all crystallographic directions, it is natural to consider that the anatase $TiO_{2-\delta}$ is a 3D electron system. The ES-VRH model, which assumes strong Coulomb interactions [19], might be also applied. As shown in Figure 4.2., both models gave reasonable fits to A6

and A7, although the 3D-Mott VRH model can fit the data over a wider temperature range (to 14 K for A6 and 23 K for A7) than the ES-VRH model (only up to 8.7 K for A6 and 7.9 K for A7). Thus, the 3D-Mott VRH model may be more valid and in any case, strong localization due to strong disorder is present. The linear fits in Figure 4.2 enable calculation of T_0 for A6, with $T_0 = 3.51 \times 10^2$ K for the 3D-Mott VRH model and 9.08 K for the ES-VRH model. For A7 T_0 for the 3D-Mott VRH model and the ES-VRH model were 3.11×10^4 K and 9.59×10^1 K, respectively.

Figure 4.3 shows the MR ratio, defined as $(\rho(H\ \mathrm{T}) - \rho(0\ \mathrm{T}))/\rho(0\ \mathrm{T})$, measured at 2 K for some of the obtained films. Surprisingly, multiple sign changes of MR from positive (A1) to negative (A3) to positive (A5 and A6)) were observed as a function of δ. In A1 and A5, the MR seemed to show a typical H^2 dependence at low fields up to 5 T, which can be explained by the scattering of the hopping electrons by impurity centers (i.e. the oxygen defects and the magnetic Ti^{3+} ions. The relatively large positive MR at 7 T of 11% in A1 probably reflects the high mobility of electrons in anatase [3, 6] and/or the many impurity centers. In contrast, the MR in A3 was negative with a relatively small value of −0.7% at 7 T. In general, a system where the sign reversal of MR is observed has both positive and negative factors contributing to the total MR. One possible negative contribution is the quantum interference (QI) effect [20], whereas for the positive contribution the author suspects the scattering of hopping electrons mentioned earlier to be at play. Thus, in A3, δ have increased to the point that the QI effect dominates over carrier scattering. Such a small, negative MR (−2.2% at 9 T) in an anatase $TiO_{2-\delta}$/LAO film was also reported [3]. The value of MR in A5 (8%) is sizably smaller than that in A1 despite the increase of the impurity centers, strongly suggesting more contribution of QI to MR in A5. Additionally, in A6 the MR is positive but a

relatively small value of only 3% at 7 T, indicating the comparable effects between QI and carrier scattering. The observed multiple sign changes of MR as a function of chemical composition are quite unusual. As far as the author knows multiple sign changes of MR has been found only in $GdPd_3$ as a function of magnetic field [21].

4.4. Conclusion

In conclusion, unprecedentedly highly reduced anatase $TiO_{2-\delta}$ thin films were obtained via a low-temperature reduction using CaH_2, with resistivities as low as 10^{-3} Ω cm at RT, covering both metallic and semiconducting states. A considerably large $n \sim 10^{21}$ cm^{-3} was obtained at RT. Complex changes were also observed in the sign and the MR ratio of the films as a function of δ. More theoretical and experimental studies of transport, magnetism and optics are needed to understand these phenomena. Application of the low-temperature reduction to other oxide thin films may open a new avenue to systematically control their magnetoelectric properties.

References

[1] Y. Furubayashi, T. Hitosugi, Y. Yamamoto, K. Inaba, G. Kinoda, Y. Hirose, T. Shimada, and T. Hasegawa: Appl. Phys. Lett. **86** (2005) 252101.

[2] T. Hitosugi, Y. Furubayashi, A. Ueda, K. Itabashi, K. Inaba, Y. Hirose, G. Kinoda, Y. Yamamoto, T. Shimada, and T. Hasegawa: Jpn. J. Appl. Phys. **44** (2005) L1063.

[3] S. D. Yoon, Y. Chen, A. Yang, T. L. Goodrich, X. Zuo, D. A. Arena, K. Ziemer, C. Vittoria, and V. G. Harris: J. Phys.: Condens. Matter **18** (2006) L355.

[4] N. Sbaï, J. Perrière, B. Gallas, E. Millon, W. Seiler, and M. C. Bernard: J. Appl. Phys. **104** (2008) 033529.

[5] H. Tang, K. Prasad, R. Sanjinès, P. E. Schmid, and F. Lévy: J. Appl. Phys. **75** (1994) 2042.

[6] L. Forro, O. Chauvet, D. Emin, Z. Zuppiroli, H. Berger, and F. Lévy: J. Appl. Phys. **75** (1994) 633.

[7] T. Sekiya, T. Yagisawa, N. Kamiya, D. D. Mulmi, S. Kurita, Y. Murakami, and T. Kodaira: J. Phys. Soc. Jpn. **73** (2004) 703.

[8] M. A. Hayward and M. J. Rosseinsky: Chem. Mater. **12** (2000) 2182.

[9] V. V. Poltavets, K. A. Lokshin, S. Dikmen, M. Croft, T. Egami, and M. Greenblatt: J. Am. Chem. Soc. **128** (2006) 9050.

[10] Y. Tsujimoto, C. Tassel, N. Hayashi, T. Watanabe, H. Kageyama, K. Yoshimura, M. Takano, M. Ceretti, C. Ritter, and W. Paulus: Nature **450** (2007) 1062.

[11] M. A. Hayward, M. A. Green, M. J. Rosseinsky, and J. Sloan: J. Am. Chem. Soc. **121** (1999) 8843.

[12] S. Inoue, M. Kawai, Y. Shimakawa, M. Mizumaki, N. Kawamura, T. Watanabe, Y.

Tsujimoto, H. Kageyama, and K. Yoshimura: Appl. Phys. Lett. **92** (2008) 161911.

[13] S. Inoue, M. Kawai, N. Ichikawa, H. Kageyama, W. Paulus, and Y. Shimakawa: Nat. Chem. **2** (2010) 213.

[14] M. Kawai, S. Inoue, M. Mizumaki, N. Kawamura, N. Ichikawa, and Y. Shimakawa: Appl. Phys. Lett. **94** (2009) 082102.

[15] Y. Shigesato, D. C. Paine, and T. E. Haynes: J. Appl. Phys. **73** (1993) 3805.

[16] W. Gong, H. Yun, Y. B. Ning, J. E. Greedan, W. R. Datars, and C. V. Stager: J. Solid. State. Chem. **90** (1991) 320.

[17] S. Ohta, T. Nomura, H. Ohta, M. Hirao, H. Hosono, and K. Koumoto: Appl. Phys. Lett. **87** (2005) 092108.

[18] P. A. Lee, and T. V. Ramakrishnan: Rev. Mod. Phys. **57** (1985) 287.

[19] A. L. Efros and B. I. Shklovskii: J. Phys. C **8** (1975) L49.

[20] V. L. Nguen, B. Z. Spivak, and B. I. Shklovskii: Sov. Phys. JETP **62** (1985) 1021.

[21] A. Pandey, C. Mazumdar, R. Ranganathan, and S. Dattagupta: J. Magn. Magn. Mater. **321** (2009) 2311.

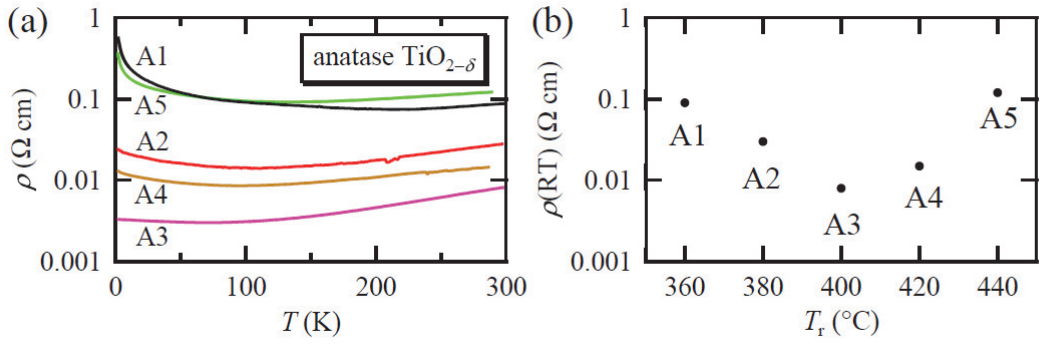

Figure 4.1. (a) Temperature dependence of the resistivity (ρ) of the anatase $TiO_{2-\delta}$ films obtained via low-temperature reduction using CaH_2. The reaction temperatures of the obtained films A1−A5 were systematically changed (see the text for details). (b) Resistivities at room temperature of A1−A5. T_r is the reaction temperature of each film.

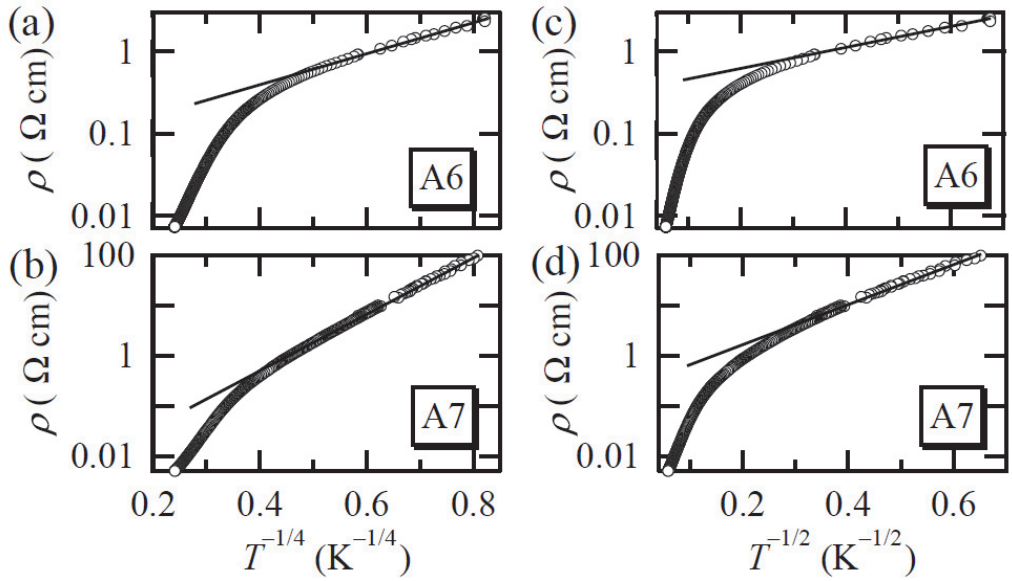

Figure 4.2. Temperature dependence of the resistivities for A6 and A7 with larger oxygen defects than A1−A5. (a), (b) The data fitted by the 3D-Mott VRH model. (c), (d) The data fitted by the ES-VRH model.

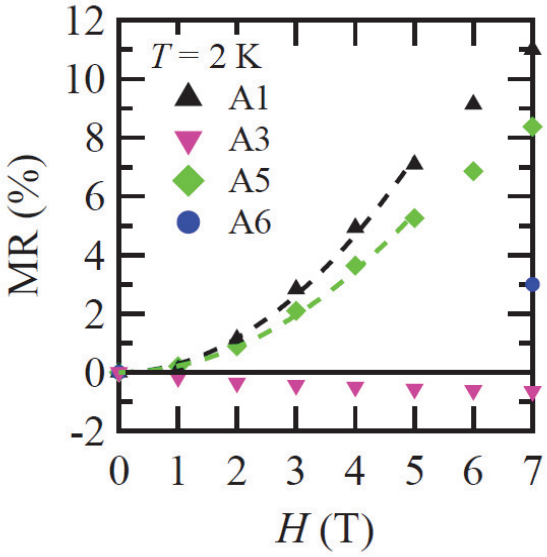

Figure 4.3. Multiple sign changes in the sign of magnetoresistance (MR) observed in the reduced anatase films (A1, A3, A5, A6). Dotted lines show the H^2 fit to the MR of A1 and A5.

Chapter 5. Selective Preparation of Macroporous Monoliths of Conductive Titanium Oxides Ti_nO_{2n-1} (n = 2, 3, 4, 6)

5.1. Introduction

Titanium oxides are generally featured by low environmental burden, biocompatibility, low cost, and chemical stability. A titanium dioxide (Ti(IV)O_2; d^0) as a wide-gap semiconductor exhibits photocatalytic and photovoltaic properties [1, 2]. Reduced titanium oxides with *d* electrons are also attractive regarding transport and magnetic properties; A series of reduced titanium oxides (Ti_nO_{2n-1}; n = 2, 3, 4, ..., 10) undergo Peierls-like metal insulator transitions, which can be controlled by external stimuli such as temperature, light and pressure [3−5], and therefore might be useful for memory and switching devices. Ti_4O_7 (n = 4) finds its applications as electrodes for electrochemical reactions [6, 7].

Porous oxides receive considerable attention because of good mass transport, high surface area, and low density. In particular, when they are of monolithic form, various applications can be found, including electrodes [6−8], separation media [9−11], biomedical materials [12], and so on. Such porous oxide monoliths have usually been prepared via the sol-gel process, by polymer or silica template method [6−8, 13−16], or by the phase separation method [9−11, 17−23]. Among the methods available, the phase separation method based on spinodal decomposition allows precise control of pore properties (e.g. pore size and pore volume). It is a simple method that requires adjusting starting compositions and does not require any templates.

Ever since the report on porous silica monoliths [9], various kinds of porous oxide monoliths with well-controlled pore properties have been synthesized using the phase separation method based on spinodal decomposition. Examples include aluminum oxides (Al_2O_3 and $Y_3Al_5O_{12}$) [18, 19], titanium oxides (TiO_2 and $ATiO_3$ (A = Mg, Ca, Sr, Ba)) [11, 20−23], and zirconium oxide (ZrO_2) [24]. However, all of these oxide monoliths are insulators. Therefore, conducting porous oxide monoliths with controlled pore properties would be an appealing system because it would create a new kinds of electrodes and/or electrocatalysts which could alter carboneous materials. As far as the author knows, porous monoliths of conducting oxides have been reported only for Ti_4O_7 (or Ebonex) and (La, Sr)MnO_3, relying on different synthesis strategies; the former is prepared by thermal decomposition of TiO_2 powder and polymer binders, followed by and H_2 reduction [6, 7, 25], while the latter was prepared by heat treatment of the mixture of K_2CO_3, $MnSO_4 \cdot 5H_2O$, La_2O_3 and $SrCO_3$), followed by water rincing to eliminate K_2SO_4 [26]. Unfortunately, in either case it is impossible to precisely control their pore properties.

In this paper the author reports on the selective synthesis, with a zirconium getter, of a series of conducting titanium oxide porous monoliths. As a precursor, an anatase-type TiO_2 monolith prepared via a phase separation method was utilized, which has interconnected and well-defined macropores, Depending on the amount of Zr and the reaction temperature, the TiO_2 monoliths convert to a single phase of Ti_6O_{11}, Ti_4O_7, Ti_3O_5 and Ti_2O_3, with retaining macropore properties of the precursor. Namely, all the obtained monoliths have a uniform pore size distribution and relatively large porosity of about 60%.

5.2. Experimental

5.2.1. Preparation of the porous TiO_2 precursor monoliths

Porous TiO_2 monoliths were prepared according to the sol-gel method reported previously [21]. A TiO_2 gel was obtained utilizing the sol-gel method where the hydrolysis of titanium (IV) *n*-propoxide ($Ti(O^nPr)_4$) was suppressed by a chelating agent and NH_4NO_3. During the spinodal decomposition, the solution separated into a TiO_2 sol phase and a solvent phase, forming a well-defined macroporous structure; the following gelation process fixed the macropore structure, resulting in the macroporous TiO_2 gels. In a typical preparation, 2.0 mL of $Ti(O^nPr)_4$, 1.4 mL of 1-propanol (PrOH) and 1.0 mL of Ethyl acetoacetate (EtAcAc) were mixed in a glass tube. After obtaining a homogeneous yellow solution, 0.175 g of polyethylene oxide (PEO, M_w = 10,000) was added and was stirred at 60 ºC until PEO was completely dissolved. Then, the solution was cooled to 40 ºC and 0.4 mL of 1 M NH_4NO_3 aqueous solution was added slowly with vigorous stirring. After mixing for 3 min, the obtained homogeneous solution was

kept at 40 ºC for 24 h. The obtained gels were washed with ethanol at 60 ºC followed by a stepwise solvent exchange from ethanol to distilled water. The resultant gels were finally immersed in distilled water at 60 ºC for 24 h. After drying the wet gels at 40 ºC, the resultant xerogels were calcined at 600 ºC and 800 ºC for 2 h, resulting in anatase and rutile structure, respectively, with uniform pore size distribution.

5.2.2. Preparation of the Ti_nO_{2n-1} porous monoliths

The reduction of the monolith with elemental zirconium leads to Ti_nO_{2n-1} (n = 2, 3, 4, and 6), as can be expressed as

$$2n\mathrm{TiO_2} + \mathrm{Zr} \rightarrow 2\mathrm{Ti}_n\mathrm{O}_{2n-1} + \mathrm{ZrO_2} \qquad (5.1)$$

The anatase TiO_2 monolith (typically 5 mm in diameter, 5 mm in height) was placed in an evacuated ($< 4 \times 10^{-2}$ Pa) quartz tube, and was separated by approximately 5 mm from a piece of Zr foil (99.2% purity, 0.1 mm in thickness). In all the reaction conditions the author attempted the reaction time of 1 day and heating/cooling rates of 100 ºC/h were employed, while the TiO_2/Zr ratio was varied corresponding to Equation 5.1 with 0−10% excess of Zr, and the reaction temperatures were changed between 1000 ºC and 1180 ºC. To obtain single phases of Ti_nO_{2n-1}, the calcined anatase TiO_2 monolith (~ 5mm ϕ, ~ 5 mm in height) was held in an evacuated ($< 4 \times 10^{-2}$ Pa) quartz tube, and was separated by approximately 5 mm from a piece of Zr foil (99.2% purity, 0.1 mm in thickness) with the molar ratio TiO_2 : Zr = 4 : 1.05 (for Ti_2O_3 (n = 2), 6 : 1.05 (for Ti_3O_5 (n = 3)), 8 : 1.05 (for Ti_4O_7 (n = 4)), and 12 : 1.10 (for Ti_6O_{11} (n = 6)). The

sealed tube was heated for 1day at 1150 ºC for Ti_2O_3 and Ti_3O_5, and 1050 ºC for Ti_4O_7 and Ti_6O_{11}, respectively, with heating/cooling rates of 100 ºC/h.

5.2.3. Characterization

Powder X-ray diffraction (XRD) profiles were obtained using Bruker D8 diffractometer in the 2theta range of 10º−60º with 0.02º step. The microstructures of the fractured surfaces of the samples were observed by scanning electron microscopy (SEM) using JSM-6060S, JEOL. Magnetic susceptibility measurements were performed using superconducting quantum interference device (SQUID, Quantum Design MPMS) under a magnetic field of 1 T between 5 and 300 K. Magnetic susceptibility measurements at high temperature (> 300 K) were performed at the Institute for Solid State Physics (ISSP), the University of Tokyo. Electrical resistivity of each specimen was measured by four probe method using Quantum Design PPMS. A mercury porosimeter (Pore Master 60-GT, Quantachrome Instruments, USA) was used to characterize the macropores of the samples, while helium pycnometry (Accupyc 1330, Micromeritics, USA) was employed to determine the skeletal density of the samples. The bulk density was calculated from the weight and volume calculated from precisely measured dimensions of each specimen. The porosity of each sample was calculated as (1 − [bulk density]/[skeletal density]) × 100 %.

5.3. Results and discussion

Typical reaction conditions are listed in Table 5.1. In all cases, the reaction time of 1 day and heating/cooling rates of 100 ºC/h were employed. The use of stoichiometric

TiO_2/Zr ratio in Equation 5.1 always resulted in a contamination of less-reduced (i.e. larger *n*) phases, together with the purpose phase, due to incomplete oxidation of Zr to ZrO_2. For example, for TiO_2/Zr = 12 (corresponding to *n* = 6), a thermal treatment at 1050 ºC yielded a Ti_6O_{11} and Ti_7O_{13} mixture. Therefore, a 10% excess amount of Zr was used to compensate incomplete oxidation of Zr and to isolate the Ti_6O_{11} phase (see see Figure 5.1). It was also found that what products are formed depends on the reaction temperature. For example, in a molar ratio of TiO_2/Zr = 6/1.05 (*n* ~ 3), reactions at 1100 ºC, 1150 ºC, 1180 ºC resulted in a single phase of Ti_4O_7 (*n* = 4), a single phase of Ti_3O_5 (*n* = 3), and mixed phases of Ti_2O_3 (*n* = 2) and Ti_3O_5 (*n* = 3), respectively (see Figure 5.2). In summary, the typical requirements to obtain single phases are a 5% Zr-excess for Ti_2O_3, Ti_3O_5, and Ti_4O_7, and 10% for Ti_6O_{11}, and the reaction temperature of 1150 ºC for Ti_2O_3 and Ti_3O_5, and of 1050 ºC for Ti_4O_7 and Ti_6O_{11}.

It is highly remarkable that, as displayed in Figure 5.3 (a), the thus obtained compounds Ti_2O_3, Ti_3O_5, Ti_4O_7, and Ti_6O_{11} retain their monolithic shape without noticeable changes in diameter and height without any visible cracks. The reduced Ti_nO_{2n-1} monoliths have an interconnected macropore network with uniform pore size of about 2 μm and relatively high porosity of about 60%, similar to the anatase TiO_2 precursors. Furthermore, reflecting the color change from white to black, they have relatively high electrical conductivities of 10^{1}–10^{-2} Ω cm at room temperature (RT). Details of the pore, magnetic, and electrical properties will be discussed later.

Figure 5.3 (b) exhibits observed and calculated XRD profiles of the precursor anatase TiO_2 and its reduced products Ti_nO_{2n-1} with *n* = 2, 3, 4, 6. While the XRD peaks for anatase TiO_2 are broad (FWHM = 0.276°, for the peak at 25.3°) due to the small crystallite size (20−60 nm),[21] those for the reduced phases are relatively sharp

(FWHM = 0.143° (n = 6), 0.123° (n = 4), 0.098° (n = 3), and 0.062° (n = 2), for the peak at 26.5°, 26.4°, 25.1°, and 23.8°, respectively), which indicate a certain crystal growth and promises good crystallinity. Each XRD pattern of reduced phases resembles the corresponding simulated one without impurities, and the lattice parameters are in excellent agreement with the reported values [27−30]. The temperature dependence of magnetic susceptibilities for the reduced Ti_nO_{2n-1} monoliths (Figure 5.4) exhibits anomalies associate with the Peierls-like metal-insulator transition at around T_{MI} = 130 K for Ti_6O_{11}, around 150 K for Ti_4O_7, around 450 K for Ti_3O_5, and 500 K for Ti_2O_3, respectively, similar to the previous susceptibility data [4, 31]. The electrical resistivity data in Figure 5.5 (a) also show anomalies at around T_{MI} = 150 K for Ti_6O_{11} and around 150 K for Ti_4O_7, while the data for Ti_3O_5 and Ti_2O_3 in Figure 5.5 (b) exhibits semiconducting temperature dependence below 300 K, similar to the previous reports [32, 33]. Compared with the previous data for the Ti_nO_{2n-1} single crystals, the observed anomalies in the magnetic and/or transport measurements for the obtained monoliths were somewhat broad, which may be attributed to the polycrystalline nature.

When a rutile TiO_2 precursor was used instead of anatase, any of reduced phases were not able to be isolated by Zr getter. Here, the rutile TiO_2 precursor was prepared by calcining the dried TiO_2 gels at 800°C for 2 h in air [21]. At the reaction conditions where anatase TiO_2 transformed to Ti_6O_{11}, rutile precursor resulted in mixture of Ti_4O_7, Ti_5O_9, and Ti_6O_{11}. Such a difference was also seen when attempting to synthesize Ti_4O_7 from rutile (see Figure 5.6). However, these observations do not mean that the *direct* transformation from a meta-stable anatase to any of reduced phases is essential for isolating a single phase monolith. It was observed that, when heated up to 700°C in a 100°C/h and rapidly quenched to RT, anatase changed mostly to rutile without the

formation of any reduced phases (See Figure 5.7). The uniform crystallite size in the anatase precursor monoliths might be important for obtaining each single phase.

Despite substantial removal of oxide ions and non-topochemical transformation of lattice frameworks, the macropore properties of the anatase TiO_2 monolith are retained during the reduction. Figures 5.8 (a)−(e) show scanning electron microscopy (SEM) images of anatase TiO_2 precursor, Ti_6O_{11}, Ti_4O_7, Ti_3O_5, and Ti_2O_3, respectively. All the images of the reduced oxides demonstrate interconnected pore structures, similar to that of the precursor. In Ti_2O_3, the most reduced material, pinhole-like pores are seen on the surface. Mercury porosimetry measurements as shown in Figure 5.8 (f) demonstrate that all materials possess uniform macropores of around 2 μm; in addition, the macropore diameter and volume are almost the same in all samples, which indicates that the well-defined macroporous structure of the precursor monolith was retained through the reduction by Zr.

Table 5.2. summarizes the densities, porosities, and electrical resistivities at RT of the obtained monoliths and a commercial Ebonex made from Ti_4O_7/Ti_5O_9 [6]. The skeletal densities of the Ti_nO_{2n-1} monoliths (4.25−4.38 g cm^{-3}) agree well with the expected densities (4.25−4.57 g cm^{-3}) calculated from previous reports [28−30]. Moreover, the bulk density of each porous Ti_nO_{2n-1} material is estimated to be 1.75−1.85 g cm^{-3}, and gives a porosity as large as 57−60%, which is close to that of the precursor (64%). To the best of the author's knowledge, such low bulk densities and large porosities [6] have not been achieved in porous monoliths of reduced titanium oxides; for example, the commercially available Ebonex, has a bulk density about two times larger (3.6−3.8 g cm^{-3}) and a porosity about three times smaller (20%) [6]. Furthermore, all the reduced monoliths have relatively low electrical conductivities in

the range of 10^{1}−10^{-2} Ω cm at RT (see Table 5.2.). In particular, the resisitivity of Ti_4O_7 porous monolith is 1.5×10^{-2} Ω cm, lower than the lowest values of Ebonex (2×10^{-2} Ω cm at RT) where a less conducting Ti_5O_9 exists as a secondary phase [6].

Because of higher corrosion resistance, and wider potential windows compared to carbon electrodes, Ebonex electrodes have been commercially utilized in bipolar batteries, remediation of waste soil or water, and so on [6, 7]; they have also been studied in terms of oxygen/hydrogen evolution and/or oxygen reduction for fuel cells [34−37], and oxidation of harmful molecules such as sulfur dioxide and halogenated organic species in waste aqueous solutions [38, 39]. The obtained Ti_nO_{2n-1} macroporous monoliths should be advantageous over the commercial porous Ebonex in terms of bulk densities, porosities, and fluid permeabilities. Notably, the success in the selective preparation of Ti_2O_3, Ti_3O_5, Ti_4O_7, and Ti_6O_{11} as a single phase can give the opportunity to compare the support effect of each Ti_nO_{2n-1} porous monoliths when used as a catalyst support.

5.4. Conclusion

In summary, it is reported that the selective preparation of macroporous monoliths of titanium oxides Ti_nO_{2n-1} with n = 2 (Ti_2O_3), 3 (Ti_3O_5), 4 (Ti_4O_7) and 6 (Ti_6O_{11}) by simply reducing macroporous anatase TiO_2 monoliths using a zirconium getter. The obtained monoliths have interconnected macropore networks with uniform pore size, with porosities up to 60%, like the anatase precursor. The obtained porous oxide monoliths with the high conductivities and low densities may be useful for a wide range of electrochemical applications. Notably, the merit of the phase separation method i.e.

the fact that the macropore properties of the TiO_2 precursors are easily controllable by adjusting the starting composition [21] may enable us to obtain Ti_nO_{2n-1} monoliths with different pore properties. Furthermore, such redox treatments of existing oxide porous monoliths would give new materials.

References

[1] A. Fujishima and X. Zhang: Comptes Rendus Chimie **9** (2005) 750.

[2] B. O'Regan and M. Gratzel: Nature **353** (1991) 737.

[3] S. Ohkoshi, Y. Tsunobuchi, T. Matsuda, K. Hashimoto, A. Namai, F. Hakoe, and H. Tokoro: Nat. Chem. **2** (2010) 539.

[4] H. Ueda, K. Kitazawa, H. Takagi, and T. Matsumoto: J. Phys. Soc. Japan **71** (2002) 1506.

[5] M. Watanabe, M. Miyasaka, and K. Tanaka: J. Phys.: Conf. Ser. **148** (2009) 012017.

[6] J. R. Smith, F. C. Walsh, and R. L. Clarke: J. Appl. Electrochem. **28** (1998) 1021.

[7] F. C. Walsh and R. G. A. Wills: Electrochim. Acta **55** (2010) 6342.

[8] C. M. Doherty, R. A. Caruso, B. M. Smarsly, P. Adelhelm, and C. J. Drummond: Chem. Mater. **21** (2009) 5300.

[9] K. Nakanishi and N. Soga: J. Am. Ceram. Soc. **74** (1991) 2518.

[10] K. Nakanishi and N. Tanaka: Acc. Chem. Res. **40** (2007) 863.

[11] J. Konishi, K. Fujita, K. Nakanishi, K. Hirao, K. Morisato, S. Miyazaki, and M. Ohira: J. Chromat. A **1216** (2009) 7375.

[12] L. L. Hench: J. Am. Ceram. Soc. **74** (1991) 1487.

[13] M. Breulmann, S. A. Davis, S. Mann, H. P. Hentze, and M. Antonietti: Adv. Mater. **12** (2000) 502.

[14] H. Maekawa, J. Esquena, S. Bishop, C. Solans, and B. F. Chmelka: Adv. Mater. **15** (2003) 591.

[15] G. L. Drisko, A. S. Zelcer, V. Luca, R. A. Caruso, and G. J. d. A. A. Soler-Illia: Chem. Mater. **22** (2010) 4379.

[16] X. Fan, H. Fei, D. H. Demaree, D. P. Brennan, J. M. St. John, and S. R. J. Oliver: Langmuir **25** (2009) 5835.

[17] K. Kanamori and K. Nakanishi: Chem. Soc. Rev. **40** (2011) 754.

[18] Y. Tokudome, K. Fujita, K. Nakanishi, K. Miura, and K. Hirao: Chem. Mater. **19** (2007) 3393.

[19] Y. Tokudome, K. Fujita, K. Nakanishi, K. Kanamori, K. Miura, K. Hirao, and T. Hanada: J. Ceram. Soc. Jpn. **115** (2007) 925.

[20] J. Konishi, K. Fujita, K. Nakanishi, and K. Hirao: Chem. Mater. **18** (2006) 864.

[21] G. Hasegawa, K. Kanamori, K. Nakanishi, and T. Hanada: J. Am. Ceram. Soc. **93** (2010) 3110.

[22] O. N. Ruzimuradov, G. Hasegawa, K. Kanamori, and K. Nakanishi: J. Ceram. Soc. Jpn. **119** (2011) 440.

[23] O. Ruzimuradov, G. Hasegawa, K. Kanamori, and K. Nakanishi: J. Am. Ceram. Soc. **94** (2011) 3335.

[24] J. Konishi, K. Fujita, S. Oiwa, K. Nakanishi, and K. Hirao: Chem. Mater. **20** (2008) 2165.

[25] K. Kolbrecka and J. Przyluski: Electrochim. Acta **39** (1994) 1591.

[26] E. S. Toberer, J. C. Weaver, K. Ramesha, and R. Seshadri: Chem. Mater. **16** (2004) 2194.

[27] J. K. Burdett, T. Hughbanks, G. J. Miller, J. W. Richardson, and J. V. Smith: J. Am. Chem. Soc. **109** (1987) 3639.

[28] C. E. Rice and W. R. Robinson: Mater. Res. Bull. **11** (1976) 1355.

[29] S. Asbrink and A. Magneli: Acta Crystallogr. **12** (1959) 575.

[30] Y. Le Page and P. Strobel: J. Solid State Chem. **43** (1982) 314.

[31] L. K. Keys and L. N. Mulay: Appl. Phys. Lett. **9** (1966) 248.

[32] C. N. R. Rao, S. Ramdas, R. E. Loehman, and J. M. Honig: J. Solid State Chem. **3** (1971) 83.

[33] J. M. Honig and T. B. Reed: Phys. Rev. **174** (1968) 1020.

[34] P. Paunović, O. Popovski, E. Fidanevska, B. Ranguelov, D. S. Gogovska, A. T. Dimitrov, and S. H. Jordanov: Int. J. Hydro. Energy **35** (2010) 10073.

[35] V. Rashkova, S. Kitova, and T. Vitanov: Electrochim. Acta **52** (2007) 3794.

[36] T. Ioroi, Z. Siroma, N. Fujiwara, S. I. Yamazaki, and K. Yasuda: Electrochem. Comm. **7** (2005) 183.

[37] G. Chen, S. R. Bare, and T. E. Mallouk: J. Electrochem. Soc. **149** (2002) A1092.

[38] K. Scott, W. Taama, and H. Cheng: Chem. Eng. J. **73** (1999) 101.

[39] G. Chen, E. A. Betterton, R. G. Arnold, and W. P. Ela: J. Appl. Electrochem. **33** (2003) 161.

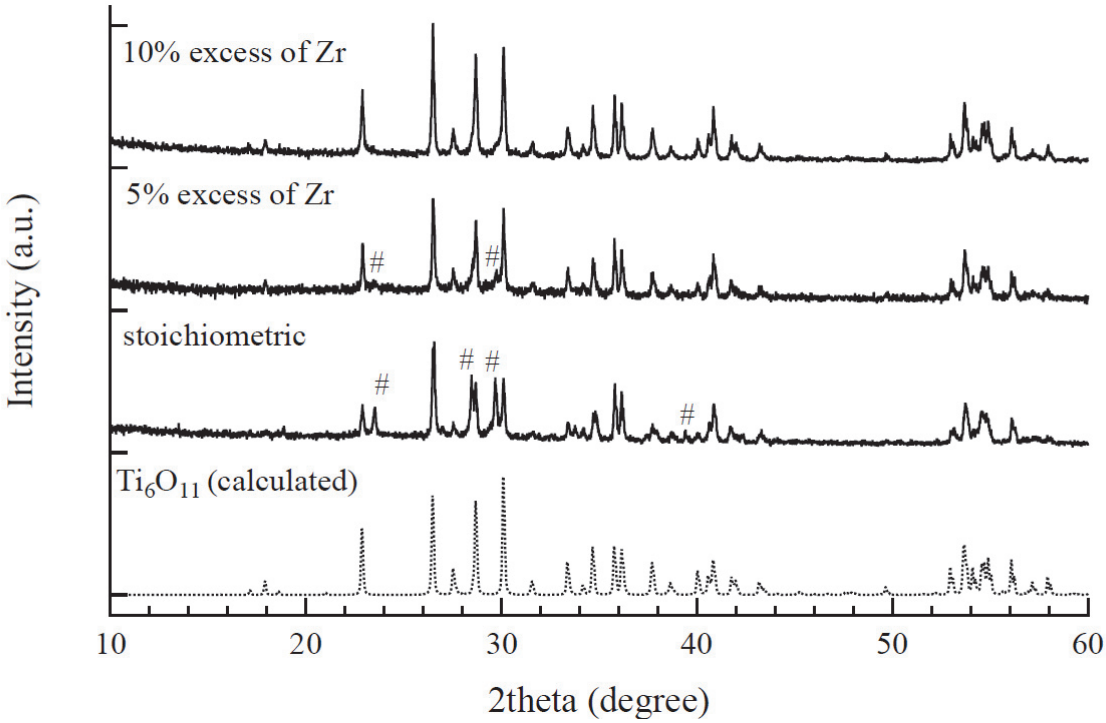

Figure 5.1. Attempts to prepare Ti_6O_{11} where proper amount of Zr was examined. From up to bottom, preparation with 10% excess of Zr, 5% excess of Zr, and stoichiometric amount of Zr. In all cases, reaction temperatures were 1050 ºC, cooling/heating rate was 100 ºC/h, and reaction time was 1 d. Dotted lines show the calculated X-ray diffraction (XRD) patterns for Ti_6O_{11}. Pound signs represent Ti_7O_{13}.

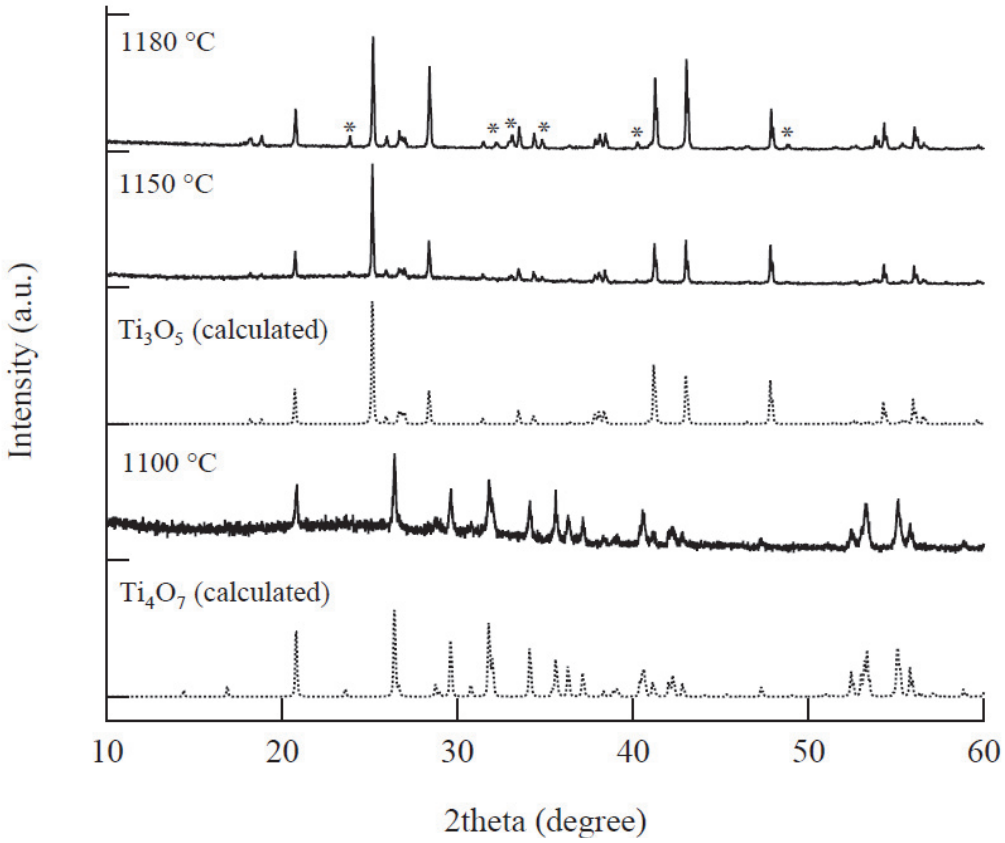

Figure 5.2. Attempts to prepare Ti_3O_5 where reaction temperature was controlled. Solid lines show, from up to bottom, results for the reduction at 1180 ºC, 1150 ºC, and 1100 ºC, respectively. Stars represent Ti_2O_3. Dotted lines show the calculated XRD patterns for rutile Ti_4O_7 (bottom) and Ti_3O_5 (top), respectively.

Table 5.1. Typical reaction conditions and results in case of anatase TiO_2 precursors.

heating/cooling rate (ºC/h)	reaction temperature (ºC)	TiO_2 : Zr	result
100	1050	12 : 1	Ti_6O_{11}, Ti_7O_{13}
100	1000	10 : 1	Ti_4O_7, Ti_5O_9, Ti_6O_{11}
100	1000	12 : 1	Ti_6O_{11}, Ti_7O_{13}, Ti_9O_{17}
100	1100	6 : 1	Ti_4O_7
100	1050	12 : 1	Ti_6O_{11}, Ti_7O_{13}
100	1050	12 : 1.05	Ti_6O_{11}, Ti_7O_{13}
100	1050	12 : 1.1	Ti_6O_{11}
100	1180	6 : 1.1	Ti_2O_3, Ti_3O_5
100	1150	6 : 1.1	Ti_2O_3, Ti_3O_5
100	1050	8 : 1.05	Ti_4O_7
100	1050	12 : 1.05	Ti_6O_{11}
100	1150	6 : 1.05	Ti_3O_5
100	1150	4 : 1.05	Ti_2O_3

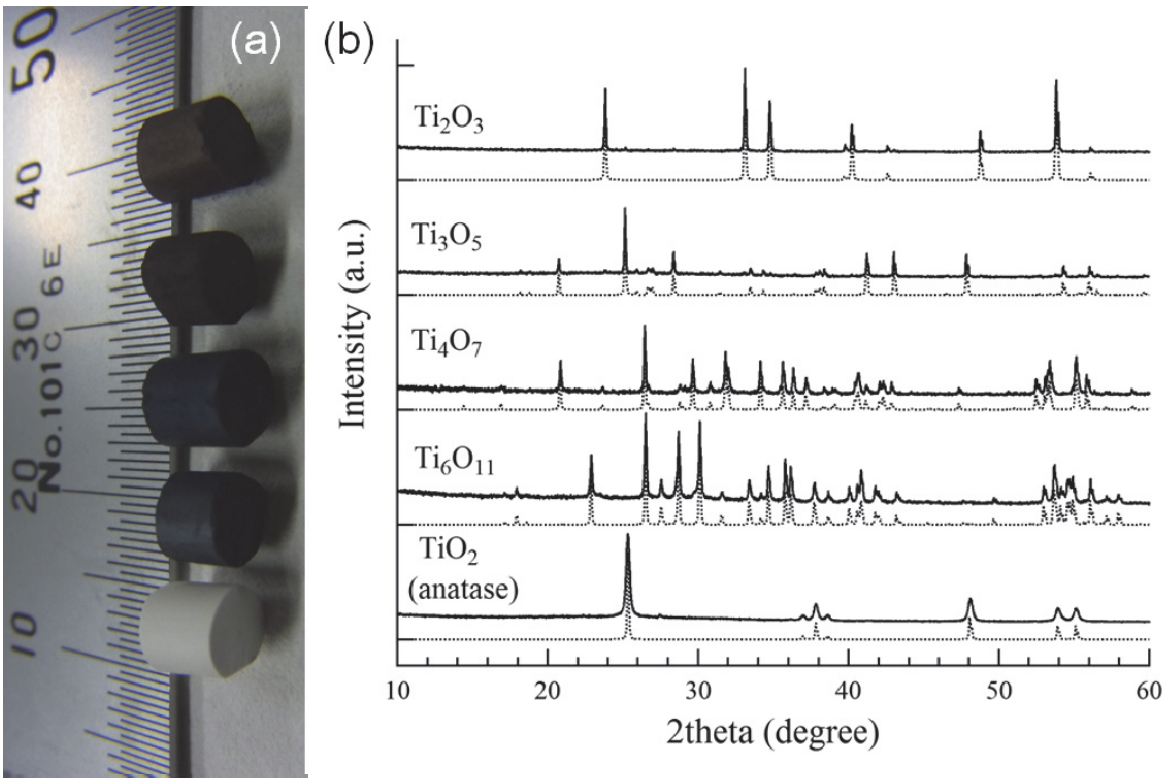

Figure 5.3. (a) Photographs and (b) observed (solid) and calculated (dotted) XRD profiles of anatase TiO_2, Ti_6O_{11}, Ti_4O_7, Ti_3O_5, and Ti_2O_3 monoliths (from bottom to top).

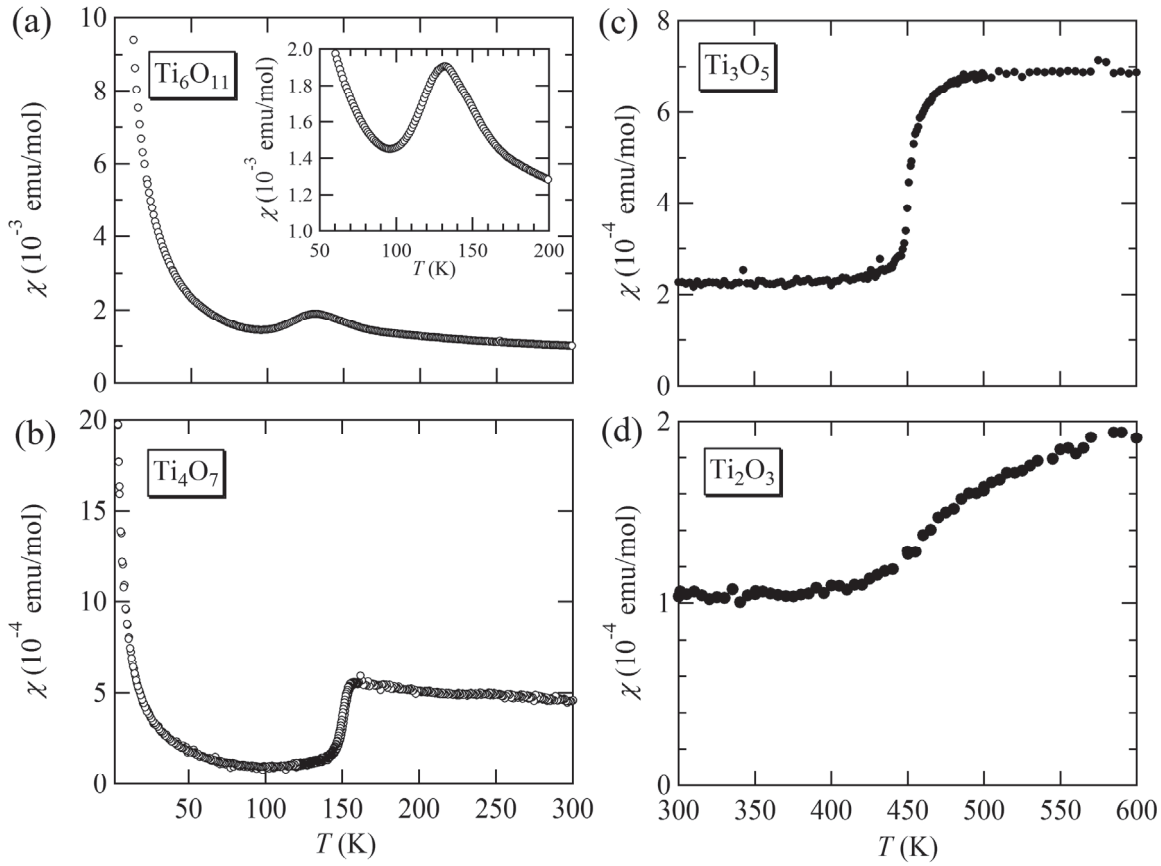

Figure 5.4. Temperature dependence of the magnetic susceptibilities χ of (a) Ti_6O_{11}, (b) Ti_4O_7, (c) Ti_3O_5, and (d) Ti_2O_3. Inset in (a) is an enlarged plot.

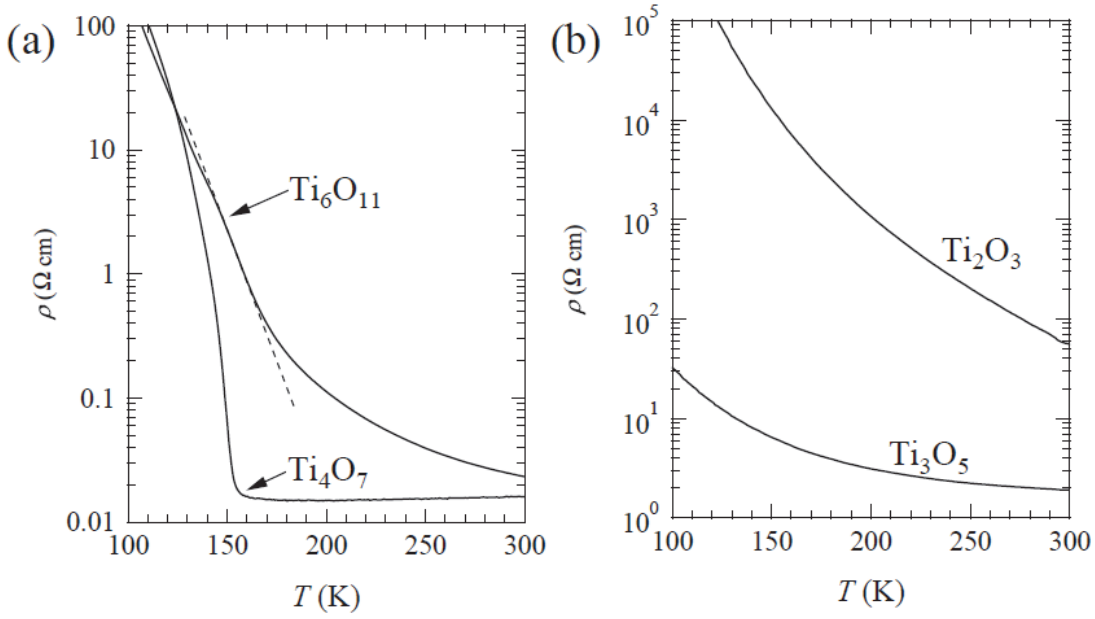

Figure 5.5. Temperature dependence of the electrical resistivities ρ of (a) Ti_6O_{11} and Ti_4O_7 (b) Ti_3O_5 and Ti_2O_3. Dotted lines in (a) are guide to the eye.

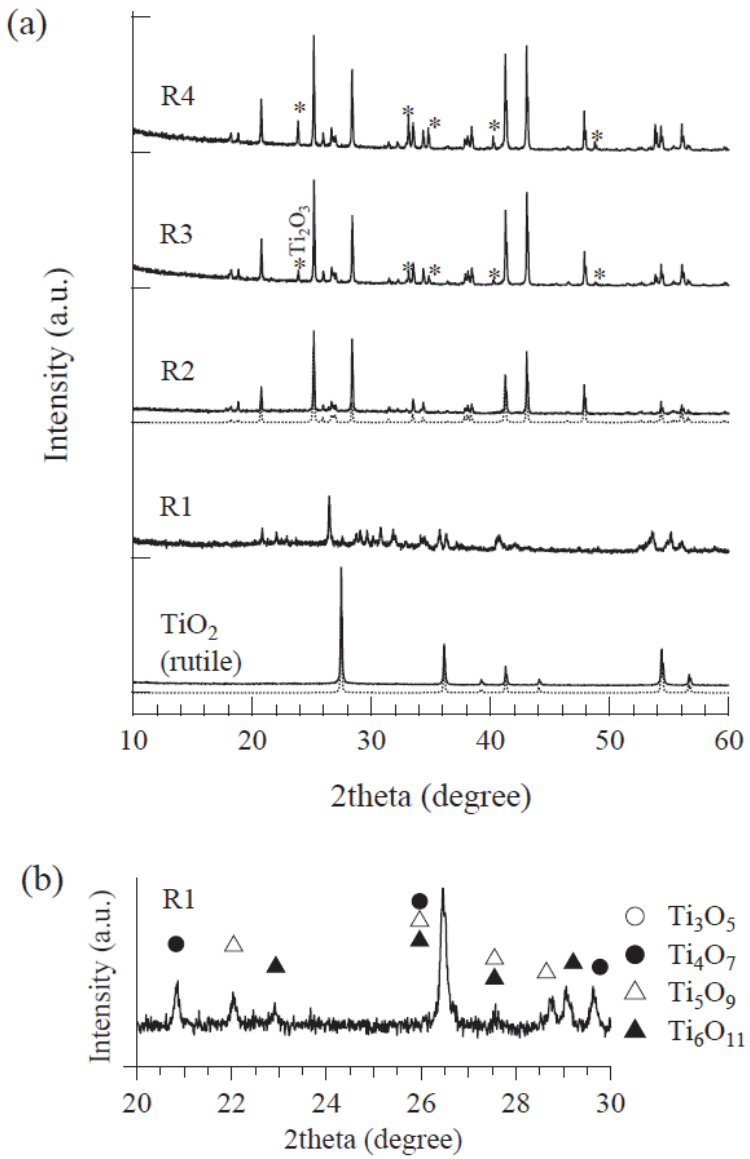

Figure 5.6. XRD profiles of the macroporous monoliths of rutile TiO_2 (calcined at 800 ºC for 2 h) and the reduced ones. R1–R4 represents the reduced monoliths in the reaction conditions for n = 6, 4, 3 and 2 in the case of anatase precursors, respectively. Stars in (a) represent Ti_2O_3. Dotted lines in (a) show the calculated XRD patterns for rutile TiO_2 (bottom) and Ti_3O_5 (top), respectively. Inset is the enlarged plot of the XRD profile of R1. Open circles stand for Ti_3O_5, closed circles stand for Ti_4O_7, open triangles stand for Ti_5O_9, and closed triangles stand for Ti_6O_{11}.

Table 5.2. Bulk electrical resistivities, densities, and porosities at room temperature (RT) of anatase TiO_2 and Ti_nO_{2n-1} monoliths (n = 2, 3, 4, 6) and a commercial porous Ebonex.

sample	Estimated skeletal density [g cm^{-3}]	Reported true density [g cm^{-3}]	Bulk density [g cm^{-3}]	Porosity [%]	Bulk Resistivity at RT [Ω cm]
Ti_2O_3	4.38	4.57 [a]	1.75	60	5.6×10^{1}
Ti_3O_5	4.25	4.25 [b]	1.78	58	1.9×10^{0}
Ti_4O_7	4.33	4.32 [c]	1.82	58	1.5×10^{-2}
Ti_6O_{11}	4.28	4.30 [c]	1.85	57	2.0×10^{-2}
TiO_2	3.83	3.89 [d]	1.39	64	–
porous Ebonex[e]	–	–	3.6–3.8	20	$(2.0–4.0) \times 10^{-2}$

[a] calculated from the values obtained from ref. 28.

[b] calculated from the values obtained from ref. 29.

[c] calculated from the values obtained from ref. 30.

[d] calculated from the values obtained from ref. 27.

[e] data were obtained in ref. 6.

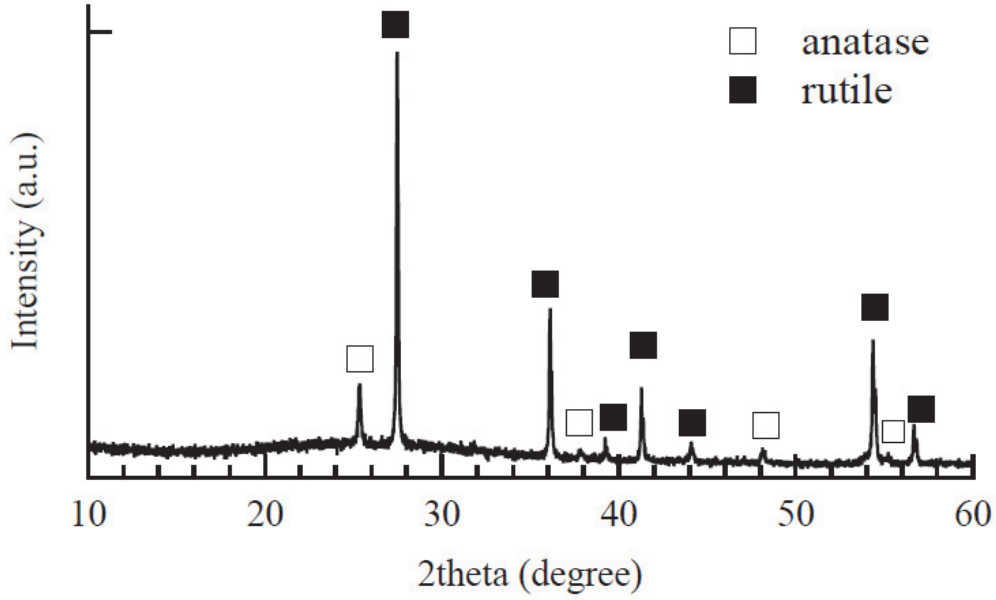

Figure 5.7. XRD profile of the anatase TiO_2 precursor monolith measured after a 100°C/h heating to 700°C and a rapid quenching to RT. The precursor monolith was sealed in an evacuated silica tube with Zr foil in the molar ratio of TiO_2 : Zr = 8 : 1.05.

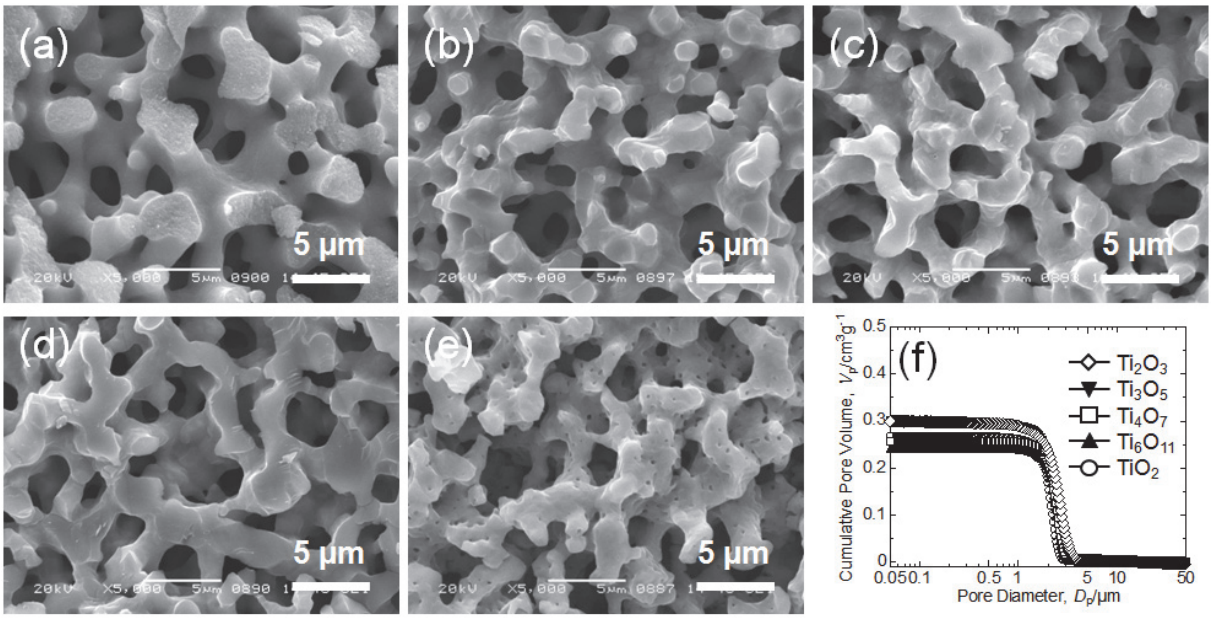

Figure 5.8. (a)−(e) SEM images of macroporous monoliths of (a) anatase TiO_2, (b) Ti_6O_{11}, (c) Ti_4O_7, (d) Ti_3O_5, and (e) Ti_2O_3. (f) mercury porosimetry results of anatase TiO_2 and its reduced Ti_nO_{2n-1} monoliths.

General conclusion

This thesis focused on the magnetic and electrical properties of transition metal oxides obtained using structurally related (in the sense of crystal structures and morphologies) precursors.

In Chapter 1, the temperature variations of the specific heat and magnetization were measured for the ion-exchanged layered copper oxyhalide $(CuCl)LaNb_2O_7$. The results provide evidence that no magnetic ordering down to as low as 2 K and that the Bose-Einstein Condensation (BEC) occurs at almost as half as was expected (18 T) from the size of its zero-field gap. It is highly possible that $(CuCl)LaNb_2O_7$ provides a new mechanism that leads to the BEC.

In Chapter 2, a quantum phase transition from spin-disordered state to antiferromagnetic order as a function of x in (CuCl)La($Nb_{1-x}Ta_x$)$_2O_7$ was reported. It is found that (CuCl)$LaTa_2O_7$ exhibits, despite the closeness of the lattice parameters in the solid solution, collinear (or stripe) antiferromagnetic (CAF) order at $T_N \sim 7$ K. This clearly shows that the substitution of Ta^{5+} for Nb^{5+} in nonmagnetic slabs can affect the ground state of this quasi-2D magnet. The spin-disordered ground state in (CuCl)$LaNb_2O_7$ is fairly robust against Ta substitution ($0 \leq x \leq 0.4$), accompanied by a slight reduction of the spin gap, which is in marked contrast to the drastic collapse of the spin disorder in ($CuCl_{0.95}Br_{0.05}$)$LaNb_2O_7$. In the intermediate region ($0.4 < x < 1.0$), CAF order was observed but with a nearly constant T_N, likely coexisting with the spin-disordered state with systematic variation of the volume fraction. This is in stark contrast to the case of ($CuCl_{1-y}Br_y$)$LaNb_2O_7$ where T_N increases gradually from 7 K (y = 0.05) to 32 K (y = 1.0).

In Chapter 3, a quadruple-layered copper oxyhalide (CuCl)$Ca_2NaNb_4O_{13}$ was reported. Via topotactic ion-exchange with $CuCl_2$, the precursor $RbCa_2NaNb_4O_{13}$ with diffuse superreflections changes into (CuCl)$Ca_2NaNb_4O_{13}$ with a well-defined, tetragonal $2a_p \times 2a_p \times 2c_p$ superstructure. The insertion of the edge-shared $CuCl_4O_2$ layer induces strong bonding between the neighboring perovskite slabs, likely stabilizing the superstructure. Magnetic studies reveal that (CuCl)$Ca_2NaNb_4O_{13}$ does not undergo magnetic long-range ordering down to 2 K despite strong magnetic interaction in the CuCl plane, due to the enhanced quantum fluctuations in two dimensions. Group theory analysis together with the synchrotron XRD and TEM measurements suggests the $I4/mmm$ space group with an unusual in-phase two-tilt system (++0) in (CuCl)$Ca_2NaNb_4O_{13}$.

In Chapter 4, it is reported that unprecedentedly highly reduced anatase $TiO_{2-\delta}$ thin films were prepared via a low-temperature reduction using CaH_2. The resistivities were as low as 10^{-3} Ω cm at room temperature, covering both metallic and semiconducting states. Furthermore, a considerably large carrier density of $n \sim 10^{21}$ cm^{-3} was obtained at room temperature. These films also showed complex changes in the sign and the ratio of magnetoresistance (MR) as a function of δ.

In Chapter 5, the author reported the selective preparation of macroporous monoliths of oxygen deficient titanium oxides Ti_nO_{2n-1} with n = 2 (Ti_2O_3), 3 (Ti_3O_5), 4

(Ti_4O_7) and 6 (Ti_6O_{11}), by simply reducing macroporous anatase TiO_2 monoliths using a zirconium getter. The obtained monoliths have interconnected macropore networks with uniform pore size, with porosities up to 60%, like the anatase precursor.

Future experiments

As described above, the layered copper oxyhalides $(CuCl)LaNb_2O_7$ are square-lattice-based two-dimensional (2D) quantum magnets showing a spin-disordered ground state. However, there remains several open issues such as i) the mechanism of BEC in this compound, and ii) sizable effect on magnetism by elemental substitutions. Very recently, a success in growing a single crystal of $(CuCl)LaNb_2O_7$ was reported, where structural reinvestigation was also performed [1]. To understand the detailed magnetic properties in the present compound together with its family compounds, measurements using single crystals are required. Besides, further search for the related new materials are of interest: for example, applying the ion-exchange reaction to other layered perovskites $A'A_{n-1}B_nO_{3n+1}$ with $n > 4$ may allow us to obtain more 2D materials with further enhanced quantum fluctuations.

In this work, studies on reduction of titanium dioxide (TiO_2) with specific morphologies (i.e. thin films and porous monoliths) have been presented. As for the obtained, reduced anatase $TiO_{2-\delta}$ thin films, more theoretical and experimental studies of transport, magnetism and optics are needed to understand the complex phenomena such as MR results. Moreover, application of the low-temperature reduction to other oxide thin films may open a new avenue to systematically control their magnetoelectric properties. The obtained Ti_nO_{2n-1} macroporous monoliths with high electrical conductivities and high fluid permeabilities may be useful for a wide range of electrochemical applications. Notably, the phase separation method allows the control of the macropore properties of the TiO_2 precursors simply by adjusting the starting composition [2]: thus it is highly possible to obtain Ti_nO_{2n-1} monoliths with different pore properties. Furthermore, such redox treatments of existing oxide porous monoliths would give new materials (e. g. porous TiN monoliths from TiO_2).

References

[1] O. J. Hernandez, C. Tassel, K. Nakano, W. Paulus, C. Ritter, E. Collet, A. Kitada, K. Yoshimura, and H. Kageyama: Dalton Trans. **40** (2011) 4605.

[2] G. Hasegawa, K. Kanamori, K. Nakanishi, and T. Hanada: J. Am. Ceram. Soc. **93** (2010) 3110.

List of Publications

Chapter 1

Bose-Einstein Condensation of Quasi-Two-Dimensional Frustrated Quantum Magnet (CuCl)$LaNb_2O_7$

Atsushi Kitada, Zenji Hiroi, Yoshihiro Tsujimoto, Taro Kitano, Hiroshi Kageyama, Yoshitami Ajiro, and Kazuyoshi Yoshimura

Journal of the Physical Society of Japan **76** (2007) 093706/1−4.

Chapter 2

Quantum phase transition in (CuCl)$La(Nb_{1-x}Ta_x)_2O_7$

Atsushi Kitada, Yoshihiro Tsujimoto, Hiroshi Kageyama, Yoshitami Ajiro, Masakazu Nishi, Yasuo Narumi, Koichi Kindo, Masaki Ichihara, Yutaka Ueda, Yasutomo J. Uemura, and Kazuyoshi Yoshimura

Physical Review B **80** (2009) 174409/1−5.

Chapter 3

Quadruple-layered perovskite (CuCl)$Ca_2NaNb_4O_{13}$

Atsushi Kitada, Yoshihiro Tsujimoto, Takafumi Yamamoto, Yoji Kobayashi, Yasuo Narumi, Koichi Kindo, Adam A. Aczel, Yasutomo J. Uemura, Yoko Kiuchi, Yutaka Ueda, Kazuyoshi Yoshimura, Yoshitami Ajiro, and Hiroshi Kageyama

Journal of Solid State Chemistry **185** (2012) 10-17.

Chapter 4

Highly-Reduced Anatase $TiO_{2-\delta}$ Thin Films via Low-Temperature Reduction

Atsushi Kitada, Shigeru Kasahara, Takahito Terashima, Kazuyoshi Yoshimura, Yoji Kobayashi, and Hiroshi Kageyama

Applied Physics Express **4** (2011) 035801/1−3.

Chapter 5

Selective Preparation of Macroporous Monoliths of Conductive Titanium Oxides Ti_nO_{2n-1} (n = 2, 3, 4, 6)

Atsushi Kitada, George Hasegawa, Yoji Kobayashi, Kazuyoshi Kanamori, Kazuki Nakanishi, and Hiroshi Kageyama

submitted.

The following papers are not included in this thesis

Spin-Ladder Iron Oxide $Sr_3Fe_2O_5$

Hiroshi Kageyama, Takashi Watanabe, Yoshihiro Tsujimoto, Atsushi Kitada, Yuji Sumida, Kazuyoshi Kanamori, Kazuyoshi Yoshimura, Naoaki Hayashi, Shigetoshi Muranaka, Mikio Takano, Monica Ceretti, Werner Paulus, Cremens Ritter, and Gilles André

Angewandte Chemie International Edition **47** (2008) 5740−5745.

Muon spin relaxation studies of the frustrated quasi-two-dimensional square-lattice spin system Cu(Cl, Br)La(Nb, $Ta)_2O_7$: Evolution from spin-gap to antiferromagnetic state

Yasutomo J. Uemura, Adam A. Aczel, Yoshitami Ajiro, Jeremy P. Carlo, Tatsuo Goko, Daniel A. Goldfeld, Atsushi Kitada, Graeme M. Luke, Greg J. MacDougall, Igor G. Mihailescu, Jose A. Rodriguez, Peter L. Russo, Yoshihiro Tsujimoto, Christopher R. Wiebe, Travis J. Williams, Takafumi Yamamoto, Kazuyoshi Yoshimura, and Hiroshi Kageyama

Physical Review B **80** (2009) 174408/1−9.

Synthesis, Structural and Magnetic Properties of the Solid Solution $(CuCl_{1-x}Br_x)LaNb_2O_7$ ($0 < x < 1$)

Yoshihiro Tsujimoto, Atsushi Kitada, Hiroshi Kageyama, Masakazu Nishi, Yasuo Narumi, Koichi Kindo, Yoko Kiuchi, Yutaka Ueda, Yasutomo J. Uemura, Yoshitami Ajiro, and Kazuyoshi Yoshimura

Journal of the Physical Society of Japan **79** (2010) 014709/1−4.

Two-dimensional $S = 1$ Quantum Antiferromagnet $(NiCl)Sr_2Ta_3O_{10}$

Yoshihiro Tsujimoto, Atsushi Kitada, Yasutomo J. Uemura, Tatsuo Goko, Adam A. Aczel, Travis J. Williams, Graeme M. Luke, Yasuo Narumi, Koichi Kindo, Masakazu Nishi, Yoshitami Ajiro, Kazuyoshi Yoshimura, and Hiroshi Kageyama

Chemistry of Materials **22** (2010) 4625−4631.

First Single-Crystal Synthesis and Low Temperature Structural Determination of the Quasi-2D Quantum Spin Compound $(CuCl)LaNb_2O_7$

Olivier J. Hernandez, Cedric Tassel, Kunihiro Nakano, Werner Paulus, Cremens Ritter, Eric Collet, Atsushi Kitada, Kazuyoshi Yoshimura, and Hiroshi Kageyama

Dalton Transactions **40** (2011) 4605−4613.

Fe-Site Substitution Effect on the Structural and Magnetic Properties in $SrFeO_2$

Liis Seinberg, Takafumi Yamamoto, Cedric Tassel, Yoji Kobayashi, Naoaki Hayashi, Atsushi Kitada, Yuji Sumida, Takashi Watanabe, Masakazu Nishi, Kenji Ohoyama, Kazuyoshi Yoshimura, Mikio Takano, Werner Paulus, and Hiroshi Kageyama

Inorganic Chemistry **50** (2011) 3988−3995.

Two-Dimensional Frustrated Antiferromagnets (*M*Cl)$LaNb_2O_7$ (*M* = Mn, Co, Cr)

Atsushi Kitada, Yoshihiro Tsujimoto, Takeshi Yajima, Kazuyoshi Yoshimura, Yoshitami Ajiro, Yoji Kobayashi, and Hiroshi Kageyama

Journal of Physics: Conference Series **320** (2011) 012035/1−6.

ToF Inelastic Neutron Scattering Studies on Quantum Spin Systems (CuCl)LaB_2O_7 (*B* = Nb, Ta)

Seiko Ohira-Kawamura, Kenji Nakajima, Yasuhiro Inamura, Yoshihiro Tsujimoto, Atsushi Kitada, Fumitaka Takeiri, Hiroshi Kageyama, Yoshitami Ajiro, Masakazu Nishi, and Kazuhisa Kakurai

Journal of Physics: Conference Series **320** (2011) 012037/1−5.

Acknowledgment

The present thesis summarizes the author's studies performed at the Department of Energy and Hydrocarbon Chemistry, Graduate School of Engineering, Kyoto University.

First of all, the author wishes to express his greatest gratitude to Professor Hiroshi Kageyama for his invaluable advice and suggestion throughout the course of this work.

The author is also grateful to Professor Koichi Eguchi and Professor Takeshi Abe for their kind guidance and comments that helped me in completing this thesis.

The author is also grateful to Professor Zenji Hiroi, Professor Koichi Kindo, Professor Yutaka Ueda (Institute of Solid State Physics (ISSP, University of Tokyo), Professor Yasutomo J. Uemura (Columbia University), Professor Graeme M. Luke (McMaster University), Professor Takahito Terashima, Professor Kazuki Nakanishi, Professor Yoshitami Ajiro, and Professor Kazuyoshi Yoshimura (Kyoto University), for their kind guidance and comments that helped him in the completion of this thesis.

A special word of thanks is conveyed to Dr. Yoshihiro Tsujimoto (National Institute of Materials Science (NIMS)), Dr. Yoji Kobayashi, Dr. Shigeru Kasahara, Mr. George Hasegawa, Dr. Kazuyoshi Kanamori (Kyoto University), Dr. Yasuo Narumi (Institute of Metal Research(IMR), Tohoku University), Dr. Adam. A. Aczel (McMaster University), Dr. Masaki Ichihara, Dr. Yoko Kiuchi, and Dr. Masakazu Nishi (ISSP, University of Tokyo), for their valuable discussions and supports.

Sincere gratitude is also expressed to all the members of Professor Kageyama's Laboratory for their kind encouragement, support, and collaboration. A special debt of gratitude goes to the coauthors in the author's publications: Dr. Cedric Tassel, Mr.

Takashi Watanabe, Mr. Taro Kitano, Mr. Yoichi Baba, Mr. Yuji Sumida, Mr. K. Nakano, Ms. Liis Seinberg, Mr. Takafumi Yamamoto, Mr. Fumitaka Takeiri, and Dr. Takeshi Yajima.

The author would like to thank for the financial support from Japan Society of the Promotion of Science (JSPS) for Young Scientists.

Finally, the author would like to thank his family immensely, particularly, his parents Makoto and Hiroko Kitada, for their understanding, support, and encouragement.

Atsushi Kitada

2011